BROADBAND COHERENT LIGHT GENERATION IN RAMAN-ACTIVE CRYSTALS DRIVEN BY FEMTOSECOND LASER FIELDS

A Dissertation

by

MIAOCHAN ZHI

Submitted to the Office of Graduate Studies of
Texas A&M University
in partial fulfillment of the requirements for the degree of

DOCTOR OF PHILOSOPHY

December 2007

Major Subject: Physics

BROADBAND COHERENT LIGHT GENERATION IN RAMAN-ACTIVE CRYSTALS DRIVEN BY FEMTOSECOND LASER FIELDS

A Dissertation

by

MIAOCHAN ZHI

Submitted to the Office of Graduate Studies of
Texas A&M University
in partial fulfillment of the requirements for the degree of

DOCTOR OF PHILOSOPHY

Approved by:

Chair of Committee,	Alexei V. Sokolov
Committee Members,	Edward Fry
	George Kattawar
	Philip Hemmer
Head of Department,	Edward Fry

December 2007

Major Subject: Physics

ABSTRACT

Broadband Coherent Light Generation in Raman-active
Crystals Driven by Femtosecond Laser Fields. (December 2007)
Miaochan Zhi, B.E., Zhejiang University;
M.S., Zhejiang University
Chair of Advisory Committee: Dr. A. V. Sokolov

I studied a family of closely connected topics related to the production and application of ultrashort laser pulses. I achieved broadband cascade Raman generation in crystals, producing mutually coherent frequency sidebands which can possibly be used to synthesize optical pulses as short as a fraction of a femtosecond (fs). Unlike generation using gases, there is no need for a cumbersome vacuum system when working with room temperature crystals. Our method, therefore, shows promise for a compact system.

One problem for sideband generation in solids is phase matching, because the dispersion is significant. I solved this problem by using non-collinear geometry. I observed what to our knowledge is a record-large number of spectral sidebands generated in a popular Raman crystal $PbWO_4$ covering infrared, visible, and ultraviolet spectral regions, when I applied two 50 fs laser pulses tuned close to the Raman resonance. Similar generation in diamond was also observed, which shows that the method is universal. When a third probe pulse is applied, a very interesting 2-D color array is generated in both crystals.

As many as 40 anti-Stokes and 5 Stokes sidebands are generated when a pair of time-delayed linear chirped pulses are applied to the $PbWO_4$ crystal. This shows that pulses with picosecond duration, which is on the order of the coherence decay time, is more effective for sidebands generation than Fourier transform limited fs pulses.

I also studied the technique of fs coherent Raman anti-Stokes scattering (CARS) which is used as a tool for detecting dipicolinic acid, the marker molecule for bacterial spores. I observed that there is a maximum when the concentration dependence of the near-resonant CARS signal is measured. I presented a model to describe this behavior, and found an analytical solution that agrees with our experimental data.

Theoretically, I explored a possible application for single-cycle pulses: laser induced nuclear fusion. I performed both classical and quantum mechanical calculations for a system of two nuclei moving under a superintense ultrashort field. From our calculation I noted that the nuclear collisions occur on a sub-attosecond time scale, and are predicted to result in an emission of zeptosecond bursts of light.

In memory of my parents, Taizhang Zhi and Song'e Wei

ACKNOWLEDGMENTS

First I'd like to thank Dr. Sokolov for giving me the opportunity to carry out this research, which involves many exciting physics problems. His enthusiasm for research is inspiring and fosters an atmosphere of discovery. His wealth of knowledge is key in guiding my research.

I want to particularly thank Dr. Scully. Without his help, I would not have been admitted as a graduate student here. Later he gave me the opportunity of working on the fs-CARS project, which eventually lead to the bulk of the research for this dissertation. Dmitry Pestov, Robert K. Murawski, Xi Wang and Yuri Rostovtsev are a few of the people who have helped me tremendously during my research. The happy and exciting days of working with them will remain in my memory forever.

I am grateful to Dr. Hemmer for introducing me to the experimental optics basic skills. He showed me that some experiments can be done by simple, even used instruments. He broadened my research by kindly offering me free diamond samples. Dr. Fry and Dr. Kattawar, as busy as they are, guided me through the first difficult couple of years here. They talked to me using their valuable time.

I'd like to thank Elena Kuznetsova, Zoe Sariyanni, Changhui Li,Vladmir Sautekov, Pengwang Zhai, Petr Anisimov, Xudong Xu, Serguei Jerebtsov, Dr. Kolomenskii, Siu Ah Chin, Anatoly Svidzinsky, Ling Wang and many other fellow graduate students and friends who helped me during my research. I want to specially thank Tagarathi V. Nageswar Rao and Spiros Vellas at the TAMU supercomputing group for helping me parallelize the code.

I am very thankful for my husband Tom and my baby Tiya for giving me peace of mind while writing this dissertation. Lastly, I'd like to thank my family for their

love and support. My father was my first teacher and my mother taught me love. I thank my brothers and sisters for their guidance, support and sacrifices.

TABLE OF CONTENTS

CHAPTER Page

CHAPTER Page

LIST OF TABLES

LIST OF FIGURES

FIGURE Page

FIGURE Page

FIGURE Page

FIGURE Page

FIGURE Page

FIGURE Page

FIGURE Page

FIGURE Page

FIGURE Page

FIGURE Page

CHAPTER I

INTRODUCTION

The generation of ultrashort pulses is made possible by the technique of modelocking, which was first demonstrated in 1964 when nanosecond (ns) mode-locked pulses were produced [1]. First femtosecond (fs) laser pulses were generated using dye lasers in 1975 [2]. Later solid-state material was developed, which made the reliable and tunable pulsed laser available. The most attractive material is titanium-doped sapphire crystals (Ti:Sapphire, Al_2O_3:Ti^{3+}), which has extremely wide gain bandwidth (from 660 nm to 1180 nm) and makes the generation of 4 fs possible if this bandwidth is modelocked. With the important modelocking technique—"Kerr-lens modelocking" observed in 1991 [3], 6.5 fs pulses from a Ti:Sapphire laser were generated in 1997 [4]. This was by then the shortest pulse ever generated directly from a laser. Nowadays, commercial laser systems routinely produce sub-100 fs pulses and these pulses are finding applications in many fields. In 1999 Nobel Prize in Chemistry was awarded to Professor Ahmed H. Zewail "for showing that it is possible with rapid laser technique to see how atoms in a molecule move during a chemical reaction" using fs pulses.

Short pulse generation requires a wide phase-locked spectrum. Earlier the short pulses were obtained by expanding the spectrum of a mode locked laser by self phase modulation (SPM) in an optical fiber and then compensating for group velocity dispersion (GVD) by diffraction grating and prism pairs. Pulses as short as 4.4 fs have been generated [5]. For ultrafast measurements on the time scale of electronic motion, generation of subfemtosecond pulses is needed. Generation of subfemtosecond pulses with a spectrum centered around the visible region is even more desirable, due to the

---

This dissertation follows the style of Physical Review A.

fact that the pulse duration will be shorter than the optical period and will allow sub-cycle field shaping. As a result, a direct and precise control of electron trajectories in photoionization and high-order harmonic generation will become possible. But to break the few-fs barrier new approaches are needed.

In recent past, broadband collinear Raman generation in molecular gases has been used to produce mutually coherent equidistant frequency sidebands spanning several octaves of optical bandwidths [6]. It has been argued that these sidebands can be used to synthesize optical pulses as short as a fraction of a fs [7]. The Raman technique relied on adiabatic preparation of near-maximal molecular coherence by driving the molecular transition slightly off resonance so that a single molecular superposition state is excited. Molecular motion, in turn, modulates the driving laser frequencies and a very broad spectrum is generated, hence the term for this process "molecular modulation". By phase locking, a pulse train with a time interval of the inverse of the Raman shift frequency is generated. While at present isolated attosecond X-ray pulses are obtained by high harmonic generation (HHG) [8], the pulses are difficult to control because of intrinsic problems of x-ray optics. Besides, the conversion efficiency into these pulses is very low (typically 10^{-5}). On the other hand, the Raman technique shows promise for highly efficient production of such ultrashort pulses in the near-visible spectral region, where such pulses inevitably express single-cycle nature and may allow non-sinusoidal field synthesis [7].

In the Raman technique ns pulses are applied for preparing maximal coherence when gas is used as a Raman medium. When the pulse duration is shorter than the population relaxation time T_2 ($T_2 = \frac{1}{\pi c \Delta\nu_R}$, $\Delta\nu_R$ is the spontaneous Raman linewidth), the response of the medium is a highly transient process, i.e. the Raman polarization of the medium doesn't reach a steady state within the duration of the pump pulse. In this transient stimulating Raman scattering (SRS) regime, a large coherent a mole-

cular response is excited. It has been shown that the SRS gain increment explicitly depended on the integral cross section and was independent of the peak cross section of spontaneous Raman scattering as the ratio between the pumping pulse width (11 picosecond (ps)) and the time of optical dephasing of molecular vibrations changed from 0.42 to 9.3 in the spontaneous Raman scattering study of several oxide cyrstals [9]. The advantage of using a short pulse is that the number of the pulse in the train will be reduced compared with the ns Raman technique. But when a single fs pump is used, the strong self phase modulation (SPM) suppresses the Raman generation [10]. When a pulse duration is reduced to less than a single period of molecular vibration or rotation, an impulsive SRS regime is reached [11]. In this regime, an intense fs pulse with a duration shorter than the molecular vibrational period prepares the vibrationally excited state and a second, relatively weak, delayed pulse propagates in the excited medium in the linear regime and experiences scattering due to the modulation of its refractive index by molecular vibrations, which results in the generation of the Stokes and anti-Stokes sidebands [12]. This technique has the advantage of eliminating the parasitic nonlinear process since it is confined only within the pump pulse duration.

A closely related approach which is called four-wave Raman mixing (FWRM) for generating ultrashort pulses using two-color stimulated Raman effect is proposed in 1993 by Imasaka [13]. It is based on an experimental result his student has stumbled on. Shuichi Kawasaki was trying to develop a tunable source for thermal lens spectroscopy and he noticed bright, multicolored spots out of the Raman cell pressurized with hydrogen, which they called "Rainbow Star" [14]. The applied beam was supposed to be monochromatic but it actually had two color in it. To confirm the FWRM hypothesis, a nonlinear optical phenomenon in which three photons interact to produce a fourth photon, they used two-color laser beams with frequencies sepa-

rated by one of the rotational level splittings for hydrogen (590 cm^{-1}). Indeed, they observed the generation of more than 40 colors through the FWRM process, which provided a coherent beam consisting of equidistant frequencies covering more than thousandths cm^{-1} in frequency domain [15]. This FWRM process resulted in the generation of higher-order rotational sidebands at reduced pump intensity compared to the stimulated Raman scattering. The generation of the FWRM fields required phase matching and were coherently phased, and therefore had the potential to be used to generate sub-fs pulses [16].

Later ps pulses [17], ps and fs pump pulses [18], and a single fs pulse [10] were used to find the optimal experimental conditions for efficient generation of high-order rotational lines. Generally speaking, when the additional Stokes field is supplied rather than grown from quantum noise, advantages include: high-order anti-Stokes generation, higher conversion efficiency, and improved reproducibility of the pulses generated, as shown in earlier experiments with gas in ns regime [19]. Recently, efficient generation of high-order anti-Stokes Raman sidebands in a highly transient regime is also observed using a pair of 100-fs laser pulses tuned to Raman resonance with vibrational transitions in methane or hydrogen [20; 21]. They found that in this transient regime, the two-color set-up permits much higher conversion efficiency, broader generated bandwidth, and suppression of the competing SPM. The high conversion efficiency observed proves the preparation of substantial coherence in the system although the prepared coherence in the medium cannot be near maximal as in the case of the adiabatic Raman technique.

Almost all these works are carried out using a simple-molecule gas medium such as H_2, D_2, SF_6 or methane since the gas has negligible dispersion and long coherence lifetime. Molecular gas also has a few other advantages as a Raman medium. They are easily obtainable with a high degree of optical homogeneity and have high

frequency vibrational modes with small spectral broadening, which leads to large Raman frequency shifts and large Raman scattering cross sections. However, a Raman gas cell with long interaction length is needed due to the lower particle concentration [22].

How about solids Raman medium such as Raman crystal? As we know, the high density of solids results in the high Raman gain. The higher peak Raman cross sections in crystals result in lower SRS thresholds, higher Raman gain, and greater Raman conversion efficiency [22]. In addition, there is no need for cumbersome vacuum systems when working with room temperature crystals, and therefore a compact system can be designed.

The difficulty in using crystals is the phase matching between the sidebands because the dispersion in solids is significant. Sideband generation using strongly driven Raman coherence in solid hydrogen is reported but the generation process is very close to that of H_2 gas and solid hydrogen is a very exotic material [23]. Observation of generation with few sidebands (Stokes or Anti-Stokes) in other solid material is nothing new. About two decades ago, Dyson *et. al.* has observed one Stokes and 1 AS generated on quartz during an experiment designed for another purpose [24]. Later, there were numerous works of using Raman crystals for building Raman lasers which extended the spectral coverage of solid-state lasers by using SRS [25]. A detailed review of crystalline and fiber Raman lasers is given by Basiev [26]. The Raman spectroscopy of many crystals for SRS is therefore available because of this particular usage for building Raman lasers [27]. The Raman lasers are normally pumped by ns or ps pulses, which are comparable with the period of Raman-active vibration. In particular, potassium gadolinium tungstate ($KGd(WO_4)_2$; KGW) crystal, a very popular Raman crystal due to its high efficiency, has been studied with two-color fs pulses using collinear configuration [28]. Only 2 S were observed. Later impulsive

Raman scattering was observed in KGW using 70 fs pulses and 2 AS and 1 S were generated [29]. To our knowledge, no efficient generation using crystals had been reported before our experiment.

Therefore this research is directed toward the development of efficient broadband generation using Raman crystals. Since coherence lifetime in a solid is typically shorter than in a gas, the use of fs (or possibly ps) pulses is inevitable when working with room-temperature crystals. We choose $PbWO_4$ (lead tungstate), which exhibits good optical transparency, high damage threshold, and is non-hygroscopic. It is also a popular crystal used for building Raman lasers using ns or ps pulsed pumping [30]. Diamond is also used in our experiments since it has a narrow Raman line at relatively large Raman frequency—1332 cm^{-1} with linewidth of 3.3 cm^{-1}(T_2=3.2 ps) [31]. Moreover, diamond has the highest atom density of any material and it is transparent from far infrared to ultraviolet (above 230 nm) and has the widest electromagnetic bandpass of any material which is very attractive for broadband generation. We find that the main difference when working with crystal using two-color laser fields excitation is the necessity of using non-collinear geometry of the two applied fields so that the phase matching condition can be fulfilled. Phase matching plays a crucial role as we will show later. We have successfully generated as many as 40 colors when using two-color fs pulses and as many as 50 colors when three-color fs pulses are focused in the crystal. The effects of the polarization, the angle between the two pump beams, and the detuning between the two pump laser frequencies on the sidebands generation are studied as well.

During our work, we noticed that similar experiments were carried out with different crystals very recently. For example, high-order coherent anti-Stokes Raman scattering (CARS) has been observed in $YFeO_3$ and $KTaO_3$ crystals when two-color fs pulses were used [32; 33]. A multiple CARS generation in $KNbO_3$ [33] and in TiO_2

[34] have just been reported. We can see there is a growing interest in broadband generation using Raman-active crystals.

The major part of this dissertation, including chapter II to V, is on the subject of broadband sidebands generation in Raman crystals. In chapter II I give an introduction to the basic concepts which are needed for the description of our work, and a theoretical background for this Raman generation technique. In chapter III, I present our experimental results on broadband light generation in $PbWO_4$ using fs pulses. In chapter IV, broadband light generation in diamond is given. A. M. Zheltikov proposed the idea of using a sequence of short light pulses. When the time interval between the pulses in the train is equal to the period of Raman vibrations, the corresponding Raman-active mode is selectively excited [35]. This idea may be especially suitable for solids since the competing nonlinear processes such as SPM can be avoid using a pulse train while the coherence can still build up. We have extended this idea to the efficient generation in $PbWO_4$ using two time-delayed linearly chirped pulses. This experiment is discussed in chapter V.

Spontaneous, stimulated, and coherent Raman scattering provide the basis for Raman spectroscopy [36] which is a powerful tool widely used in chemistry, biology, and engineering [36; 37; 38]. In early research, ns CARS spectroscopy has been used for measuring the concentration of molecular species in combustion diagnostics [39]. In the time-resolved CARS technique [40], two pulses (pump and Stokes) are used to create coherence at one or more Raman transitions. Then a third time-delayed probe pulse is applied, which scatters from the coherence and generates the CARS and coherent Stokes Raman scattering (CSRS) signals. By delaying the third pulse, the strong instantaneous nonresonant background from FWM can be eliminated, which renders femtosecond CARS superior to nanosecond CARS for the determination of spectroscopic constants, especially under extreme conditions such as those in com-

bustion cells or flames [41]. Recently time-resolved femtosecond CARS spectroscopy has been applied for measuring the gas-phase temperatures and concentrations [42].

Dipicolinic acid (DPA) is a marker molecule for bacterial spores [43] and the ability to detect trace amounts is of paramount importance. We work with DPA in a H_2O/NaOH solution (NaDPA). Optical coherence of NaDPA has a relaxation time of the order of 30 fs, and vibrational coherence in liquids has picoseconds time scale. Femtosecond pulses therefore are essential for the study of a complex organic molecule such as NaDPA. In chapter VI, we study concentration dependence of fs CARS in the presence of strong absorption using a NaDPA solution. We also study the CSRS in the crystalline DPA.

A variety of nonlinear processes becomes accessible thanks to the large intensities of fs pulses. In chapter VII, I present a theoretical study of laser-controlled nuclear fusion using superintense ultrashort (a few cycle) pulses. This dissertation is summarized in chapter VIII.

CHAPTER II

BASIC CONCEPTS AND THEORY

In this chapter, I give some basic concepts for ultrashort pulses: the linear and nonlinear pulse propagation of a short pulse in a dispersive medium and the resultant nonlinear effects such as self phase modulation and self focusing, which are encountered frequently in our experiment using fs pulses. An introduction to the Raman scattering, which is crucial to this work, is given here. The terms including four wave mixing, coherent anti-Stokes Raman scattering, coherent Stokes Raman scattering, and four wave Raman mixing, which are often used in the related references and this work, are given here too. After that I briefly mention an ultrafast pulse measurement technique—self diffraction frequency-resolved optical gating, which is used in our experiment to characterize the chirp of a pulse.

In the theory part I give a derivation for the Hamiltonian of the molecular system including the interaction with the laser field. In order to show how the propagation of the two fields leads to the sidebands generation, we perform an approximate theoretical calculation using the crystal $PbWO_4$ as an example.

A. Basic concepts

1. Linear pulse propagation in a dispersive medium

When a pulse propagates in a dispersive medium, the pulse gets broadened because frequency components within the pulse travel with different phase velocity $V_\phi = \frac{c}{n(\lambda)}$, where c is the speed of light and $n(\lambda)$ is the refractive index at this wavelength. This leads to a chirped pulse, where the instantaneous frequency varies over the temporal pulse. A pulse is called linearly chirped when the phase has a quadratic variation, i.e.

the frequency varies linearly with time delay. The frequency of a positively chirped pulse increases as a function of time delay, while the frequency of a negatively chirped pulse decreases vs. time. The pulse length increases due to the chirp and consequently the peak intensity of the pulse decreases. We can use it to our advantage as will be shown in chapter V. Here I give a derivation of a pulse output width from a dispersive medium as a function of the input pulse length and the group delay dispersion.

a. Pulse broadening

The electric field of a gaussian pulse with width (FWHM) τ_{in}, amplitude E_0, and center frequency ω_0 can be written as:

$$E_{in}(t) = E_0 \exp(-2\ln 2 \frac{t^2}{\tau_{in}^2} - i\omega_0 t). \tag{2.1}$$

The fourier transform of the electric field is:

$$E_{in}(w) = \frac{1}{\sqrt{2\pi}} \int_{-\infty}^{\infty} E_{in}(t) \exp(i\omega t) dt = \alpha \exp[-\frac{\tau_{in}^2 (\omega - \omega_0)^2}{8\ln 2}]. \tag{2.2}$$

Here $\alpha = \frac{E_0 \tau_{in}}{2\sqrt{\ln 2}}$ is a constant. The electric field of the output pulse is [44]:

$$\begin{aligned} E_{out}(w) &= E_{in}(w) \exp\{-i[\phi + (\omega - \omega_0)\phi' + \frac{\phi''}{2}(\omega - \omega_0)^2]\} \\ &= \alpha \exp(-i\phi) \exp(-i(\omega - \omega_0)\phi') \exp[-(\frac{\tau_{in}^2}{8\ln 2} + \frac{i\phi''}{2}(\omega - \omega_0)^2]. \end{aligned} \tag{2.3}$$

Here ϕ' is the group delay and ϕ'' is the group delay dispersion (GDD). The high-order terms such as third-order dispersion (TOD) are neglected. Let $\omega' = \omega = \omega_0$

and $\Gamma = -(\frac{\tau_{in}^2}{8\ln 2} + \frac{i\phi''}{2})$, then

$$\begin{aligned} E_{out}(t) &= \int_{-\infty}^{\infty} E_{out}(\omega)\exp(-i\omega t)d\omega \\ &= \alpha\sqrt{\frac{\pi}{\Gamma}}\exp[-i(\phi-\omega_0 t)]\exp[-\frac{(\phi'-t)^2}{4\Gamma}] \\ &= \alpha^{'}\exp\left[-i(\phi-\omega_0 t) - \frac{(\phi'-t)^2}{\frac{\tau_{in}^2}{2\ln 2} + 2i\phi''}\right]. \end{aligned} \tag{2.4}$$

Let's redefine $\Gamma = (\frac{\tau_{in}^2}{2\ln 2} + 2i\phi'')^{-1}$, then the output field has the form of

$$\begin{aligned} E_{out}(t) &= E_0\exp[i(\omega_0 t-\phi) - \Gamma(t-\phi')^2] \\ &= E_0 e^{i(\omega_0 t-\phi)} e^{\left[\frac{2i\phi''}{\frac{\tau_{in}^4}{4(\ln 2)^2+4\phi''^2}}(t-\phi')^2\right]} e^{\left\{-\left[\frac{\frac{\tau_{in}^2}{2\ln 2}}{\frac{\tau_{in}^4}{4(\ln 2)^2+4\phi''^2}}(t-\phi')^2\right]\right\}}. \end{aligned} \tag{2.5}$$

We finally get the expression for the output pulse width versus the input pulse width as:

$$\frac{\tau_{out}}{\tau_{in}} = \sqrt{1 + \frac{\phi''^2}{\tau_{in}^4} * 16(\ln 2)^2} \tag{2.6}$$

The phase change for a pulse through a dispersive medium l is $\phi = kz = \frac{2\pi}{\lambda}(ln) = \frac{\omega}{c}ln$. Here n is function of frequency and wavevector k=$2\pi/\lambda$. We can write

$$\phi(\omega) = \frac{\omega ln(w)}{c}. \tag{2.7}$$

The GDD ϕ'' as a function of λ and $\frac{d^2n}{d\lambda^2}$ can be calculated as follows.

$$\phi'' = \frac{d^2\phi}{d\omega^2} = \frac{l}{c}(\omega\frac{d^2n}{d\omega^2} + 2\frac{dn}{d\omega}). \tag{2.8}$$

Since

$$\frac{dn}{d\omega} = \frac{dn}{d\lambda}\frac{d\lambda}{d\omega} = -\frac{\lambda^2}{2\pi c}\frac{dn}{d\lambda}; \tag{2.9}$$

and

$$\frac{d^2n}{d\omega^2} = \frac{d}{d\lambda}(\frac{dn}{d\omega})\frac{d\lambda}{d\omega} = \frac{\lambda^4}{4\pi^2c^2}\frac{d^2n}{d\lambda^2} + \frac{\lambda^3}{2\pi^2c^2}\frac{dn}{d\lambda}. \tag{2.10}$$

Therefore we have

$$\phi'' = \frac{d^2\phi}{d\omega^2} = \frac{\lambda^3 l}{2\pi c^2}\frac{d^2 n}{d\lambda^2}. \tag{2.11}$$

Please note that the GDD always refers to some optical element (e.g. the GDD of a 1-mm thick silica plate is 35 fs^2 at 800 nm) or to some given length of a medium (e.g. an optical fiber). If one specifies the GDD per unit length (in units of s^2/m), this is the group velocity dispersion (GVD) [45].

b. Effective interaction length

Due to dispersion of the material, different waves propagate at different group velocities. For femtosecond pulses, the interacting pulses may get separated after propagating some distance in the medium, which means that there is a reduced effective interaction length L_{eff}. Thus L_{eff} is an important parameter for choosing the thickness of the crystal. Next I show how to calculate L_{eff}.

Group velocity V_G is defined as:

$$V_G = (\frac{dk}{d\omega})^{-1} = \frac{c}{n - \lambda\frac{dn}{d\lambda}}. \tag{2.12}$$

The group velocity mismatch (GVM) is defined as:

$$\triangle V_G = \left(\frac{1}{V_{G,i}} - \frac{1}{V_{G,j}}\right)^{-1}. \tag{2.13}$$

where $V_{G,i}$ and $V_{G,j}$ are the group velocities of the two interacting waves i and j. The interaction length L_{eff} can be calculated by:

$$L_{eff} = 2\tau_p|\triangle V_G| = 2\tau_p\left|\left(\frac{1}{V_{G,i}} - \frac{1}{V_{G,j}}\right)^{-1}\right|. \tag{2.14}$$

where τ_p is the input pulse duration at FWHM. For the crystal we use, the interaction length of $PbWO_4$ and diamond is about 0.5 mm and 1.2 mm respectively when pulses

with wavelength 580 and 640 nm are used. The interaction length is longer when a pair of IR pulses are used due to the relatively smaller dispersion over this region.

2. Nonlinear pulse propagation

a. Self focusing and white light generation

Nonlinear optical phenomena arise when an intense short pulse interacts with a nonlinear medium. In nonlinear optics, the optical response can be described by expressing the polarization $\tilde{P}(t)$ as a power series in the field strength $\tilde{E}(t)$ as in [46]:

$$\begin{aligned} \tilde{P}(t) &= \chi^{(1)}\tilde{E}(t) + \chi^{(2)}\tilde{E}^2(t) + \chi^{(3)}\tilde{E}^3(t) + \cdots \\ &= \tilde{P}^{(1)}(t) + \tilde{P}^{(2)}(t) + \tilde{P}^{(3)}(t) + \cdots \end{aligned} \tag{2.15}$$

The constant of proportionality $\chi^{(1)}$ is the linear susceptibility. The linear polarization of the material $\tilde{P}^{(1)}(t)$ gives rise to the linear optical effects such as refractive index, dispersion and birefringence. The quantities $\chi^{(2)}$ and $\chi^{(3)}$ are the second- and third-order nonlinear optical susceptibilities, respectively. The second order nonlinear polarization $\tilde{P}^{(2)}(t)$ is responsible for second harmonic generation, sum- and difference-frequency mixing, and parametric generation.

The third order nonlinear polarization $\tilde{P}^{(3)}(t)$ is essential to this work and will be described in detail here. First it is responsible for optical Kerr effect. A sufficiently high laser field can induce a nonlinear refractive index response in the materials such that the index n becomes intensity dependent as:

$$n = n_0 + n_2 I \tag{2.16}$$

where n_0 is the usual linear or low intensity refractive index, $n_2 = \frac{12\pi^2}{n_0^2 c}\chi^{(3)}$ is an optical constant that characterizes the strength of the optical nonlinearity, and I

is the intensity of the incident laser field. When a beam of light having a uniform transverse intensity distribution propagates through a material in which n_2 is positive, the material acts as a positive lens, which causes the rays to curve toward each other. The intensity at the focal spot of the self-focused beam is usually sufficiently large to lead to optical damage of the material. We have observed this in the crystal sample we use. The beam profile is drastically changed as shown in Fig. 1 (b).

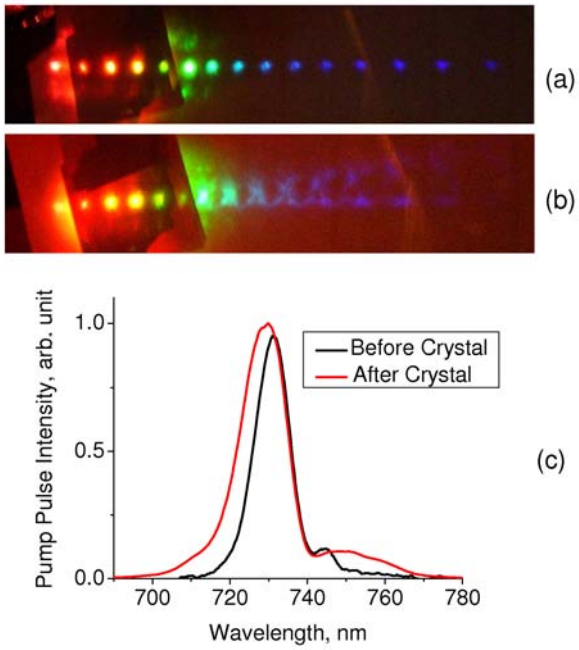

Fig. 1. Nonlinear effects in crystal. (a) The intensity of the pump beams used are below the threshold of self focusing. The sidebands generated are nice, round spots. (b) The intensity of the pump beams used are above the threshold of self focusing, which results in the deterioration of the generated beams. (c) SPM causes pulse broadening as the pulse propagates through the crystal.

b. Self phase modulation and cross phase modulation

The intensity of an ultrashort pulse changes with time, hence different parts of the pulse experience different magnitudes of refractive index. The time varying refractive index produces a time-dependent phase modulation of the pulse and therefore contributes to spectral broadening of the pulse, which is called **self phase modulation** (SPM). Considering a pulse with center frequency ω_0 propagating in a medium of length L, the phase

$$\phi(t) = \omega_0 t - kz = \omega_0 t - \frac{2\pi n}{\lambda} L. \tag{2.17}$$

The instantaneous frequency is the derivative of the phase with respect to time as given by:

$$\frac{d\phi(t)}{dt} = \omega_0 - \frac{2\pi L}{\lambda}\frac{dn}{dt} = \omega_0 - \frac{2\pi n_2 L}{\lambda}\frac{dI(t)}{dt}. \tag{2.18}$$

We see that the nonlinear refractive index induces an approximately linear chirp on the pulse. If one pulse modifies the effective refractive index causing a second pulse to change its characteristics, this is referred to as **cross-phase modulation** (CPM). In our experiment, SPM causes the spectral broadening after the crystal as shown in Fig. 1 (c) and CPM makes two pulses affect each other slightly. CPM provides a very convenient way to find the zero delay of two interacting pulses. When the intensity of a pulse is high enough, the pulse after a nonlinear medium is drastically broadened in spectrum. The spectrally broadened pulse is referred to as a **white-light continuum** pulse. White light generation is a very complicated process. Beside SPM, and self-focusing, there are other nonlinear processes contributing to the white light generation [47]. White light generation in glass can be used to find the focus of the pulses as well as the time overlap between pulses since one can use a high intensity beam without the concern of burning the glass.

3. Raman scattering

a. Linear Raman scattering

I'd like to pay some tribute to the great scientist Raman here. It is in March 1928 that professor Raman announced his discovery of Raman scattering, which he called a new secondary radiation. "*The apparatus used by Raman for the discovery consisted of a mirror for deflecting sunlight, a condensing lens, a pair of complementary glass filters, a flask containing benzene and a pocket spectroscope. the total cost not exceeding $25*", as described by R. S. Krishnan [48]. Raman observed not only the Stokes radiation, which has the lower photon energy than the incident photon, but the extremely weak anti-Stokes radiation.

Raman scattering is an inelastic collision of an incident photon with a molecule. Following the collision, a photon with either frequency $\omega_S = \omega_l - \omega_R$ or $\omega_{AS} = \omega_l - \omega_R$ is scattered. Here ω_R is the vibrational frequency of the molecule. The former one is called **Stokes** radiation. In the latter case, the photo $\hbar\omega_l$ is scattered by an excited molecule and is called **anti-Stokes** radiation. This process is illustrated in Fig. 2. The intermediate state of the system during the scattering process is often called "virtual state" (dotted line in Fig. 2 (a) and (b)). Since in thermal equilibrium the population of level n is smaller than the population in ground state g by the Boltzmann factor $\exp(-\hbar\omega_{ng}/kT)$, most molecules will initially be in the ground state. Consequently, the anti-Stokes radiation is much weaker than the Stokes radiation. If the virtual level coincides with one of the molecular eigenstates, one speaks of the **resonance Raman effect**. As a result of the resonance, the Stokes or anti-Stokes radiation can be dramatically enhanced. Both Boyd [46] and Demtröder [49] give an excellent description of the Raman scattering. Here I just briefly write some of the formulas which are important for understanding the work presented in this

dissertation.

The dipole moment of a molecule under an electric field $E = E_0 \cos(\omega t)$ can be written as:

$$p = \mu_0 + \tilde{\alpha} E. \tag{2.19}$$

The first term μ_0 represents a possible permanent dipole moment while $\tilde{\alpha} E$ is the induced dipole moment. $\tilde{\alpha}$ is called the polarizability. The dipole moment and polarizability can be expanded into Taylor series in the normal coordinates q_n of the nuclear displacements as:

$$\mu = \mu_0 + \sum_{n=1}^{Q} \left(\frac{\partial \mu}{\partial q_n} \right)_0 q_n + \ldots, \tag{2.20}$$

$$\alpha_{ij}(q) = \alpha_{ij}(0) + \sum_{n=1}^{Q} \left(\frac{\partial \alpha_{ij}}{\partial q_n} \right)_0 q_n + \ldots. \tag{2.21}$$

For small vibrational amplitudes the normal coordinates $q_n(t)$ of the vibrating molecule can be approximated by

$$q_n(t) = q_{n0} \cos(\omega_R t), \tag{2.22}$$

ω_R is the vibrational frequency. Inserting Eq. 2.20 and Eq. 2.21 to into Eq. 2.22 yields the total dipole moment [49]

$$\begin{aligned} p = \mu_0 \quad &+ \quad \sum_{n=1}^{Q} \left(\frac{\partial \mu}{\partial q_n} \right)_0 q_{n0} \cos(\omega_n t) + \alpha_{ij}(0) E_0 \cos(\omega t) \\ &+ \quad \frac{1}{2} E_0 \sum_{n=1}^{Q} \left(\frac{\partial \alpha_{ij}}{\partial q_n} \right)_0 q_{n0} [\cos(\omega + \omega_R) t + \cos(\omega - \omega_R) t]. \end{aligned} \tag{2.23}$$

The last term describes the Raman scattering. We can see that two inelastically scattered components with the frequencies $\omega - \omega_R$ (Stokes waves) and $\omega + \omega_R$ (anti-Stokes waves) are produced. The mode with polarizability change $\frac{\partial \alpha}{\partial q} \neq 0$ is called a

Raman-active mode.

b. Stimulated Raman scattering

This spontaneous Raman scattering process has very low efficiency. Typically only approximately 1 part in 10^6 of the incident radiation will be scattered into the Stokes frequency. When the laser beam intensity becomes sufficiently large, highly efficient scattering can occur as a result of the process called **stimulated Raman scattering** (SRS). It is described in detail in Boyd's book [46]. Here I just give some of the relevant equations.

The expression for the Stokes polarization is:

$$\tilde{P}_S^{NL}(z,t) = P(\omega_S)\exp(-i\omega_S t) + c.c. \tag{2.24}$$

The complex amplitude $P(\omega_S)$ is given by:

$$P(\omega_s) = 6\chi_R(\omega_S)|A_L|^2 A_S \exp(ik_S z). \tag{2.25}$$

Assume the total optical field can be represented as:

$$\tilde{E}(z,t) = A_L \exp[i(k_L z - \omega_L t)] + A_S \exp[i(k_S z - \omega_S t)] + \text{c.c.}. \tag{2.26}$$

Here $\chi_R(\omega_S)$ is a shortened form of $\chi^3(\omega_S = \omega_S + \omega_L - \omega_L)$ and is given by:

$$\chi_R(\omega_S) = \frac{(N/6m)\left(\frac{\partial\alpha}{\partial q}\right)_0^2}{\omega_R^2 - (\omega_L - \omega_S)^2 + 2i(\omega_L - \omega_S)\gamma}. \tag{2.27}$$

Here γ is the damping constant, N is the density of the molecules and m is the reduced nuclear mass.

The evolution of the Stokes field A_S is given in the slowly-varying amplitude

approximation by

$$\frac{dA_S}{dz} = -\alpha_S A_S \tag{2.28}$$

where

$$\alpha_S = -12\pi i \frac{\omega s}{n_s c} \chi_R(\omega_S) |A_L|^2 \tag{2.29}$$

is the Stokes wave "absorption" coefficient which has a negative real part, implying that the Stokes wave has exponential growth. Raman Stokes amplification is a process for which the phase-matching condition is automatically satisfied. For anti-Stokes waves, there is a similar expression as Stokes waves. And there is another contribution that depends on the Stokes amplitude. The total polarization at the AS frequency is given by:

$$P(\omega_a) = 6\chi_R(\omega_a)|A_L|^2 A_a \exp(ik_a z) + 3\chi_F(\omega_a) A_L^2 A_S^\star \exp[i(2k_L - k_S)z] \tag{2.30}$$

Here $\chi_F(\omega_a) = \chi^3(\omega_a = 2\omega_L - \omega_S)$ is a FWM susceptibility. Similarly there is a FWM contribution to the Stokes polarization. Assuming optically isotropic medium, slowly varying amplitude and constant pump approximations, the field amplitude of AS and S field obey the coupled equations:

$$\frac{dA_S}{dz} = -\alpha_S A_S + \kappa_S A_a^* e^{i\triangle kz}, \tag{2.31}$$

$$\frac{dA_a}{dz} = -\alpha_a A_a + \kappa_a A_S^* e^{i\triangle kz}. \tag{2.32}$$

When the wavevector mismatch $\triangle k = (2\mathbf{k}_L - \mathbf{k}_S - \mathbf{k}_a)$ is small, the FWM term is an effective driving term. Perfect phase matching can always be achieved if the Stokes wave propagates at some nonzero angle with respect to the laser wave.

For SRS, the Stokes field and anti-Stokes field generated can have higher efficiency, specially when an external cavity is used. Many Raman lasers, based on the SRS process, have been built using nonlinear crystals [25]. The phenomenon

of high-order stimulated Raman lines simultaneously generated over a wide spectral region is called **four-wave Raman mixing** (FWRM) [10]. For example, FWRM in crystal $PbWO_4$ has been observed up to 9th order [30]. We have mentioned four

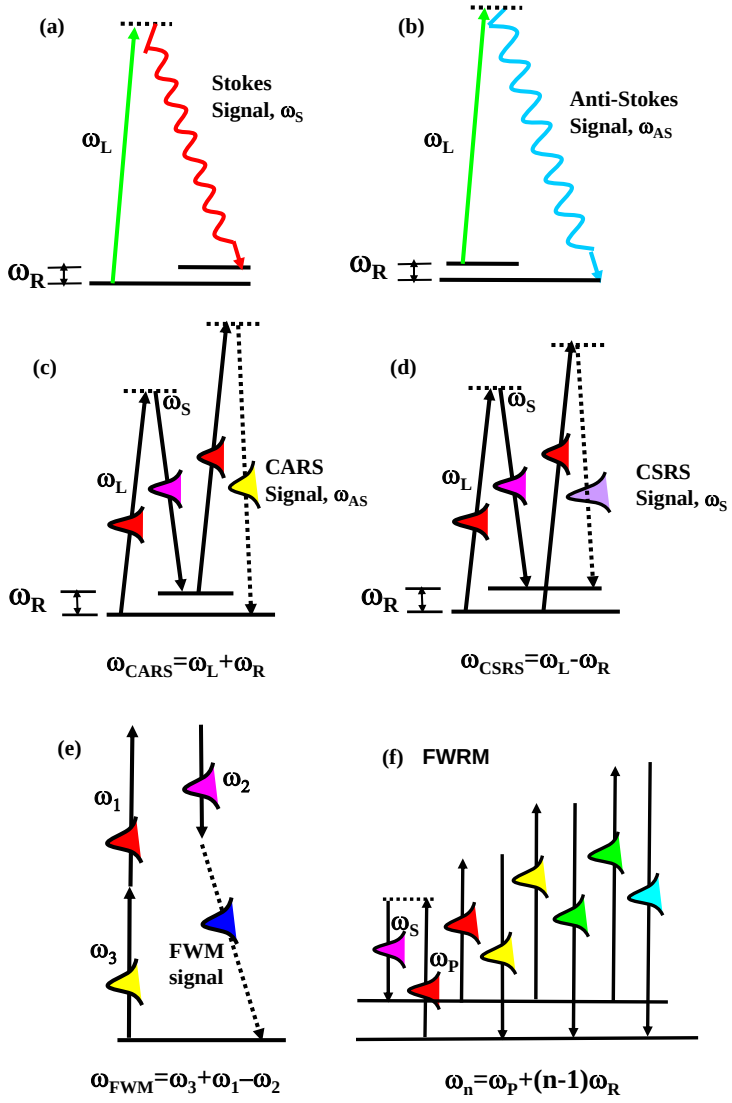

Fig. 2. Schematic level diagrams for different processes. (a) anti-Stokes Raman scattering; (b) Stokes Raman scattering; (c) CARS (d) CSRS; (e) FWM; (f) FWRM.

wave mixing susceptibility in the above description. **Four wave mixing** (FWM) is a general term for a process in which a frequency is created from the three other

frequencies $\omega_4 = (\pm\omega_1) + (\pm\omega_2) + (\pm\omega_3)$. Third harmonic generation is a special case of FWM in which $\omega_1 = \omega_2 = \omega_3$, and $\omega_4 = 3\omega_1$. In **coherent anti-Stokes Raman scattering (CARS)**, a special case of FWM, the two laser field are chosen such that $\omega_1 - \omega_2 = \omega_R$. These two waves generate a large population density of vibrationally excited molecules. These excited molecules act as a nonlinear medium for the generation of AS radiation at $\omega_{CARS} = 2\omega_2 - \omega_1$. CARS is also called a four-wave parametric mixing process. The intensity I of the CARS signal is [49]

$$I \propto |\chi^{(3)}|^2 N^2 I_1(\omega_1)^2 I_2(\omega_2) \tag{2.33}$$

Here N is the molecular density and $I_1(\omega_1)$ and $I_2(\omega_2)$ are the pump laser intensities. Another similar process is **coherent Stokes Raman scattering (CSRS)** in which a frequency $\omega_{CSRS} = 2\omega_1 - \omega_2$ is generated. The different processes are shown schematically in Fig. 2.

4. Ultrashort pulse measurement method—SD FROG

To measure an event in time, you must use a shorter one. How to measure a shortest pulse ever created is a difficult problem which is addressed by a book "Frequency-Resolved Optical Gating: The Measurement of Ultrashort Laser Pulses" [50]. Here I will just briefly mention one method which is easy to set up and is used in our experiment—SD Frequency-Resolved Optical Gating (FROG).

Self diffraction (SD) is also a $\chi^{(3)}$ nonlinear process in which the three interactive pulses are replica of each other. It is also called forward four-wave mixing. Here I give a brief description of this powerful pulse measuring method. The schematics of the SD FROG is shown in Fig. 3 [51]. The signal pulse field has the form of:

$$E_{sig}(t,\tau) = E(t)^2 E^*(t-\tau) \tag{2.34}$$

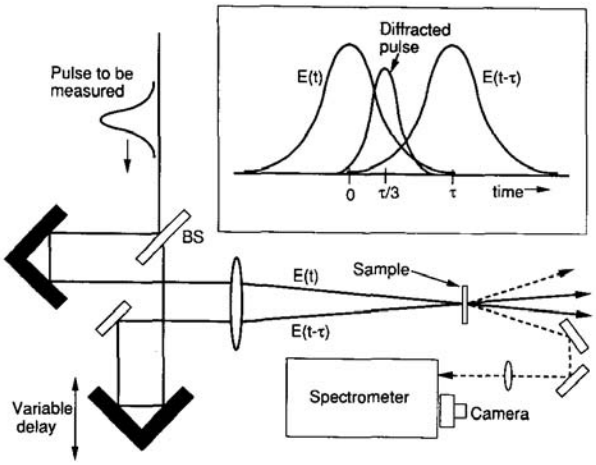

Fig. 3. Schematics of the SD FROG. The signal pulse is centered at approximately the time $\tau/3$ of one input pulse (From D. J. Kane and R. Trebino, IEEE Journal of Quantum Electronics, Vol. 29, 571 (1993)).

and the measured signal intensity is

$$I_{FROG}(\omega,\tau) = |\int_{-\infty}^{\infty} E(t)^2 E^*(t-\tau)\exp(-i\omega t)dt|^2. \tag{2.35}$$

Assuming it is a gaussian pulse $E(t) = \exp(-\frac{t^2}{\tau^2})$, then

$$\begin{aligned} E_{sig}(t,t_0) &= \exp(-\frac{t^2}{t_0^2})\exp[-\frac{(t-\tau)^2}{t_0^2}]\exp[-\frac{(t-\tau)^2}{t_0^2}] \\ &= \exp[-\frac{t^2}{t_0^2} - 2\frac{(t-\tau)^2}{t_0^2}] \end{aligned} \tag{2.36}$$

From $\frac{d}{dt}(E_{sig}(t,t_0)) = 0$, one can find that the signal pulse has a maximum at approximately the time $\tau/3$ of one input pulse as shown in Fig. 3 inset. The instantaneous frequency of the signal pulse is

$$\Omega_{sig}(\tau) = 2\omega(\tau/3) - \omega(-2\tau/3). \tag{2.37}$$

As a result, for the case of linear chirp, if the FROG signal frequency is $\Omega_{sig}(\tau) = \beta\tau$, then $\omega(\tau) = 3/4\beta\tau$. This formula will be used in chapter VIII when the subject of

chirped pulse excitation is discussed.

B. Hamiltonian derivation and sidebands generation

As described in the introduction, our method of generating broadband sidebands in crystals uses two pump fields, which are tuned close to the Raman frequency. These two fields prepare the molecular coherence. The coherent molecular motion modulates light and produces the sidebands. In this section I derive the Hamiltonian using an approach following Hickman's description [52] which arrives at the same formulas as shown in [53]. All the equations are in terms of z and the retarded time $t = t_{lab} - z/c$. The field propagation which produces the sidebands is shown in [53].

First we write the time-dependent wave function in terms of an expansion of zero field eigenfunctions:

$$H_0|n>=\hbar W_n|n> \tag{2.38}$$

$$\psi = \sum_n C_n e^{-iW_n t}|n> \tag{2.39}$$

The time dependent Schrödinger equation has the form of:

$$(H_0 + V)|n>=i\hbar\frac{\partial\psi}{\partial t} \tag{2.40}$$

Using Eq. 2.38 and Eq. 2.39 we have:

$$\sum_n C_n e^{-iW_n t}(H_0 + V)|n>=i\hbar\sum_n(\frac{\partial C_n}{\partial t} - iW_n C_n)e^{-iW_n t}|n> \tag{2.41}$$

Rearranging the terms we get:

$$\sum_n i\hbar(\frac{dC_n}{dt} - C_n V)e^{-iW_n t}|n>=0 \tag{2.42}$$

Applying $< j|$ to the above equation, we have:

$$\sum_n < j|i\hbar(\frac{dC_n}{dt} - C_n V)e^{-iW_n t}|n >= 0; \tag{2.43}$$

$$i\hbar\frac{dC_n}{dt}e^{-iW_j t} = \sum_n < j|C_n V|n > e^{-iW_n t}. \tag{2.44}$$

Exchanging index j with n and letting $W_{jn} = W_j - W_n$, we obtain:

$$i\hbar\frac{dC_n}{dt} = \sum_j < n|V(t)|j > C_j e^{-iW_{jn}t}. \tag{2.45}$$

The interaction potential can be written as:

$$V = -P\varepsilon = -\frac{1}{2}P\sum_j V_j e^{-i\omega_j t} + c.c., \tag{2.46}$$

with $V_j = E_j e^{i\varphi_j}$. Therefore, from Eq. 2.45, we have

$$\begin{aligned} i\hbar\frac{\partial C_n}{\partial t} &= \sum_{n'} < n|V(t)|n' > C'_n e^{-iW_{n'n}t} \\ &= \sum_{n'} < n| - \frac{1}{2}P\sum_j V_j e^{-i\omega_j t} + c.c.|n' > C'_n e^{-iW_{n'n}t} \\ &= -\frac{1}{2}\sum_{n'=1}^{\infty} P_{nn'}C_{n'}\sum_j [V_j e^{i(\omega_j - W_{n'n})t} + V_j^* e^{-i(\omega_j + W_{n'n})t}] \end{aligned} \tag{2.47}$$

Here we deal with the situation where $P_{12} = 0$ and we can neglect all the terms except $P_{1n'}$ and $P_{2n'}$. Next we use adiabatic approximation to solve for C_n (n=3,4...) in

terms of C_1, C_2 as:

$$\begin{aligned} C_n &= \frac{i}{2\hbar}\sum_{n'=1}^{2} C_{n'}P_{nn'}\sum_j[\frac{V_j e^{i(\omega_j - W_{n'n})t}}{i(\omega_j - W_{n'n})} + \frac{V_j^* e^{-i(\omega_j + W_{n'n})t}}{-i(\omega_j + W_{n'n})}] \\ &= -\frac{1}{2\hbar}\sum_{n'=1}^{2} C_{n'}P_{nn'}\sum_j[\frac{V_j^* e^{-i(\omega_j - W_{nn'})t}}{\omega_j - W_{nn'}} - \frac{V_j e^{i(\omega_j + W_{nn'})t}}{\omega_j + W_{nn'}}] \\ &= -\frac{1}{2\hbar}\{C_1 P_{n1}\sum_j[\frac{V_j^* e^{-i(\omega_j - W_{n1})t}}{\omega_j - W_{n1}} - \frac{V_j e^{i(\omega_j + W_{n1})t}}{\omega_j + W_{n1}}] \\ &+ C_2 P_{n2}\sum_j[\frac{V_j^* e^{-i(\omega_j - W_{n2})t}}{\omega_j - W_{n2}} - \frac{V_j e^{i(\omega_j + W_{n2})t}}{\omega_j + W_{n2}}]\}. \end{aligned} \tag{2.48}$$

Plugging in the equation of C_n to Eq. 2.47, we get:

$$\begin{aligned} i\hbar\frac{\partial C_1}{\partial t} &= -\frac{1}{2}\sum_{n=3}^{\infty}\sum_j[V_j e^{i(\omega_j - W_{n1})t} + V_j^* e^{-i(\omega_j + W_{n1})t}] \\ &= -\frac{1}{2}\sum_{n=3}^{\infty}\sum_{j'}[V_{j'} e^{i(\omega_{j'} - W_{n1})t} + V_{j'}^* e^{-i(\omega_{j'} + W_{n1})t}] \\ &\times (-\frac{1}{2\hbar})\{C_1 P_{n1}\sum_j[\frac{V_j^* e^{-i(\omega_j - W_{n1})t}}{\omega_j - W_{n1}} - \frac{V_j e^{i(\omega_j + W_{n1})t}}{\omega_j + W_{n1}}] \\ &+ C_2 P_{n2}\sum_j[\frac{V_j^* e^{-i(\omega_j - W_{n2})t}}{\omega_j - W_{n2}} - \frac{V_j e^{i(\omega_j + W_{n2})t}}{\omega_j + W_{n2}}]\} \end{aligned} \tag{2.49}$$

we keep only the stationary terms, i.e. eliminating the terms with $e^{i(\omega_j \omega_{j'})t}$, it is now:

$$\begin{aligned} i\hbar\frac{\partial C_1}{\partial t} &= \frac{1}{4\hbar}\sum_{n=3}^{\infty}\{C_1 P_{1n}P_{n1}\sum_j\sum_{j'}[\frac{V_{j'}V_j^* e^{-i(\omega_j - \omega_{j'})t}}{\omega_j - W_{n1}} - \frac{V_j V_{j'}^* e^{i(\omega_j - \omega_{j'})t}}{\omega_j + W_{n1}}] \\ &+ C_2 P_{1n}P_{n2}\sum_j[\frac{V_{j'}V_j^* e^{-i(\omega_j - \omega_{j'})t}}{\omega_j - W_{n2}} - \frac{V_j V_{j'}^* e^{i(\omega_j - \omega_{j'})t}}{\omega_j + W_{n2}}]e^{-i(W_{n1} - W_{n2})t}\} \\ &= \frac{1}{4\hbar}\sum_{n=3}^{\infty}\{C_1 P_{1n}P_{n1}\sum_j\sum_{j'}[\frac{V_{j'}V_j^* e^{-i(\omega_j - \omega_{j'})t}}{\omega_j - W_{n1}} - \frac{V_j V_{j'}^* e^{i(\omega_j - \omega_{j'})t}}{\omega_j + W_{n1}}] \\ &+ C_2 P_{1n}P_{n2}\sum_j[\frac{V_{j'}V_j^* e^{-i(\omega_j - \omega_{j'} + \omega_R)t}}{\omega_j - W_{n2}} - \frac{V_j V_{j'}^* e^{i(\omega_j - \omega_{j'} - \omega_R)t}}{\omega_j + W_{n2}}]\}. \end{aligned} \tag{2.50}$$

Here we have used $W_{n1} - W_{n2} = \omega_R$. If in the first two terms we let $j = j^{'}$, the third term let $j^{'} = j + 1$ and let $j^{'} = j - 1$ in the fourth term, we can eliminate the counter-rotating terms. We get:

$$\begin{aligned} i\hbar\frac{\partial C_1}{\partial t} &= -\frac{1}{4\hbar}\sum_{n=3}^{\infty}[C_1 P_{1n}P_{n1}\sum_j |V_j^2|(\frac{1}{W_{n1}+\omega_j} - \frac{1}{W_{n1}-\omega_j}) \\ &+ C_2 P_{1n}P_{n2}\sum_j(\frac{V_{j+1}V_j^* e^{i\triangle\omega t}}{\omega_j - W_{n2}} - \frac{V_j V_{j-1}^* e^{i\triangle\omega t}}{\omega_j + W_{n2}})] \\ &= -\frac{1}{4\hbar}\sum_{n=3}^{\infty}[C_1 P_{1n}P_{n1}\sum_j |V_j^2|(\frac{1}{W_{n1}+\omega_j} - \frac{1}{W_{n1}-\omega_j}) \\ &+ C_2 P_{1n}P_{n2}\sum_j V_j V_{j-1}^*(\frac{1}{W_{n2}+\omega_j} - \frac{1}{W_{n2}-\omega_{j-1}})e^{i\triangle\omega t}]. \end{aligned} \tag{2.51}$$

Here we used

$$\omega_j = \omega_0 + j(\omega_R + \triangle\omega) \tag{2.52}$$

$$\omega_j - \omega_{j-1} = \omega_R + \triangle\omega \tag{2.53}$$

$$\omega_{j+1} - \omega_j = \omega_R + \triangle\omega \tag{2.54}$$

and the term $(W_{n2} - \omega_{j-1})$ in Eq. 2.51 can be rewritten as $(W_{n1} - \omega_j + \triangle\omega)$.

Similarly we can write the equation for C_2 as:

$$\begin{aligned} i\hbar\frac{\partial C_2}{\partial t} &= -\frac{1}{4\hbar}\sum_{n=3}^{\infty}[C_1 P_{2n}P_{n1}\sum_j V_j V_{j-1}^*(\frac{1}{W_{n1}+\omega_j} - \frac{1}{W_{n1}-\omega_{j+1}})e^{-i\triangle\omega t} \\ &+ C_2 P_{2n}P_{n2}\sum_j |V_j^2|(\frac{1}{W_{n2}+\omega_j} + \frac{1}{W_{n2}-\omega_{j-1}})] \end{aligned} \tag{2.55}$$

Again the last term $W_{n1} - \omega_{j-1}$ can be rewritten as $W_{n2} - \omega_j - \triangle\omega$. Now we can write the equation for C_2, C_1 in the matrix form as:

$$i\hbar\frac{\partial}{\partial t}\begin{bmatrix} C_1 \\ C_2 \end{bmatrix} = \begin{bmatrix} H_{11} & H_{12}e^{i\triangle\omega t} \\ H_{21}e^{-i\triangle\omega t} & H_{22} \end{bmatrix}\begin{bmatrix} C_1 \\ C_2 \end{bmatrix} \tag{2.56}$$

Here

$$H_{11} = -\frac{1}{4\hbar}\sum_{n=3}^{\infty} C_1|P_{1n}|^2 \sum_j |V_j^2|(\frac{1}{W_{n1}+\omega_j} - \frac{1}{W_{n1}-\omega_j}) \quad (2.57)$$

$$H_{12} = -\frac{1}{4\hbar}\sum_{n=3}^{\infty} C_2 P_{1n}P_{n2} \sum_j V_j V_{j-1}^*(\frac{1}{W_{n2}+\omega_j} + \frac{1}{W_{n1}-\omega_j+\triangle\omega}) \quad (2.58)$$

$$H_{21} = -\frac{1}{4\hbar}\sum_{n=3}^{\infty} C_1 P_{2n}P_{n1} \sum_j V_j V_{j+1}^*(\frac{1}{W_{n1}+\omega_j} - \frac{1}{W_{n2}-\omega_j-\triangle\omega}) \quad (2.59)$$

$$H_{22} = -\frac{1}{4\hbar}\sum_{n=3}^{\infty} C_2|P_{2n}|^2 \sum_j |V_j^2|(\frac{1}{W_{n2}+\omega_j} + \frac{1}{W_{n2}-\omega_j}) \quad (2.60)$$

Next, we let

$$C_1' = C_1; C_2' = C_2 e^{i\triangle\omega t} \quad (2.61)$$

$$a_j = \frac{1}{2\hbar^2}\sum_n |P_{1n}|^2(\frac{1}{W_{n1}+\omega_j} - \frac{1}{W_{n1}-\omega_j}) \quad (2.62)$$

$$b_j = \frac{1}{2\hbar^2}\sum_n P_{1n}P_{n2}(\frac{1}{W_{n2}+\omega_j} + \frac{1}{W_{n1}-\omega_j+\triangle\omega}) \quad (2.63)$$

$$c_j = \frac{1}{2\hbar^2}\sum_n P_{2n}P_{n1}(\frac{1}{W_{n1}+\omega_j} - \frac{1}{W_{n2}-\omega_j-\triangle\omega}) \quad (2.64)$$

$$d_j = \frac{1}{2\hbar^2}\sum_n |P_{2n}|^2(\frac{1}{W_{n2}+\omega_j} + \frac{1}{W_{n2}-\omega_j}) \quad (2.65)$$

We finally arrive at the reduced 2×2 Hamiltonian:

$$i\hbar\frac{\partial}{\partial t}\begin{bmatrix} C_1 \\ C_2 \end{bmatrix} = -\frac{\hbar}{2}\begin{bmatrix} \sum_j a_j|V_j^2| & \sum_j b_j V_j V_{j-1}^* \\ \sum_j c_j V_j V_{j+1}^* & \sum_j d_j|V_j^2| - 2\triangle\omega \end{bmatrix}\begin{bmatrix} C_1 \\ C_2 \end{bmatrix} \quad (2.66)$$

When substantial coherence is prepared on a Raman transition, it modulates the incoming field, which adds multiple sidebands separated by the transition frequency, producing a wide comb of frequency components separated by the Raman frequency. The propagation equation for the qth Raman sideband, in a time frame moving with

a speed of light c is [6; 53]:

$$\frac{\partial E_q}{\partial z} = -j\eta\hbar\omega_q N(a_q\rho_{aa}E_q + d_q\rho_{bb}E_q + b_q^*\rho_{ab}E_{q-1} + b_{q+1}\rho_{ab}^*E_{q+1}). \tag{2.67}$$

Here η is the impedance of free space, N is the molecular density, and ρ_{ij} are the elements of the 2×2 density matrix. For an estimation, we use the following parameters for a numerical calculation. The refractive index of $PbWO_4$ crystal is known from reference [54]. Since $n_q = 1 + \beta_q\frac{\lambda_q}{2\pi}$, we get $\beta_q = \frac{2\pi(n_q-1)}{\lambda_q}$, $a_q = \frac{\beta_q}{\eta\hbar\omega_q N}$, $d_q = a_q$ and we use $b_q = -a_q/5$ as an approximation. $N = 1.096 \times 10^{22}$ for crystal $PbWO_4$. We assume partial coherence using $\rho_{ab} = 0.1$ (maximum is 0.5). The result is shown in Fig. 4. We can see at a short distance of 44.7 μm, there are many sidebands generated. The resultant pulse has a full width at half maximum (FWHM) of 0.64 fs.

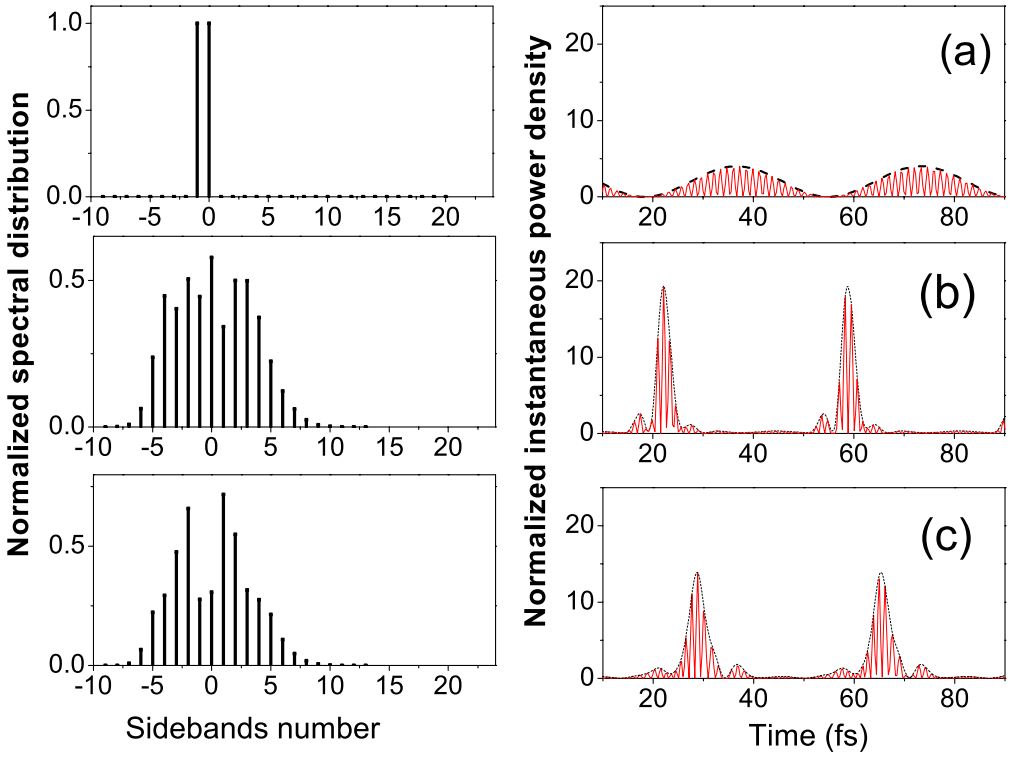

Fig. 4. Sidebands generated and instantaneous power density versus time in $PbWO_4$ crystal. The spectrum and temporal waveform for (a) z=0, (b) z=44.7 μm, the pulse produced has FWHM of 0.64 fs, (c) z=100 μm.

CHAPTER III

BROADBAND COHERENT LIGHT GENERATION IN RAMAN-ACTIVE CRYSTAL $PbWO_4$*

A. Introduction

Lead tungstate ($PbWO_4$) belongs to the tetragonal crystal system (space group of $C_{4h}^6 - I4_1/a$) with a scheelite structure. The unit cell parameters are a=b=5.456 and c=12.020 Å. $PbWO_4$ has attracted a lot of interests because of a plan to use it as a scintillation detector at the Large Hadron Collider in CERN [55]. As a stable, non-hygroscopic crystal and with low cost, $PbWO_4$ finds application as a material for Raman lasers. $PbWO_4$ has a wide optical transparency from 0.33 to 5.5 μm and a relatively large damage threshold. It has a high density of 8.23 g/cm^3.

$PbWO_4$ is a negative uniaxial crystal, i.e. the real part of the extraordinary complex refractive index n_e is lower than the ordinary one n_o (Fig. 5). The refractive index of $PbWO_4$ crystal can be fitted through the known experimental data [54] by using the Sellmeier equation [56] as following:

$$n_o(\lambda)^2 = 1 + (3.34558\lambda^2/(\lambda^2 - 0.0449397) - 5.41629 * 10^6\lambda^2/(\lambda^2 - 2.23428 * 10^7) - 6.87556 * 10^6\lambda^2/(\lambda^2 - 2.29655 * 10^7); \quad (3.1)$$

Fig. 5 also shows how the ordinary ray [polarized normal to the plane containing optical axis (c axis) and the laser wave vector k] and the extraordinary ray (polarized in the plane containing optical axis and the laser wave vector k) propagate in the

*Part of this chapter is reprinted from "Broadband coherent light generation in a Raman-active crystal driven by two-color femtosecond laser pulses," by M. Zhi and A. V. Sokolov, Opt. Lett. 32, 2251-2253 (2007), copyright 2007, with kind permission from Optical Society of America.

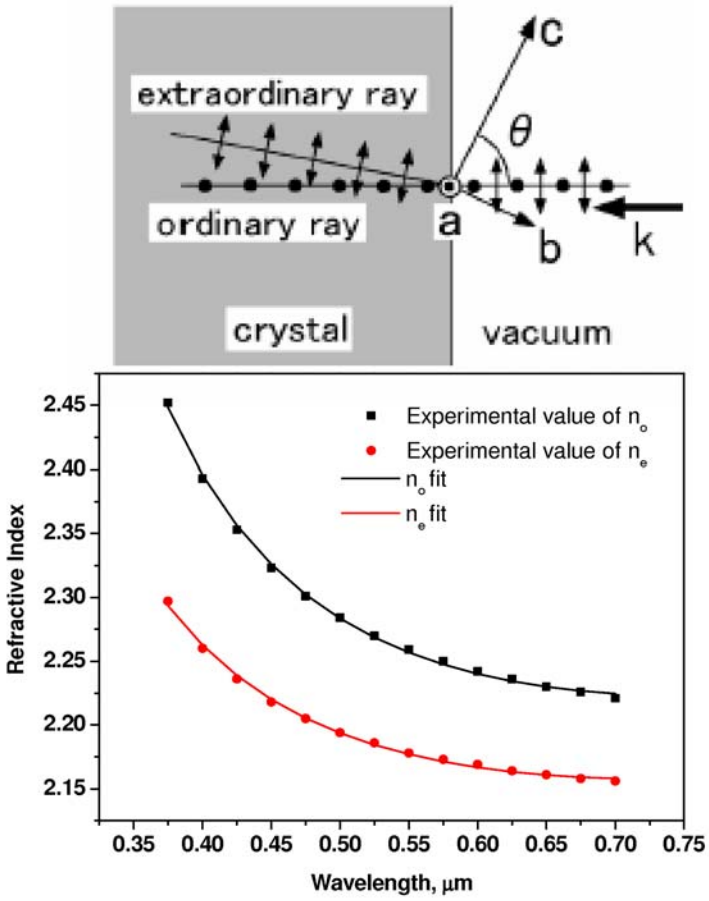

Fig. 5. (Top) propagation of the ordinary ray and the extraordinary ray in scheelite $PbWO_4$, a, b, c are the 3 axes of the crystal. k is the laser wave vector. θ is the angle between the optical axis c and the k. (Bottom) the refractive index of the two rays.

crystal [57].

Since $PbWO_4$ is a popular Raman crystal material, its Raman spectra have been measured and studied in detail [58; 59]. The excitation geometry in the reference is described by four symbols, two inside a parenthesis and two outside, for example, a(cc)a. The symbols are, left to right, the propagation direction, the polarization of the incident beam, the propagation direction, and the polarization of the scattered beam [60]. We measure the Raman spectrum of $PbWO_4$ using our sample and the

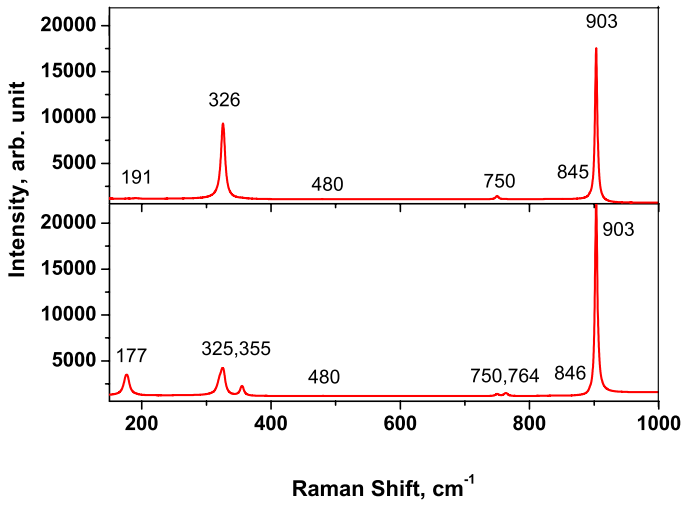

Fig. 6. Raman spectrum of the $PbWO_4$ crystal at two different orientations using a CCD camera (ISA Jobin YVon U1000). The spectrometer grating has a groove density of 1800 grooves/mm. This measurement has a 1 cm^{-1} accuracy.

result is shown in Fig. 6. The Raman spectrum should correspond to a mixture of polarizations perpendicular and parallel to the c-axis because of our sample orientation. It is dominated by a mode at 903 cm^{-1} with linewidth $\Delta\nu_R$=4.3 cm^{-1}, which corresponds to a phonon relaxation time of 2.5 ps [58]. This intense Raman line corresponds to the totally symmetric (breathing) A_g optical modes of its tetrahedral WO_4^{2-} ions [30]. Another relatively strong Raman line at 325 cm^{-1} has a linewidth of 7.5 cm^{-1} which is almost comparable to the width of 903 cm^{-1} line for a certain crystal orientation (Fig. 6). This mode is one of the internal modes of the WO_4 molecule [59].

B. Experimental setup

The schematics of the setup is shown in Fig. 7. The seed laser (Mira, Coherent) is a mode-locked (Kerr Lens Mode-locking) ultrafast laser that produces ultrashort,

wide bandwidth (>50 nm), fs pulses (<20 fs) using Ti:Sapphire as the gain medium. The output pulse has a repetition rate of 76 MHz with a wavelength at 800 nm. The pulses are used to seed an amplifier (Legend, Coherent). The pulse is first stretched by a grating to about 200 ps and then is amplified by a Ti:Sapphire regenerative amplifier system pumped by a pulsed, frequency doubled Nd:YLF laser at 523.5 nm. It is compressed afterwards by the grating compressor to a pulse with energy >1.0 mJ at a 1 kHz repetition rate and pulse duration of <35 fs FWHM. The energy stability is <1% RMS. This amplified pulse is used to pump two computer-controlled optical parametric amplifiers (OPerA, Coherent). It is first down-converted to a signal pulse (the short wavelength, 1150-1600 nm) and an idler pulse (the long wavelength, 1600-2630 nm) by a parametric process. These pulses obtained from the two OPAs can be frequency doubled or mixed with the fundamental pulses to produce up to 30 μJ per 50 fs Gaussian pulse at tunable visible wavelengths. For example, the SHG of the signal beam will produce pulses with wavelength ranging from 575 to 800 nm. The sum frequency generation (SFG) will produce pulses with wavelength range from 533 to 613 nm. These pulses are commonly used in our experiment. We typically use 1 to 2 μJ per pulse focused to about a 100 μm size spot at the sample. This laser intensity is right below the onset of (strong) SPM. We use a $10 \times 10 \times 1$ mm^3 $PbWO_4$ sample, with the large surface perpendicular to the a-axis of the crystal. The laser beams are typically sent perpendicular to the large surface and crossed at the crystal after the focal lens with a small angle θ, which varies from 2 to 7 degrees. The retro-reflectors in one or two beams (if a probe beam is used) are mounted on a motor controlled translation stage so that the delay between the pulses can be varied with a precision of 1 μm, which is about 6.7 fs. The spectra are measured with a fiber-coupled spectrometer (Ocean Optics, USB 2000, slit size 25 μm, measures wavelength ranging from 180 to 870 nm), which has an average optical resolution of 1.4 nm, with

a slightly higher resolution in the visible region. The wavelengths we gave are the peak value readings which are taken with an integration time about 100 ms (which means average over 100 pulses).

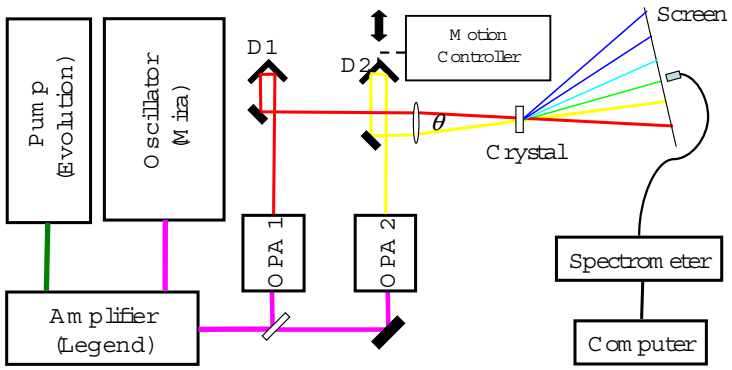

Fig. 7. Experimental setup. D1, D2 are retro-reflectors. D2 is mounted on a motor–controlled translation stage. OPA: Optical Parametric Amplifier. We take the pictures of the sidebands projected on the screen. The spectra are measured with an Ocean Optics fiber-coupled spectrometer.

C. Broadband coherent light generation in Raman-active crystals using two-color laser fields

Our crystal is a-cut, i.e. the axis perpendicular to the large area is the a-axis (see Fig. 11 top). The c-axis of the crystal is found by measuring the GDD at a few pump wavelengths at two orientations. We first find the zero delay between the pulses using the FWM signal in glass (Here zero delay is defined at the point where the FWM signal is maximized). Then we insert the crystal to the beam and the difference between the two zero delays gives the GDD at the wavelength of this beam. The GDD measured at one orientation with pulse wavelengths at 604 nm, 730 nm and 800 nm is 5400 fs, 5047 fs and 4627 fs, respectively. They are 4860 fs, 4607 fs and

3287 fs at an orientation which is 90^o from previous measurement. Comparing the measured value of the GVD to the calculated ones we can then identify the c-axis since $PbWO_4$ is a negative uniaxial crystal. The interaction length is about 0.5 mm when a pair of visible pulses with wavelengths of 640 nm and 580 nm is used. It is about 1 mm when a pair of pulses in the IR region with wavelength of 800 nm and 730 nm is used.

In this section, I discuss broadband sideband generation in Raman-active crystals by exciting two strong modes, 903 cm^{-1} and 325 cm^{-1}, respectively.

1. Generation by excitation of the strong Raman mode at 901 cm^{-1}

Highly efficient 1.3 μm second-Stokes $PbWO_4$ Raman laser has been constructed by Gad *et al.* [61] and the high order Stokes (S) and anti-Stokes (AS) generated lines in $PbWO_4$ crystal under 100 picosecond (steady state regime, pulse duration $\tau_p >> T_2 = (\pi c \Delta\nu_R)^{-1}$) laser excitation have been observed by Kaminskii *et al.* [30]. Using two-color ultrashort pulses (transient regime, $\tau_p >> T_2$), we observe efficient generation of many sidebands in $PbWO_4$ when two pulses (λ_1= 620 nm, λ_2= 588 nm, $\delta\omega$= 930 cm^{-1}) with parallel polarizations are crossed at the crystal with an angle of 4 degrees (Fig. 8). The sidebands emerge spatially well-separated and have the same polarization as the two input beams. Up to 20 AS and 2 S sidebands are observed on a white paper screen which is put about 25 cm away from the crystal (Fig. 8 top). The spectrum of the first 6 AS and the higher order sidebands (AS 12 to AS 16) is shown in Fig. 8 (bottom). The spectra of the lower-order sidebands show a rich structure, due to simultaneous excitation of several Raman lines by the large spectral width of the fs laser pulses. Takahashi has observed a similar effect in his study of $YFeO_3$ crystals [62]. The frequency spacing between the sidebands decreases gradually and reaches about 450 cm^{-1} at the highest orders measured, to

our surprise.

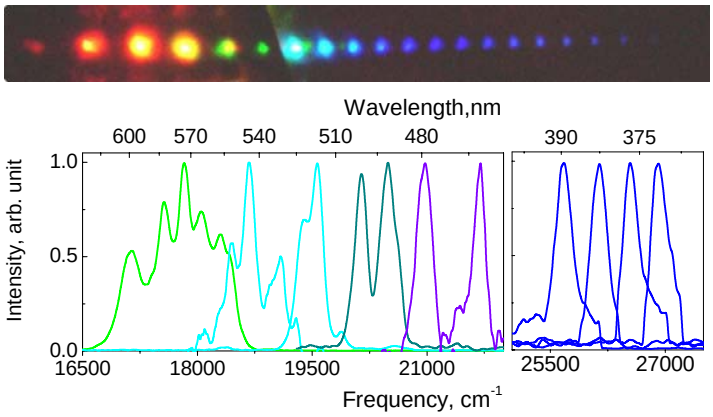

Fig. 8. Broadband generation in $PbWO_4$ crystal with two pulses (at 588 nm and 620 nm) applied at an angle of 4 degrees to each other. Top: generated colors projected on a white paper screen. The two input pulses (bright yellow and red spots), two S and two AS are attenuated by an neutral-density filter. Note that the line connecting the color spots has a slight cusp at intermediate AS orders. Bottom: spectra of the generated sidebands (left: AS 1 to AS6; right: AS 12 to AS 16). The frequency spacing between the sidebands at higher orders decreases gradually.

To prove the Raman-resonant nature of sideband generation, and to separate the effect of instantaneous FWM, we tune the difference between the two applied laser frequencies ($\delta\nu$), and measure the generated AS frequencies. Fig. 9 shows these generated frequencies as a function of the angle at which sidebands emerge from the $PbWO_4$ crystal. We perform this measurement at a relatively large input beam crossing angle of 6 degrees. At this angle, and at sufficiently large $\delta\nu$ (1804 or 2002 cm^{-1}), the generated AS 1 beam splits into two slightly separated distinctively colored beams: one corresponding to (non-resonant) FWM, and the other (which is much brighter) corresponding to Raman-resonant AS generation. By moving the fiber tip of the spectrometer to the location shown in Fig. 9 (insert) by an arrow, we

measure the FWM frequency (as opposed to the Raman-shifted frequency measured at the center of the main AS 1 beam). We observe that as we vary $\delta\nu$ from 844 to 2002 cm^{-1}, the Raman sidebands are generated at approximately the same angle and with roughly the same frequency shift from the previous order, while the FWM frequency varies as $\nu_{FWM} = 2\nu_2 - \nu_1$. The observed decrease in the frequency spacing between higher-order sidebands is likely due to phase matching.

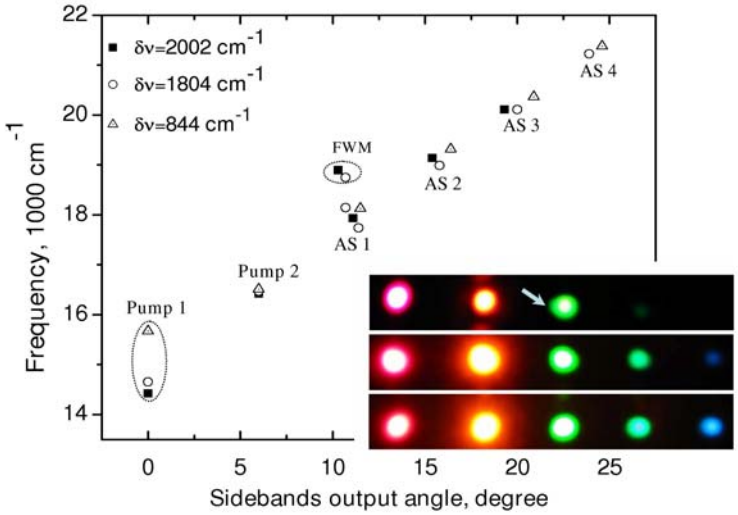

Fig. 9. Peak frequency of the generated sidebands, plotted as a function of the output angle. One input frequency (pump 2) is fixed while the $\delta\nu = \nu_2 - \nu_1$ is tuned to 844 cm^{-1} (triangles), 1804 cm^{-1} (circles), and 2002 cm^{-1} (squares) respectively. The FWM frequency (measured at the point shown on the insert by the arrow) varies as $\nu_{FWM} = 2\nu_2 - \nu_1$ while the Raman sideband frequencies stay approximately fixed. The insert shows the output beams projected onto a screen, for these same values of $\delta\nu$ (varying from 2002 to 844 cm^{-1} top to bottom).

When we vary the angle between the pump and Stokes beam from 3 to 6 degree, we observe substantial changes in both the AS frequency shifts (Fig. 10), and in the conversion efficiency. No AS conversion is observed when collinear input beams are

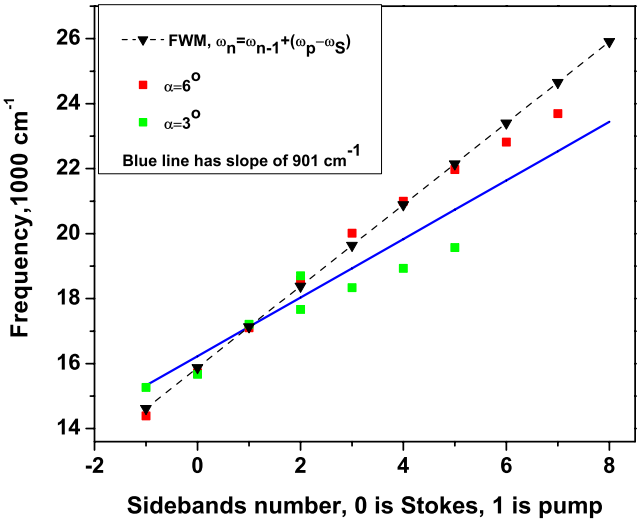

Fig. 10. Sidebands generated in $PbWO_4$ crystal when the two pulses (at 588 nm and 620 nm) are applied at an angle of 3 and 6 degrees to each other. The generated frequencies have different spacings.

used. We measure optimal AS conversion (for $\delta\nu$= 930 cm^{-1} in $PbWO_4$) when the angle between the applied beams is 4 degree. When the angle is further increased, AS conversion efficiency goes down, while the frequency separation of the AS sidebands goes up. Even though at a larger beam crossing angles the conversion efficiency is expected to decrease because of the reduced beam overlap, for angles below 6 degrees it is the phase matching, along with the spectrum of exited Raman transitions, that determines the conversion efficiency and the frequencies generated in thin crystals. Apparently, phase matching plays a critical role by selecting the direction (Note the slight bending of the plane in which the generated beams lie in Fig. 8, top) and frequency of the generated sidebands in Raman-active crystals (as compared to the collinear Raman generation in gasses [6; 7]). More quantitative calculation will be given in the next chapter where the generation in the isotropic crystal diamond is

discussed.

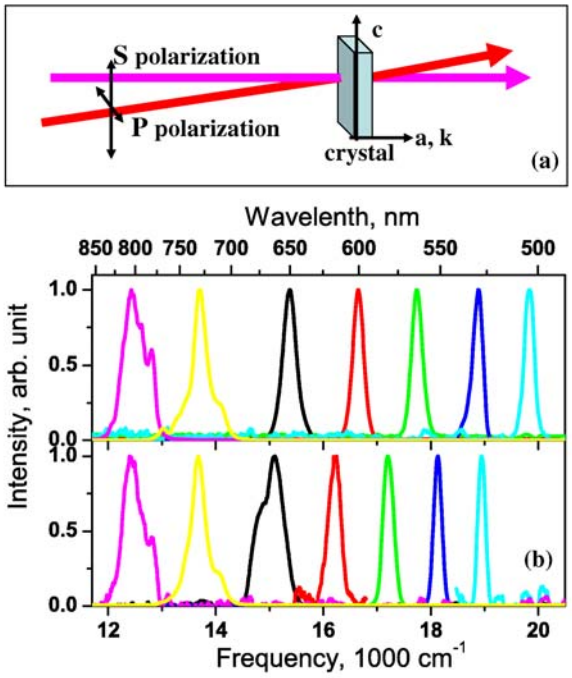

Fig. 11. (a) Crystal orientation and the two possible polarization of the laser beams. (b) Two pump beams and the first 5 AS generated in the $PbWO_4$ crystal when two pulses (at 729 nm and 805 nm) are applied at two different polarizations P (top) and S (bottom, a(cc)a excitation geometry). The sideband frequencies have different frequency spacings.

The generation is also very sensitive to the polarization of the beams. First of all, it has been shown that the Raman gain is strongly peaked when the crystal is excited by a beam whose polarization is parallel to the c-axis of the crystal in the SRS experiment [30]. Secondly, we find that the generation is best when the pump and Stokes beams have the parallel polarization, which is either parallel or normal to the c-axis. Thirdly, the generation has different frequency spacing when the polarization of the pump beams are parallel with different axis of the crystal as shown in Fig. 11. When we change the polarization of the input beams from S (the polarization

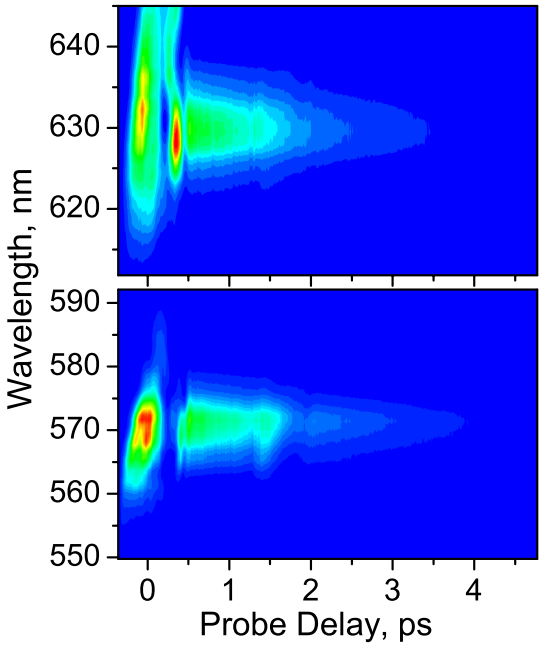

Fig. 12. The CARS/CSRS signal as a function of the probe delay. There is a gap between the strong FWM signal and long-live CARS signal.

is parallel to the plane containing the optical axis c and the wavevector k, see Fig. 11 (a)) to P (perpendicular to S), we observe a significant variation in the generated frequency spacing. We speculate that this is the result of dispersion since when P polarization is used, the crystal sees refractive index of n_o (larger than n_e). We also observe a gap in the probe delay time between the FWM signal and the CARS signal as shown in Fig. 12 which remains a mystery to us.

2. Generation by excitation of the Raman mode at 325 cm^{-1}

As we have mentioned in the introduction, with fs pulse pumping, the SRS gain increment explicitly depended on the integral cross section instead of the peak cross section of spontaneous Raman scattering [9] therefore the excitation of 325 cm^{-1} line

can dominate when phase matching is satisfied. When we reduce the angle between the pump and Stokes beams to 2.9 degree and tune the frequency difference below 600 cm^{-1}, we observe generation due to excitation of the Raman mode at 325 cm^{-1} as shown in Fig. 13 (top row in each picture). Due to the small phase matching angle between the two input pulses, the output beams are very close to each other and become inseparable for high-order sidebands. We see the interplay between the phase matching and Raman resonance when we fix the Stokes pulse at 804 nm wavelength while tunning the pump pulse from 760 to 780 nm, with a detuning varying from 408 to 615 cm^{-1}. Although it is far from Raman resonance at 615 cm^{-1} detuning, the phase matching condition between the pump and Stokes is satisfied, which results in generation of 22 AS and 2 S. The phase matching between the pump and probe fields is also good, as can be seen from the FWM signal (blue) shown in the picture. As many as 10 CARS signals are measured, which indicates a significant coherence being built up in the crystal.

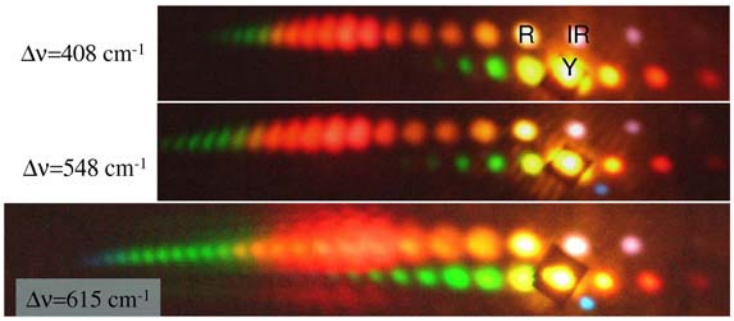

Fig. 13. Broadband generation in $PbWO_4$ crystal with Stokes pulses at 804 nm and pump pulse tuned with the detunings vary from 408 to 615 cm^{-1} (top row in each picture). The angle between the pump and Stokes beam is 2.9 degree. A third probe pulse (Y) leads to generation of many orders of CARS and CSRS signals (bottom row in each picture).

The frequencies of the sidebands generated by the pump (at 760 nm) and Stokes pulses (at 804 nm) are plotted as a function of the sideband order (Fig. 14). The frequency spacing decreases slightly as the order goes higher. In the same figure, we also plot the many orders of CARS signals generated by all three pulses. We can see that the CARS signal has a regular frequency spacing of 345 cm^{-1}, which is close to the spontaneous Raman frequency measured at 325 cm^{-1}. Because of the lower frequency spacing between the two pumps and the wide spectral width of the fs pulses, the smaller rotational modes are all excited so that the lower order sidebands have multiple peaks. This is different from the multiple peaks generated when 901cm^{-1} transition is excited. Those multiple peaks are due to the coexistence of the FWM and Raman signals. The high-order sidebands are about equally spaced at a 320 cm^{-1} spacing. The angle between the two applied beams is 2.5 degree, which corresponds to 1.2 degrees inside the crystal. Therefore it might be possible to generate sidebands using a collinear configuration of the two pump beams.

When the angle between the two pump beams is small and the frequency spacing is close, there is an overlap of the pump and Stokes pulses in the spectral domain. This overlap in spectra leads to a strong interaction between the pulses due to the Raman amplification process as shown in Fig. 15. We also observe this amplification process due to 903 cm^{-1} mode as shown in Fig. 16, where the pump and Stokes spectra are plotted as a function of the pump (Red) delay. It shows that the amplified spectra of the pulse sweeps from low to high frequency. This interesting feature depends on the timing between the two pulses and the cause of it needs further investigation.

When the 325 cm^{-1} is excited with pump pulse at 770 nm and Stokes pulse at 805 nm, we observe something interesting as shown in Fig. 17 (b). The AS 3 is much stronger than AS 1. What happens can be explained by a schematic energy level diagram as shown in Fig. 17 (a). The Raman mode width in the crystal is larger than

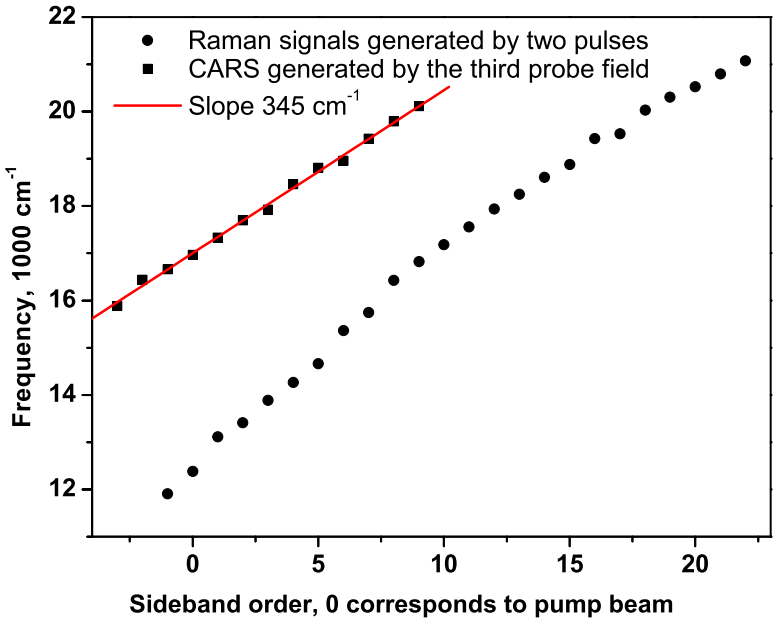

Fig. 14. The frequency of the sidebands generated by the pump at 760 nm and Stokes at 804 nm (round dots) and the frequency of the many orders of CARS signal generated by all three pulses as the function of sideband number. The frequency spacing generated by two pulses decreases slightly as the order goes higher. The CARS signal has a regular frequency spacing of 345 cm^{-1}.

the one in a gas. Consequently, although ω_{R1}=903 cm^{-1} is not exactly three times the ω_{R2}=325 cm^{-1}, it is still possible that the AS 3 gets enhanced by the Raman mode at 903 cm^{-1}. A clear indication is shown in Fig. 17 (c) where a third probe beam is used. The picture is taken with a delayed probe, therefore only CARS signal can survive. The CARS 3 signal, which is generated due to excitation of 901 cm^{-1}, is very strong, compared to the CARS 2 signal.

The long coherence decay time of the CARS signal (compared to the instantaneous FWM) gives an indication of which Raman mode is excited. We see many Raman modes are excited when we measure the CARS 1, 2 and 3 as a function of

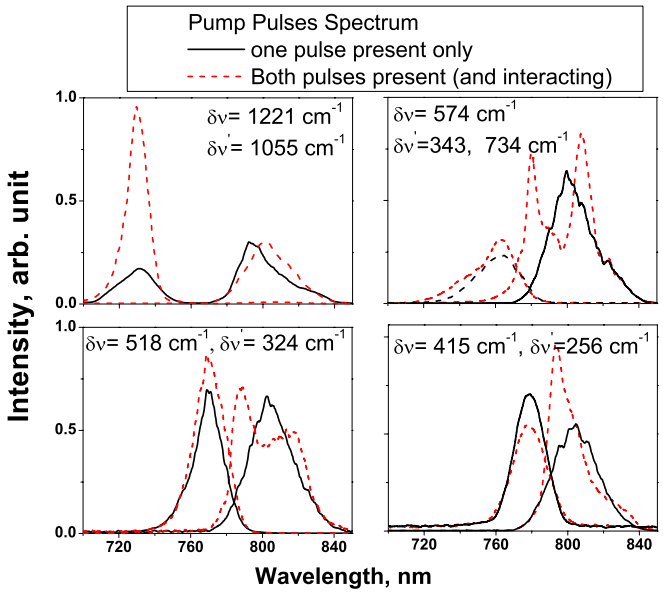

Fig. 15. The Raman amplification process. Solid curve, spectrum of the pump (Stokes) pulse measured by blocking the Stokes (pump) pulse, with the detuning $\delta\nu$. Dashed line, spectra of the pump and Stokes pulses measured with the presence of each other. The spectrum changes dramatically (the frequency spacing changes to $\delta\nu'$) when certain Raman mode is excited, due to the Raman amplification process.

probe delay as shown in Fig. 18. We see a modulation of the probe pulse in CARS 1 signal. After data processing and the subtraction of the probe beam, we see a beating signal which corresponds to the small-frequency Raman mode at 59 cm^{-1} beating with the probe beam. There are also frequencies generated due to the excitation of the Raman modes at 179 and 359 cm^{-1} in CARS 1. The signal with frequency shift of certain Raman frequency is maximized at a phase-matched angle, as can be seen from the CARS 2 and CARS 3 signals, both of which are generated due to the excitation of the other two Raman modes (760 and 903 cm^{-1}). In CARS 2 the frequency which has a shift of 760 cm^{-1} is stronger because the output angle of the CARS 2 signal is

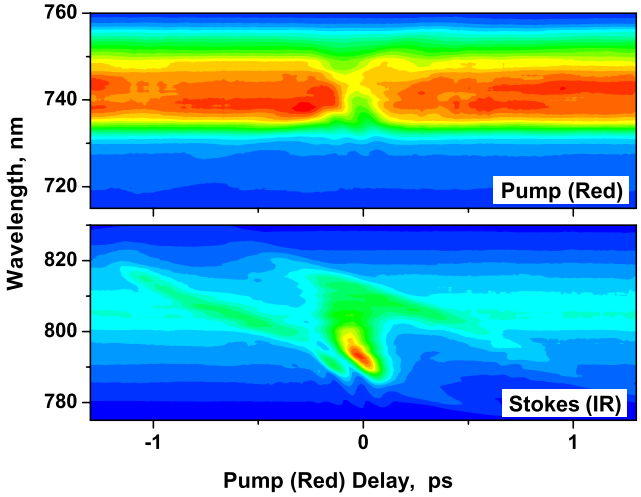

Fig. 16. The spectra of the pump and Stokes pulses as a function of the relative time delay. The spectra changes drastically when the two pulse overlap.

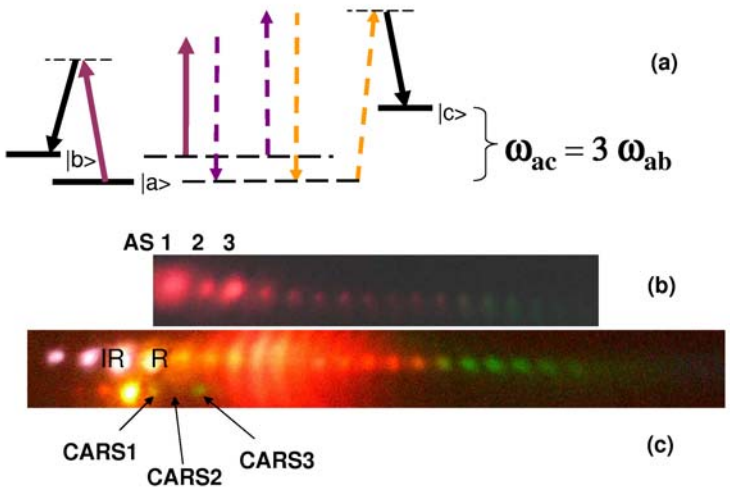

Fig. 17. (a) Energy level schematics; (b) The AS 3 generated by pump and Stokes beams which are tuned to excite the Raman mode at 325 cm^{-1} is stronger than AS 2 due to the excitation of Raman mode at 903 cm^{-1}; (c) CARS 1, 2 and 3 signals generated by a delayed probe pulse.

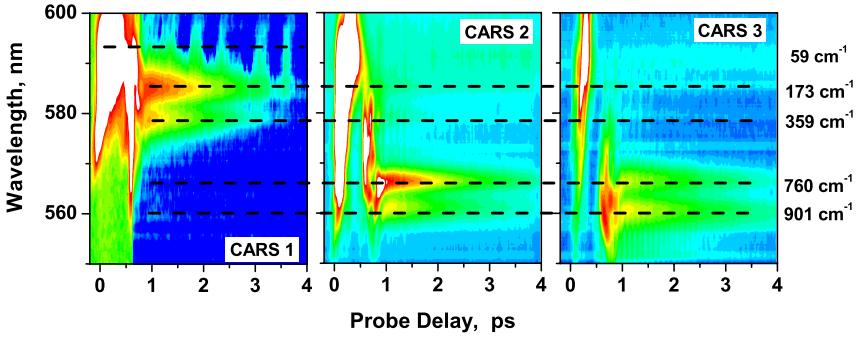

Fig. 18. Measurement of the CARS 1, 2 and 3 coherence decay by using a third probe beam. Many Raman modes are excited.

more phase-matched at this frequency. It is an opposite situation in CARS 3 where the signal with a Raman shift of 903 cm^{-1} is stronger.

D. Broadband coherent light generation in the Raman-active crystal using three-color laser fields

With two pulses, the number of the generated sidebands we observe is limited to about 22 when fs pulses are used. We have tried different ways to obtain more sidebands. Here I show two schemes with the additional third probe pulse irradiation on the sample. First one is a planar configuration, where a third pulse is sent in the direction of one of the sidebands generated by pump and Stokes pulses. The second scheme is a Box CARS configuration [49] where the three beams are sent in at the three corners of a box and the CARS signal is generated in the fourth corner. The difference here is that the third probe pulse is phase-matched with one of the sidebands generated by the pump and Stokes beams (instead of the pump or Stokes beam itself). This leads to a 2-D color array generation.

1. Planar configuration

We first generate sidebands using pump pulses at 755 nm and Stokes pulses at 803 nm as shown in Fig. 19 (a). Then we send the third beam (which we also call probe beam) at 590 nm at the same direction and wavelength as AS 6. The configuration is shown in Fig. 19 (b). The probe beam and the pump beam satisfy the phase matching condition so that a strong FWM (green) is efficiently generated, which is used as a seed to generate high-order sidebands (Fig. 19 (c)). So with three pulses, more sidebands are observed and the intensity of the high-orders is enhanced. The probe beam is converted into the sidebands with a 25% efficiency [Please not that we define the overall conversion efficiency from a pump beam to the sidebands in a following way. We first measure the power of the beam after the crystal while blocking the other pump beam (therefore no sideband generation) and call it P1. Then we measure the power of the same beam with the other pump beam present (with sideband generation) and call it P2. We call $\frac{P1-P2}{P1}$ as the conversion efficiency. This definition is used through the whole dissertation. We define a conversion efficiency to a specific order by $\frac{Psideband}{P1}$, with Psideband as the power of this specific order sideband.].

We then send in a probe beam at 543 nm to overlap with a higher order (AS 8) generated by the pump and Stokes beams as shown in Fig. 20. However, the probe beam is poorly phase-matched to the pump beam so there is no FWM (blue) generation that can be used as a seed. Consequently, although high-order sideband intensity is increased, their number only increases slightly. The sideband conversion efficiency for the probe beam is only 5%. The phase matching condition between the probe beam and the AS 1, 2, 3 generated from the pump and Stokes pulses only, which leads to the double peaks in the spectra of the higher order sidebands (AS 12, 13 and 14). We again see the importance of phase matching for the sideband

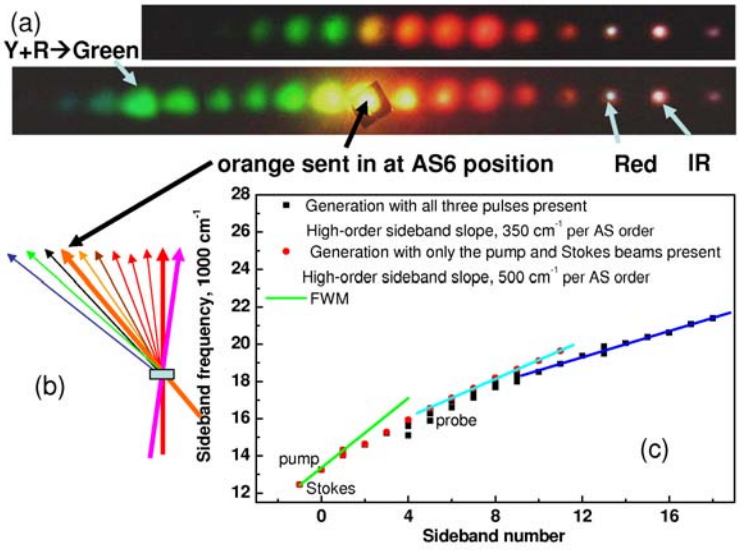

Fig. 19. Broadband pulse generation using three pulses in a planar configuration with the probe pulse sent in at the same direction and wavelength as AS 6. (a) Generation pictures with pump and Stokes beams present (top picture) and all three pulses (pump, Stokes and probe) present (bottom). (b) Input beam geometry. (c) The sideband frequency as a function of the sideband order generated by two/three pulses.

generation.

2. Box CARS configuration

We observe two-dimensional (2-D) multicolor Raman generation (Fig. 21 (b)) when we apply Red (730 nm) as a pump beam, Infrared (804 nm) as a Stokes beam, and Yellow (604 nm) as a probe beam in a Box CARS configuration as shown in Fig. 21 (a). The angle between the pump and Stokes beams is 5 degrees. The probe beam is 11 degrees from the pump beam and 16 degrees from the Stokes beam. When the probe beam angle changes, the 2-D multicolor Raman generation pattern changes dramatically: longer wavelength is generated more efficiently as shown in Fig. 21 (c).

When we increase the angle between the pump and Stokes input beams to 6

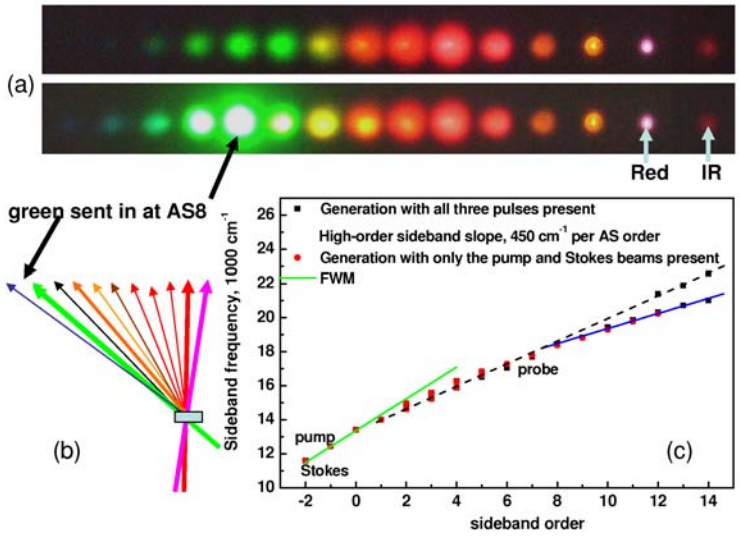

Fig. 20. Broadband pulse generation using three pulses in a planar configuration where the probe pulse is sent in at the same direction and wavelength as AS 8. (a) Generation pictures with pump and Stokes beams present (top picture) and all three pulses (pump, Stokes and probe) present (bottom). (b) Input beam geometry. (c) Sideband frequencies generated by two/three pulses. Dashed line: Probe beam mixed with AS 1, 2, 3 that are generated from pump and Stokes pulses only. As a result, AS 12, 13, 14 have distinct double peaks. (we were very confused when we measured this.)

degree while keeping the probe beam fixed, we observe up to 50 new generated colors. We see that the IR and R generation is strongly affected by the yellow probe pulse. In Fig. 22 (b) we show pictures of the first four AS with yellow probe beam present and absent. We see that the addition of the probe beam not only leads to the generation of new colors, it also affects the interaction between pump and Stokes pulse. Three things happen: (1) the generated pulse spectrum gets broader; (2) the signal gets stronger; and (3) new frequencies appear as shown in Fig. 22. The top picture is obtained with all three beams present at the input. AS 3 has two colors, the yellow part is from three beam interaction while the green part is from IR and R interaction alone. If we change the probe Yellow delay so that the pulses don't overlap in time,

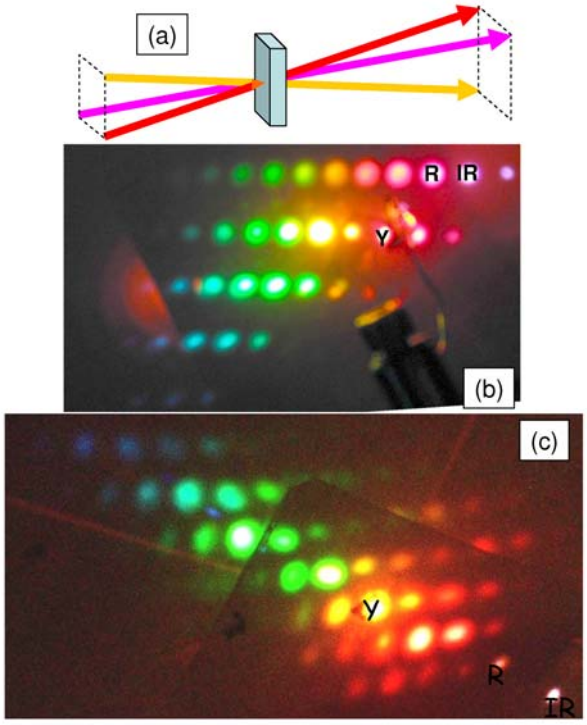

Fig. 21. (a) The Box CARS configuration. Three beams are sent in at the three corners of the box and the CARS signal is generated in the fourth corner. (b) and (c) Different 2-D patterns generated in $PbWO_4$ under different input angles (phase matching condition). The third probe pulse phase-matches with the different order of the AS generated by the pump and Stokes pulses.

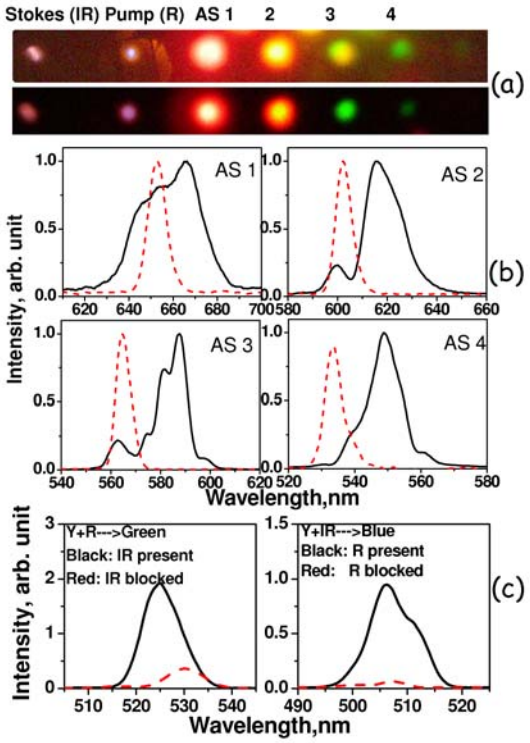

Fig. 22. (a) Top, the AS beams generated by the pump (R) and Stokes (IR) pulses with the probe (Y) pulse present; Bottom, The beams generated by the pump and Stokes pulses only. (b) solid line: AS sidebands generated by the three pulses; dashed line: AS sidebands generated by the pump and Stokes pulses only. (c) Left, FWM of the pump and probe pulses with the Stokes pulse present (solid line) and absent (dashed line); Right, FWM of the Stokes and probe pulses with pump pulse present (solid line) and absent (dashed line).

the AS fields are not affected by the Yellow pulse.

Overall, the 2-D generation is a very complicated process. It is even more difficult to assign the generated fields when several Raman modes are excited at the same time in the crystal. However, when an isotropic material such as diamond is used, we are able to understand that the generation is due to Raman, FWM and six wave mixing processes, as we will show in the next chapter.

E. Study of $PbWO_4$ properties

As mentioned earlier, $PbWO_4$ was studied earlier for the purpose of using it as a scintillation material and later as a Raman crystal material. For broadband generation, we study a few things about this crystal using fs pulses. This research is new and some of the results are easy to interpret while others need further investigation.

1. Coherent CARS decay and quantum beating

When using a third probe beam, we measure the coherence decay time of the CARS signal with a Raman shift of 903 cm^{-1} as shown in Fig. 23. The CARS and CSRS signal has a decay time of 1.3 ps while the 2nd order CARS signal has a decay time of 0.7 ps.

When a fs pulse are used as a probe, we observe the quantum beating between the two modes, which have a frequency difference of 565 cm^{-1}. The corresponding beating period in the time domain is 59 fs, which is what we measure as shown in Fig. 24 (a). The CARS signal can be described by the following formula [63]:

$$\begin{aligned} I_{CARS} &= |Ae^{-t/T_2} + Be^{i\triangle\omega t - t/T_2^{'} + i\varphi}|^2 \\ &= A^2e^{-2t/T_2} + B^2e^{-2t/T_2^{'}} + 2ABe^{-t(1/T_2+1/T_2^{'})}\cos(\triangle\omega t + \varphi). \end{aligned} \tag{3.2}$$

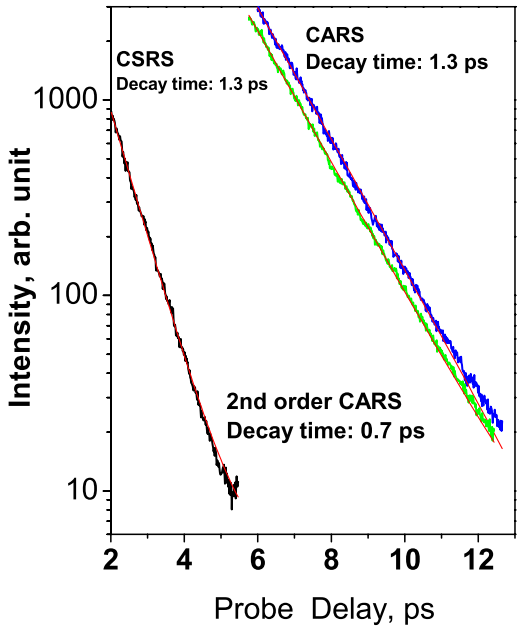

Fig. 23. Coherence decay measured through CARS, 2nd order CARS and CSRS for the Raman mode at 901 cm^{-1}. CARS and CSRS signal has the same coherence decay time of 1.3 ps. The 2nd order CARS has a decay time of 0.7 ps.

By fitting the experimental data (Fig. 24 (b)) with the above equation, we get T_2=1.3 ps, T_2'=3.8 ps, and ω=106.5 rad/ps, which is exactly the frequency difference between the two modes ($2\pi/T = 2\pi * (3/100 * 565cm^{-1}) = 106.5$).

When we use a narrow-band shaped probe beam (spectral width of about 1 nm), we are able to measure the coherence decay of the two strong modes in the crystal as shown in Fig. 24 (c). Here the measured decay time for Raman mode at 328 cm^{-1} is 1.5 ps and 2.5 ps for 901 cm^{-1} mode. The discrepancy between our two measurements could be due to the finite pulse width.

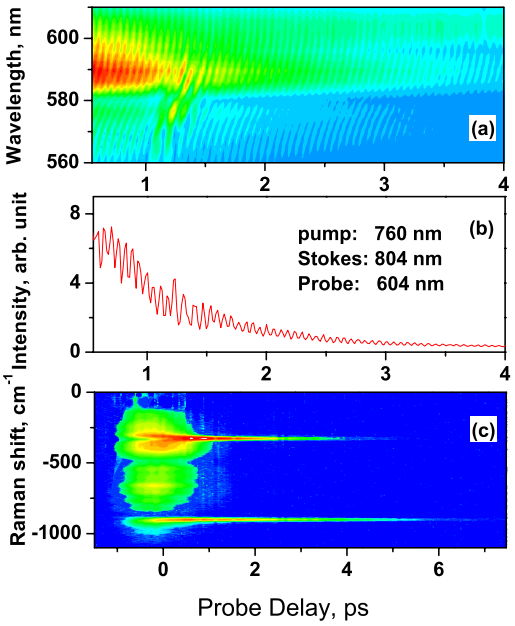

Fig. 24. (a) Quantum beating between the two strong Raman lines in $PbWO_4$ measured by using a fs probe pulse with $\triangle\nu$ between pump and Stokes pulses equal to 720 cm^{-1}. (b) The cross section from (a), which can be used to get the fitting parameters. The beating has a frequency of 106.5 rad/ps, which corresponds to the Raman shift difference of 565 cm^{-1} between the two modes. (c)The coherence decay of the simultaneously excited strong Raman lines measured when fs pump, Stokes pulses and a narrow-band ps probe (about 1 nm spectral width) are applied to the crystal.

2. UV absorption

When a UV probe is used, we observe strong absorption of the UV beam when the pulses overlap in time as shown in Fig. 25 (a). The exact origin of this absorption is unknown, but most likely it is related to a two-photon electronic excitation process. We identify that the width of the absorption dip is related to the group dispersion delay of the different pulses. We measure that the pump beam at 608 nm gets delayed about 5.1 ps (1.524 mm delay) while the Stokes beam at 700 nm has a delay of about

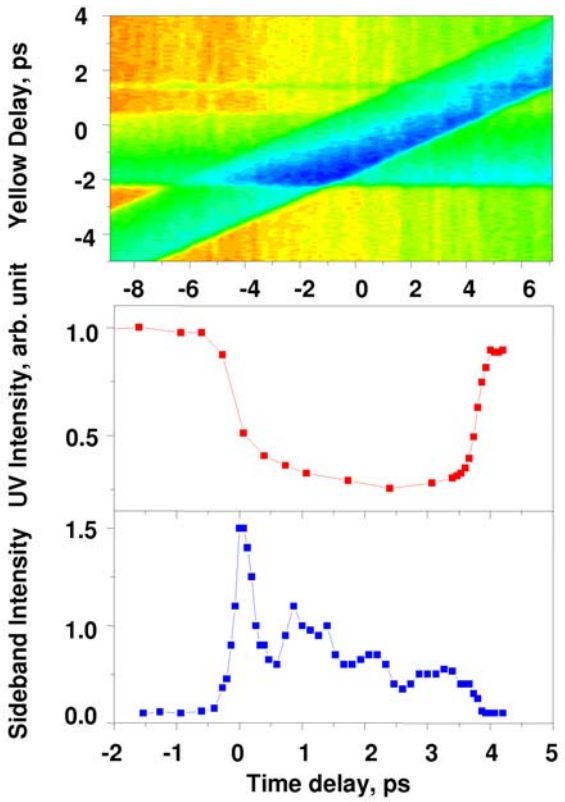

Fig. 25. UV probe pulse intensity as a function of probe delay and pump delay. When three beams overlap in time, the UV gets absorbed. (b) cross section of (a) at a zero delay of the pump pulse. The dip width corresponds to the group velocity delay of the pump and probe pulses. (c) CARS signal.

5.0 ps (1.494 mm). The UV beam at 350 nm experiences large dispersion which results in a delay of 8.62 ps (2.586 mm). The difference is about 3.6 ps, which is exactly the width of the dip we see in Fig. 25 (b). In Fig. 25 (c) we show that the CARS signal starts at the front edge where the pulses begin to overlap and exhibits quantum beating due to the simultaneously excited Raman modes.

3. The interference experiment

Next we investigate the mutual coherence among the generated sidebands. We first generate multiple AS sidebands by focusing Red (λ_R= 718 nm) and IR (λ_{IR}= 812

nm) beams into the $PbWO_4$ crystal. Then a third (Yellow) beam is sent along the direction of the generated AS 3 sideband with a matching wavelength ($\lambda_Y = 574$ nm). Once the overlap in frequency, space, and time is achieved, the sidebands (AS 2 to AS 7) start to visibly flicker, due to interference between signals generated through different channels. We measure the pulse energy of AS 5 on a shot-by-shot basis by using a fast photodiode.

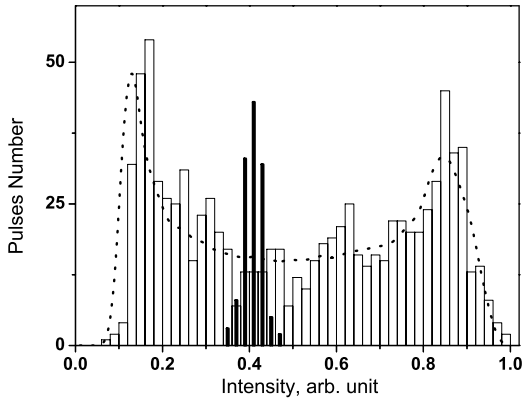

Fig. 26. Histograms of AS 5 pulse energy. Solid black bars: the number of pulses (out of 150) vs. AS 5 pulse energy generated with Red and IR input beams only. White bars: the histogram of AS 5 pulse energy (913 pulses total) with the addition of the third input beam. The dotted curve is a theoretical prediction obtained assuming perfect single-shot coherence of the two interfering fields, and random shot-to-shot variation of their relative phase.

The statistics of the AS 5 pulse energy is shown in Fig. 26. Solid black bars give the histogram (number of pulses vs. AS 5 energy), with only Red and IR pulses applied at the input. This histogram shows a typical normal distribution, with about 10% average variations. However, with the addition of the Yellow beam at the input, the histogram of the AS 5 pulse energy (913 pulses total) transforms into a very different distribution (Fig. 26, white bars). We perform a simple calculation, which

supports our qualitative understanding of this result. We consider interference of two fields (of the same frequency), whose intensities (I_1 and I_2) fluctuate within 10% of their mean values. We further assume that the relative phase of these two fields varies randomly between 0 and 2π (every value of $\triangle\phi$ being equally probable). The resultant intensity $I = I_1 + I_2 + 2\sqrt{I_1 I_2}[\cos(\triangle\phi)]$ is expected to produce a histogram that is inversely proportional to the derivative of I with respect to $\triangle\phi$ and therefore has two peaks (at $I_1+I_2+2\sqrt{I_1 I_2}$ and $I_1+I_2-2\sqrt{I_1 I_2}$, where $\triangle\phi$ equals 0 and π respectively). This is exactly what our simulation shows (Fig. 26, dotted curve). In this simulation, we take the average value of $< I_1 >$=0.41 (arbitrary units) from the measurement, and find (from the best fit in Fig. 26) $< I_2 >$=0.09. We repeat the calculation 91300 times (using random number generators), and divide the calculated number of counts (per intensity) by a factor of 100 when we compare the simulation with the experiment. The two peaks in the simulated histogram appear to be broadened by the fluctuations of I_1 and I_2, which are taken to be 10% each (matching the experimental observations). The peak on the right (at higher pulse energy) is calculated to be lower and broader than the peak on the left, in excellent qualitative agreement with the experimental data. This measurement, and its comparison with theory, confirms our expectation that the (highly-coherent) Raman process results in generation of mutually-coherent sidebands. We expect that if the phases of the input fields are stabilized, the spectral phases at the output will also be stable.

F. Conclusion

In conclusion, we observe efficient generation of what to our knowledge is a record-large number of spectra sidebands in Raman-active crystals driven by two-color fs pulses. We observe sideband generation with excitation of either the Raman mode at

903 cm^{-1} or 325 cm^{-1}. We find that phase matching plays a major role. The FWM process and the Raman process coexist. The frequency spacing of the generated sidebands is dependent on the angle and polarization of the beams. The generation is optimized when the polarization of the two beams are parallel and when the angle between them satisfies the phase matching condition.

More sidebands are generated when three beams are applied in a planar configuration when all three input beams lie in the same plane. When the three beams are sent in a Box CARS configuration, a 2-D color array is generated. Different phase matching conditions between the probe pulse and the the AS generated by the pump and Stokes pulses result in a very different 2-D generation.

Using a third probe pulse, we observe absorption of the probe beam when a UV probe is used. Also we measure the coherence decay time of the excited Raman modes with both fs and ps probe pulses.

The generation in $PbWO_4$ has low threshold and high converting efficiency. We have measured up to 31 percent of the pump energy being converted to the sidebands. The good temporal coherence implies that this broad-band light source may be used for synthesis of subfemtosecond light waveforms.

CHAPTER IV

BROADBAND COHERENT LIGHT GENERATION IN DIAMOND USING TWO OR THREE-COLOR FS LASER FIELDS

A. Introduction

In the last chapter, I describe the broadband generation in $PbWO_4$ using fs pulses. We also use another crystal diamond for the broadband generation. There are two main reasons. Firstly, diamond has a single strong narrow Raman line at a very large frequency shift (1332 cm^{-1}), compared to the other crystals [64]. Because the diamond sample exhibited one of the most intense Raman lines, the values of Raman scattering cross section for the other materials that they investigated were normalized to those of the diamond. They have shown, in this reference, that the integral Raman scattering cross section determines the Raman gain coefficient in the transient case [64]. Secondly, diamond is isotropic and the refractive index is well known, which makes it easier (compared to $PbWO_4$) to do some theoretical calculation and thus help us understand the complicated experimental results.

Beside the above-mentioned two reasons, diamond also has several remarkable properties which are desirable in our research [65]. First of all, diamond is capable of transmitting an unusually broad spectral range (from x-ray region to the microwave and mm wavelengths) and has the widest electromagnetic bandpass of any material. There is an absorption band below 230 nm and an infrared absorbtion which lies between 1400 and 2350 cm^{-1}. This broadband transmission is essential for the sideband generation. It also makes diamond a good candidate material for far IR generation. Secondly, it has an extremely high thermal conductivity (five times that of copper) and is extremely chemically inert. Therefore, it is not easy to get damaged by laser

and does not require much protection from moist. At last, diamond has the highest atom density of any material. A high density means a high Raman gain.

The well-known sharp Raman line, which corresponds to the energy of the triply degenerate F_{2g} vibrational mode of the two interpenetrating cubic sublattices of the diamond [66], is used in the Raman spectroscopy to determine the bonding states of the carbon atoms and to tell the diamond from the graphite-carbon-diamond aggregates. The strong covalent carbon-carbon tetrahedrally bonding and light mass of the carbon atoms result in a large frequency shift of the F_{2g} optical mode. Back in 1963, diamond was chosen as a representative covalent crystal for the SRS experiment and two S and 1 AS were observed when a high intensity (20 MW/cm^2) Ruby laser was used for excitation [67]. Later, the spectrum, gain, and angular distribution of intensity of stimulated Raman emission in diamond was studied in detail [68]. They found that the intensity of normal Stokes increased linearly with increasing laser intensity up to the threshold for SRS, followed by a sharp increase in intensity by a factor of 10^6 and eventually by saturation and damage to the crystal. Also the stimulated linewidth was observed to be an order of magnitude narrower than the normal linewidth. Natural diamond are costly and scarce. Recently, synthesis of large area diamonds at lower pressure using chemical vapor deposition (CVD) technique was developed. The quality of CVD diamond approaches that of the purest natural diamonds. The CVD diamond finds applications in laser physics such as heat spreaders for high power laser diodes, optical components for CO_2 lasers, UV detectors. Kaminskii *et al.* used CVD diamond for Raman laser converter based on SRS and reported observation of SRS (up to 1 S and 3 AS sidebands) in diamond (using both ns and ps pulses) [69; 66]. In this chapter we present the study of the Raman generation in diamond using a pair of fs pulses.

B. Broadband coherent light generation in diamond driven by two-color femtosecond laser field

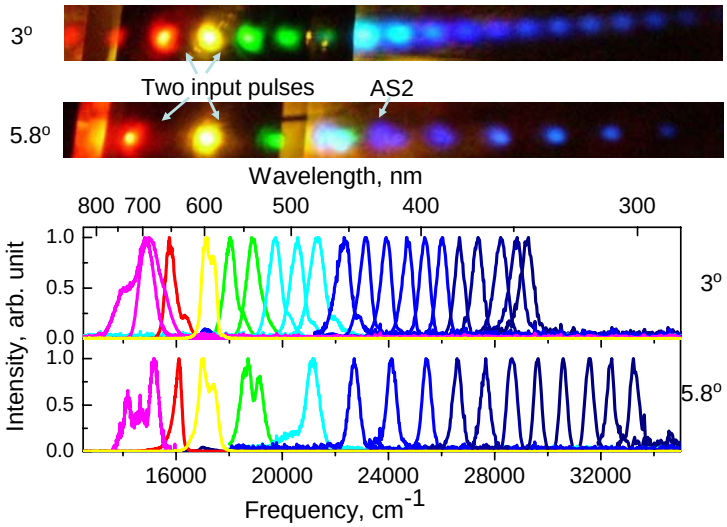

Fig. 27. The broadband generation in diamond with the two input beams (λ_1= 630 nm and λ_2= 584 nm, $\delta\nu$= 1250 cm^{-1}) crossing at angles of 3° and 5.8°. Top: The generated beams are projected onto a white screen. The two pump beams, S 1 and the first few AS beams are attenuated (after the sample) by a neutral-density filter. The AS 2 spot clearly shows two different colors, with blue corresponding to the Raman generation and green to the FWM signal. Bottom: Normalized spectra of the generated sidebands.

First we apply two-color excitation in the diamond. The experimental setup is about the same as the one we use for $PbWO_4$ crystal. By applying two 50 fs pulses (at λ_1= 630 nm, λ_2= 584 nm, and $\delta\nu$= 1250 cm^{-1}), we obtain a generation of up to 16 AS and 2 S sidebands in a 0.5 mm thick diamond sample. The highest frequency generated is in the UV region at a wavelength of 301 nm. Similar to the sideband generation in $PbWO_4$, the sideband doesn't have a equally spaced frequency shift. When we vary the crossing angle between the two applied laser beams (we used 3, 3.8, 4, 4.5 and 5.8°), and record the changes in the generated spectrum (Fig. 27, only

3 and 5.8° are shown for clarity), we find that the generation is more efficient at a 3° beam crossing angle. The energy conversion from the pump beam to AS 1 is 3%. It is 2% to the S1 and 0.5% to AS 2. The energy conversion from the pump beam to all the sidebands is 14%. The generated sidebands using 3° crossing angle overlap substantially in spectra with each other. Assuming that all the sidebands generated from 3° crossing in diamond are properly phased or locked to each other, we estimate that a single cycle of pulse with width of 0.5 fs can be obtained.

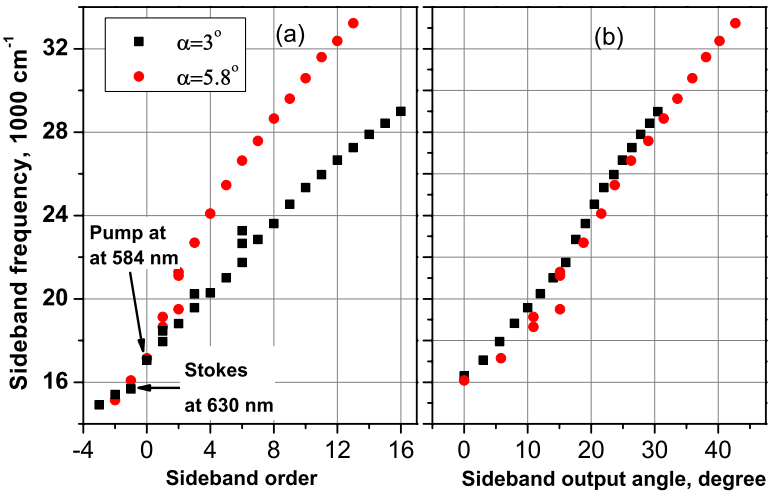

Fig. 28. The sideband frequency as a function of the sideband order (a) and as a function of the sideband output angle (b) with the two input beams (λ_1=630 nm and λ_2=584 nm, $\delta\nu$= 1250 cm^{-1}) crossing at two different angles, 3° (square) and 5.8° (round). The sidebands generated at 5.8° have a larger (about twice) frequency spacing compared to the 3° case.

From Fig. 27, we can clearly see that the instantaneous FWM signal coexists with Raman generation in the lower orders of the sidebands. The AS 2 beam spot shows two colors: blue and green. By measuring the frequency shift from the preceding sideband, we deduce that the blue is due to Raman generation, while the green beam

corresponds to the FWM signal.

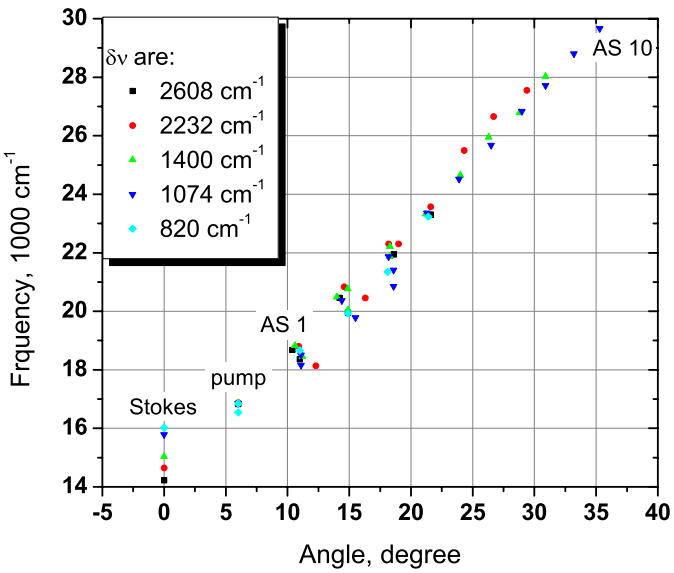

Fig. 29. The Sideband frequency and output angle at the different detunings ($\triangle\nu$ vary from 820 cm^{-1} to 2608 cm^{-1}) between the pump (fixed at 594 nm) and Stokes pulses. The output angles do not vary much, nor does the the frequencies of the sidebands, although $\triangle\nu$ varies a lot.

We plot the sideband frequency versus the sideband order as shown in Fig. 28 (a). It shows that sidebands generated at 5.8° have a larger (about twice) frequency spacing compared to the 3° case. Also the sidebands come out at a much larger angle spacing as shown in the Fig. 28 (b) (we define the Stokes output angle as 0 degree). This is more obvious for low-order sidebands which are more affected by the strong FWM signal. Both frequency and angular spacing decrease for the high-order sidebands. This shows that the initial phase matching condition between the two pump beams decides the generated sideband output angles and frequencies.

To prove that the sideband generation is from the Raman rather than the FWM process, we keep the pump frequency the same while tuning the Stokes frequency

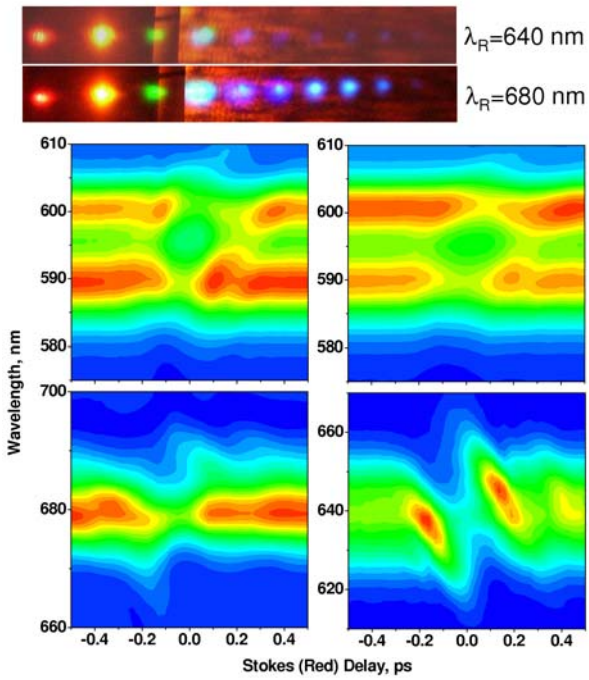

Fig. 30. The generation pictures and the pulse time responses in two different situations: (a) $\triangle\nu$ is tune close to resonance with the Raman transition and (b) the Stokes and the pump wavelengths are phase-matched at the chosen angle. When $\triangle\nu$ is on resonance with the Raman transition, the Stokes get amplified.

from 820 cm^{-1} to 2608 cm^{-1} and record the sideband frequency. The result is shown in Fig. 29. When $\triangle\nu$ varies from 820 cm^{-1} to 2608 cm^{-1}, the output angle doesn't vary much. Also, the frequency vary much less compared to the change of $\triangle\nu$. These facts are clear indications that the signals are generated mainly through the Raman process. The competing FWM process only affects the sideband slightly.

We always keep the laser intensity below the threshold for SPM. In diamond it is 3.35 mW for the (yellow) pump beam and 0.822 mW for the (red) Stokes beam, which are three to four times higher than the power used for $PbWO_4$ crystal. As a result, the effect of FWM on the sideband generation is more obvious compared to that of the $PbWO_4$. The generation is best in two situations. One is when $\triangle\nu$=1074

cm^{-1}, the frequency spacing is close to resonance with the Raman frequency. Now the phase matching condition is poorly satisfied. Consequently, low-order sidebands are relatively weaker. However, the high-order sidebands (from AS 6 to AS 9) are almost equally strong and only get weak from AS 11, as shown in Fig. 30. Another situation is when $\triangle\nu$=2232 cm^{-1}, the Stokes (at 680 nm) beam is in good phase matching condition with the pump (at 594 nm) beam with the angle we choose. The low-order sidebands are very strong because the boost from the FWM process. We conclude that for optimal sideband generation, we should choose a pair of pulses which are on resonance with the Raman transition and cross at an angle that satisfies the phase matching condition.

Another interesting feature is the interaction of the pump and Stokes pulses at the overlap (in time) region as shown in the bottom of Fig. 30. When $\triangle\nu$ is on resonance with the Raman transition (λ_{Stokes}=640 nm), the Stokes beam gets amplified through the SRS process. That is to say, the intensity of the Stokes beam increases when the pump field is present.

We see how the polarization of the pump and Stokes beams affects the sideband generation in diamond through a different experiment than the one used for $PbWO_4$. When we vary the polarization of the Stokes beam relative to the pump beam, the intensity of the sideband AS 1, AS 2 and AS 10 vary as shown in Fig. 31. The sidebands have maxima when the pump and Stokes beams have parallel polarization (waveplate angle at 0 or 180 degrees). No sidebands are generated when the polarization of the pump and Stokes beam are perpendicular to each other.

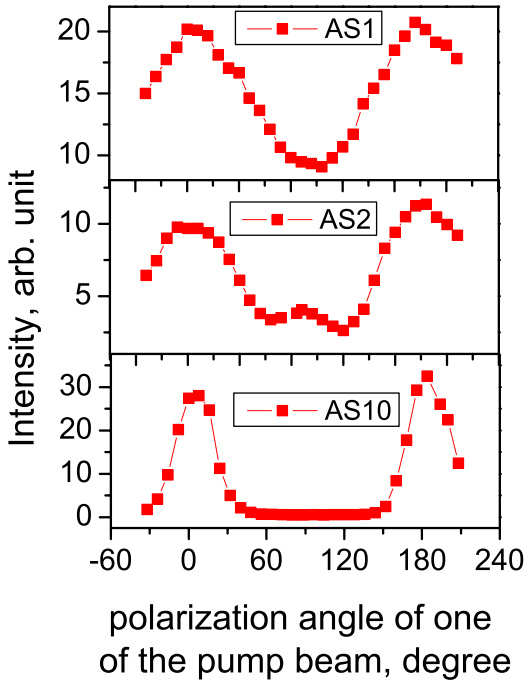

Fig. 31. The intensity of the sideband AS 1, AS 2 and AS 10 as a function of the polarization angle of the Stokes beam. The pump and the Stokes beams have parallel polarization at 0 and 180 degrees.

C. Phase matching calculation

Due to the material dispersion, phase matching is optimized when different frequency components propagate at different angles. To find out the optimal angle between a pair of wavelengths we first do a simulation using the peak wavelengths of the pulses.

The refractive index of diamond is given by a generalized Cauchy dispersion formula [70]:

$$n(\lambda) = 2.37 - 1.0 \times 10^{-5}/(1.24/\lambda)^2 + 8.0 \times 10^{-3} \times (1.24/\lambda)^2 + 1.0 \times 10^{-4} \times (1.24/\lambda)^4, \tag{4.1}$$

with λ in units of μm. This formula fits well with the available experimental data [71; 65]. (Other constants which are related to our research is the third-order nonlinear optical coefficient, which is 1.8×10^{-13} esu (2.0×10^{-22} m^2/V^2) and the nonlinear refractive index, which is 1.3×10^{-15} cm^2/W (it is one magnitude higher than that of fused silica) [46]).

The k vectors for the pump and Stokes fields are:

$$\begin{aligned} k_p &= \frac{2*\pi}{\lambda_p} * n(\lambda_p) \text{ or simply in cm}^{-1}, \\ k_p &= \frac{10^4}{\lambda_p} * n(\lambda_p), \\ k_S &= \frac{10^4}{\lambda_S} * n(\lambda_S). \end{aligned} \tag{4.2}$$

Here p denotes for the pump field and S denotes the Stokes field (by convention, $\omega_p - \omega_S = \omega_{Raman}$). From energy conservation, $\omega_{FWM} = 2 * \omega_p - \omega_s$, we have

$$\lambda_{FWM} = \frac{2*\pi*c}{\omega_{FWM}} = 1/(\frac{2}{\lambda_p} - \frac{1}{\lambda_s}), \tag{4.3}$$

$$k_{FWM} = \frac{10^4}{\lambda_{FWM}} * n(\lambda_{FWM}). \tag{4.4}$$

On the other hand, the optimal k vector can be calculated as :

$$K_{optimal} = \sqrt{(2k_p \cos\theta_p - k_s \cos\theta_s)^2 + (2k_p \sin\theta_p - k_s \sin\theta_s)^2}. \tag{4.5}$$

Note here the angle has to be converted to the angle inside the crystal by using the Snell's law.

We measure the wavelengthes (peak value) of the sidebands generated when the crossing angle between the pump and Stokes beams is 3 °. The results are shown in table I. We then use a phase matching factor M=sinc$^2(\delta k * L/2)$ to characterize the phase mismatch between the input fields or the generated fields. $\delta k = k_{FWM} -$

$K_{optimal}$, L is the sample thickness, which is about 500 μm in our experiment. When we use the measured wavelengths and angles, we find that the sidebands are almost perfectly phase matched (M is above 0.97 for the high-order sidebands).

Furthermore, we perform calculations that support our qualitative understanding of the role of phase matching using a pulse instead of just the peak wavelength. We take the spectral intensity of an n's AS sideband as given by

$$I_n(\nu) \sim I_{n-1}(\nu - \nu_R) \cdot \mathrm{sinc}^2[\overrightarrow{k}(\nu) - \overrightarrow{k}(\nu - \nu_R) - \overrightarrow{k}_R]L/2. \tag{4.6}$$

Here $\overrightarrow{k}$ is the wavevector ($k = n\nu/c$), ν_R is the Raman shift and c is the speed of light. The k-vector of the Raman excitation $\overrightarrow{k}_R$ is determined by the directions of the two input beams. We assume that the angle between the low-order sidebands is approximately the same. From a simple phase-matching calculation as shown above, the optimal generation of the lower-order AS sidebands is expected when the input beams are crossed at a 3.6° angle.

We find that when the angle is smaller than the phase matching angle, the peak frequency shift of the generated AS 1 from the pump pulse is 1163 cm^{-1}, which is smaller than the Raman shift and the opposite happens when an angle larger than

Table I. The wavelengths and the angles of the generated sidebands.

	Stokes	Pump	AS1	AS2	AS3	AS4	AS5	AS6	AS7
λ (nm)	613.5	586	557.3	531.3	511.0	494.0	476.1	460.0	437.5
θ (°)	0	3.00	5.6	7.9	10.0	12.0	14.0	16.0	17.6
	AS8	AS9	AS10	AS11	AS12	AS13	AS14	AS15	AS16
λ (nm)	423.5	407.48	394.7	385.1	375.1	366.9	358.6	351.8	345.0
θ (°)	19.1	20.5	22.0	23.6	24.9	26.4	27.8	29.2	30.5

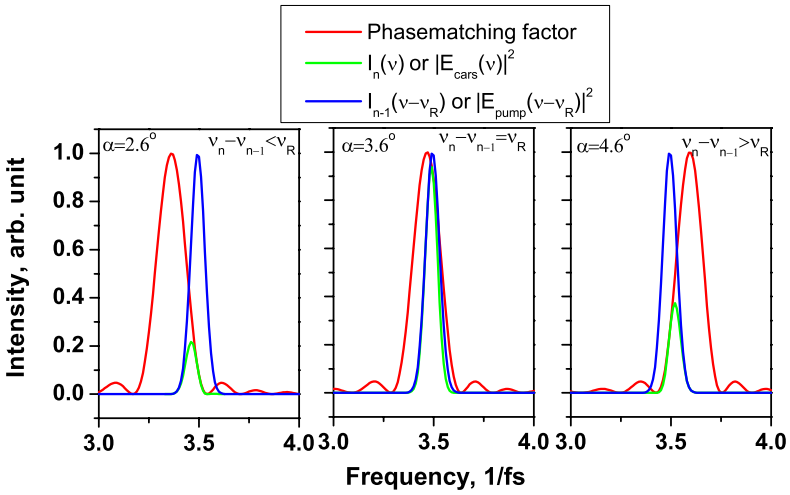

Fig. 32. Theoretical calculation of the frequency of AS 1 when the two pump beams (λ_S=630 nm, λ_p=581.23 nm, $\delta\nu$=1332 cm^{-1}, exactly the Raman frequency) cross at an angle of 2.6, 3.6 and 4.6 degrees, respectively. The phase matching angle between the two input beams is 3.6 degrees. The sample thickness is 500 μm.

the phase matching angle is applied as shown in Fig. 32. The peak frequency shift of the generated AS 1 from the pump pulse is 1301 cm^{-1} for a input angle of 3.6 degrees and 1466 cm^{-1} for 4.6 degrees. This agrees with our experimental observations on diamond. The peak wavelengths of the two input pulses phase-matches at 3.6 degrees. Therefore, when the two input pulses cross at 5.8 degrees, the generated spectrum has a larger frequency spacing than that of the 3 degrees. This calculation may also explain the gradually decreasing frequency spacing between the sidebands, since the optimum beam-crossing angle increases with a increasing sideband frequency because of the normal medium dispersion.

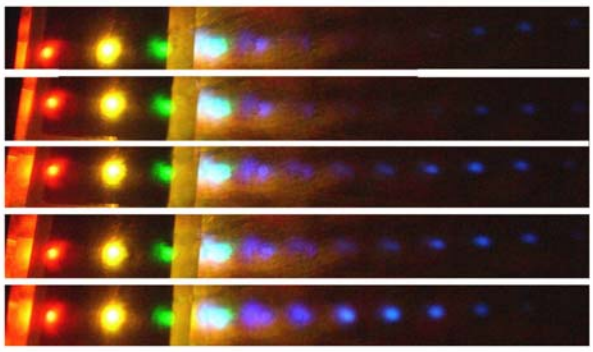

Fig. 33. The sideband generation in diamond at the different delays between the two pump pulses (λ_1= 630 nm and λ_2= 584 nm, $\delta\nu$= 1250 cm^{-1}). The time delay between each picture is about 20 fs. We see at certain delays, the high-order sidebands are brighter than the lower ones.

Raman generation in crystal is a complicated process. For example, we observe that the sideband intensity varies as we vary the delay between the two pulses. We have observed that high-order sidebands have higher intensity than the lower order ones as shown in Fig. 33, counter-intuitively. We guess that this is due to the phase-matching condition for the sidebands since the intensity of the radiation generated

by FWM is given by [72]:

$$I = \frac{9\omega_s^2}{16c^4\varepsilon_0^2 n_s n_S n_p^2}|\chi^3_{FWM}|^2 l^2 I_i I_p^2 \mathrm{sinc}^2(\triangle kl/2). \tag{4.7}$$

Here ω_s is the signal frequency, n_s, n_S, n_p are the refractive indices for the signal, Stokes and pump beams, respectively. The phase-matching factor $\mathrm{sinc}^2(\triangle kl/2)$ may modulate the sideband intensity.

D. Coherence between the sidebands

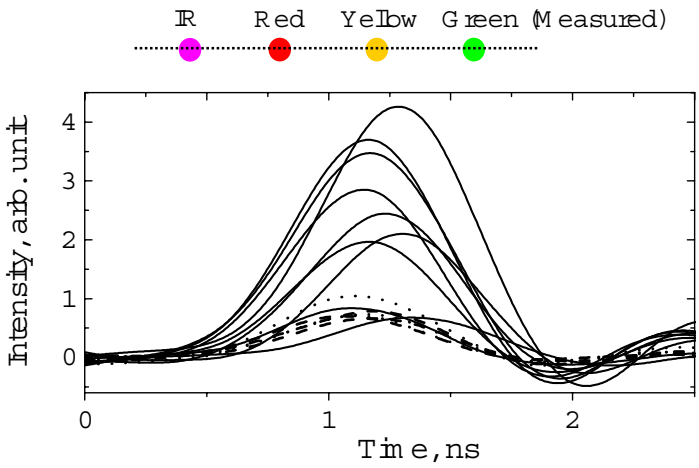

Fig. 34. "Green" sideband energy under different conditions. Black solid line: all three input pulses are present. Red dotted line: IR and Red pulses present only. Green dashed line: Yellow and Red pulses present only. Top: the input beam geometry.

We test the mutual coherence among the generated sidebands through an interference measurement. We use three input beams (instead of two) and align them in one plane, such that the higher-order AS sidebands generated through different channels overlap in space. We first generate AS 2 (Green, λ_{Green}= 545 nm) by focusing Red (λ_R= 690 nm) and IR (λ_{IR}= 802 nm) pulses into the diamond crystal. Then

we send a third beam in the direction of the generated AS 1 beam, as shown in Fig. 34(top). We tune the frequency of this third applied field (Yellow, λ_{Yellow}= 590 nm) such that the AS 1 generated from Red and Yellow fields coincides (both in space and frequency) with the AS 2 generated by Red and IR pulses. $\nu_{Green} - \nu_{Yellow}$= 1400 cm^{-1}, which agrees well with the Raman shift of 1332 cm^{-1}. When only one pair of pulses (either one) is applied to the crystal, the energy of the combined field (measured with a photodiode) is about 1 unit. When all three pulses are applied, the measured energy varies from 0 to 4 units from shot to shot as shown in Fig. 34 (we show 9 random shots), as a result of coherent addition of the two generated pulses. Since we don't attempt to stabilize the phases of the three input fields, the interference of the generated "Green" pulses is partially constructive or destructive, at random. We conclude that the two pulses, generated through the two separated Raman processes, have good mutual coherence. This measurement confirms our expectation that the (highly-coherent) Raman process results in generation of mutually-coherent sidebands. Assuming that all the sidebands generated from 3° crossing in diamond are properly phased or locked to each other, we estimate that a single cycle of pulse with width of 0.5 fs can be obtained.

E. The measurement of the coherence decay time of the CARS/CSRS signals

The unequal frequency spacing between the generated sidebands raises the question of the purity of the diamond we use. Using a pair of visible pulse as the pump (584 nm) and Stokes (635 nm) while using a UV pulse (318 nm) as a probe pules, we observe the CARS signal at 305.8 nm ($\delta\nu$= 1250 cm^{-1}) and CSRS signal at 332 nm ($\delta\nu$= 1326 cm^{-1}) (Fig. 35). Undoubtedly, this is the strong Raman line in diamond. The width of the line in the SRS spectrum $\Delta\nu_R$ is about 2.5 cm^{-1}. Accordingly the phonon

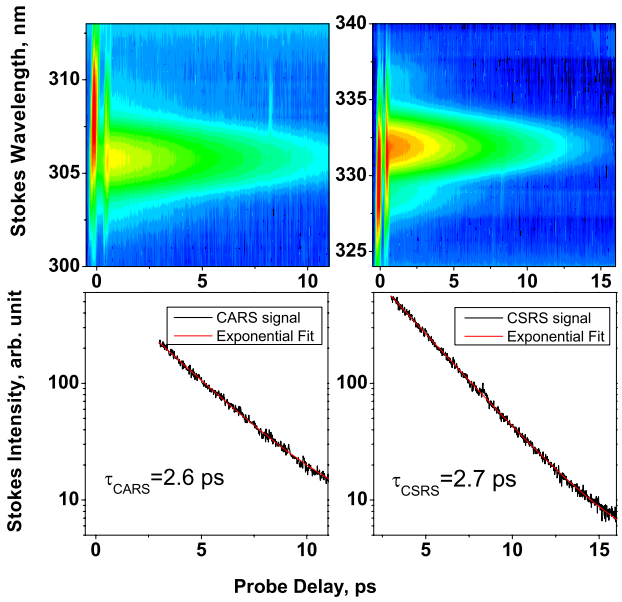

Fig. 35. The CARS and CSRS signals observed in diamond using a UV probe pulse. Top, the spectra of the CARS (left, center wavelength is 305 nm) and CSRS (right, center wavelength is 332 nm) as a function of the probe delay. Bottom, the exponential decay time of the CARS (left) and CSRS (right) signals.

relaxation time is $T_2 = (\pi c \Delta\nu_R)^{-1}$ ≈4.2 *ps* [69]. We measure the exponential decay of the the CARS/CSRS signals as shown in Fig. 35. Using $I_{CARS} \sim A\exp(-t/T_2)$, with A a constant, we obtain a decay time (T_2) of 2.6 ps for the CARS signal and 2.7 ps for the CSRS signal. This corresponds to a 4 cm^{-1} linewidth. The deviation could be due to the use of fs pulses. We also measure that AS 2 has a exponential decay with T_2=1.47 ps, which is half that of the AS 1. There is an obvious gap (about 1.5 ps) from the FWM signal to the CARS peak, which remains another mystery to us.

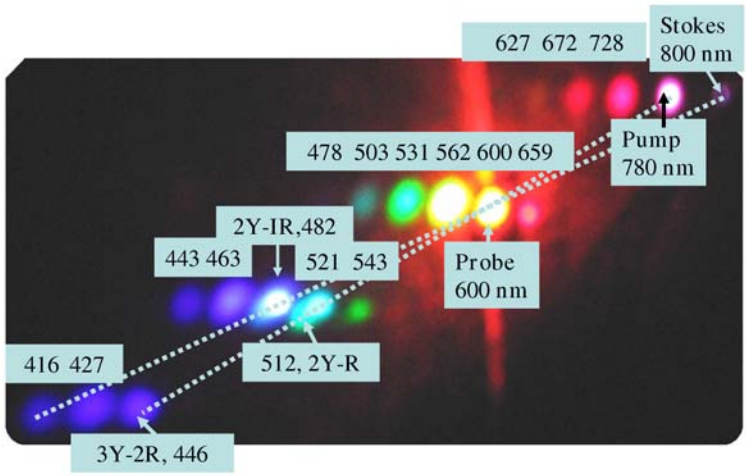

Fig. 36. The 2-D array generation in diamond with three input pulses (λ_{pump}= 720 nm, λ_{Stokes}= 800 nm, and λ_{probe}= 600 nm). The wavelengths of the sidebands are labelled in nm. The degenerate FWM signal (2Y-IR, a shorthand of $2\omega_Y - \omega_{IR}$) from the probe and Stokes pulses and the one (2Y-R) from the probe and pump pulses are much stronger than the Raman generation spots. They either superimpose or shift slightly. The six-wave-mixing signal (3Y-2R) from the pump and probe pulses is also visible.

F. Two dimensional color array generation in diamond driven by three-color femtosecond laser field

Similar to $PbWO_4$, when we apply a Stokes pulse (IR, 800 nm), a pump pulse (red, 728 nm) and a visible probe pulse (yellow, 600 nm) at the usual Box CARS geometry, in addition to the strong CARS and CSRS signals, we obtain a 2-D color array as shown in Fig. 36. Here the angle between the pump and Stokes beams is 5 degrees. The probe beam is 11 degree from the pump beam and 16 degrees from the Stokes beam. Due to a different dispersion from that of the $PbWO_4$, the generated 2-D color array is very different although same input angles between the beams are used. In addition, with a single Raman line, the result is easier to understand. The frequency spacing between the pump and Stokes pulses is around 1000 cm^{-1}. As a result, the

average sideband spacing is very regular, about 1040 cm^{-1}. The sidebands in the first row are generated by the pump and Stokes pulses. The second row is generated by the CARS/CSRS and the high-order CARS processes. The FWM signal from the probe and Stokes/pump pulses leads generation of the third row. The degenerate FWM signal from the probe and Stokes pulses ($2\omega_Y - \omega_{IR}$) and from the probe and pump ($2\omega_Y - \omega_R$) pulses are much stronger than the generation spots due to Raman effect. They either superimpose or shift slightly. The six-wave-mixing signal ($3\omega_Y - 2\omega_R$) from the pump and probe pulses results in the fourth row sideband generation. We measure the coherence decay time again so that we can compare it with that measured with a UV probe beam. The CARS signal (558.6 nm) has a frequency shift of 1235 cm^{-1} from the probe pulse and an exponential decay of 2.5 ps. The CSRS signal (652.2 nm) has a frequency shift of 1329 cm^{-1} and an exponential decay of 3.0 ps. These decay times are similar to the ones obtained with a UV probe pulse. Similar to the situation in which a UV probe pulse is used, the CARS frequency shift is somehow smaller than the CSRS frequency shift from the pump pulse. If we look at the phonon dispersion curve of diamond [73], there is a peak at 1040 cm^{-1}. This peak may explain the frequency shift of 1040 cm^{-1}.

G. Conclusion

We show that beside $PbWO_4$, broadband generation using diamond is also possible. Nonlinear frequency conversion in diamond is efficient. We have measured 7% energy conversion into the AS 1 and 1% into the AS 2 and S 1. The high-order CARS/CSRS and FWM/SWM signals are also observed in the crystal. From the theoretical calculation we find that when the angle between the pump and Stokes beams is smaller than the optimal phase matching angle, the frequency spacing between the sidebands

is smaller than the Raman shift and the opposite happens when the angle between the pump and Stokes beams is larger than the optimal phase matching angle. It may explain the frequency spacing decreases for the high-order sidebands as well. We also study the coherence decay of the Raman mode using the fs pulses. Similar to $PbWO_4$, we observe a 2-D color array generated when three-color fs laser beams are applied in the diamond in a Box CARS geometry. Due to a different dispersion, the 2-D color array is very different from the one generated in $PbWO_4$ under the same input beam conditions.

Compared to $PbWO_4$, we find that the onset of the SPM in diamond starts at a higher intensity of the laser pulse. Therefore a higher energy pulse can be used. However, the threshold for the Raman generation is higher too. The beams are more affected by the FWM process so that multiple peaks often show up in the low-order sidebands. As a result, the sideband spectrum is not as clean as that of the sideband generated in $PbWO_4$.

We believe that the generation can be optimized by choosing a pair of beams with proper wavelengths and using a lens with an optimal focal lens so that the beams cross at the crystal with a phase matching angle. Also smaller dispersion means that the generated sidebands can be increased both in number and energy by using a thicker sample (say, 1 mm), since more Raman gain can be obtained.

CHAPTER V

BROADBAND GENERATION IN RAMAN CRYSTAL DRIVEN BY A PAIR OF TIME-DELAYED LINEARLY CHIRPED PULSES

A. Introduction

In chapter III I present the results of sideband generation in the $PbWO_4$ crystal by focusing two near transform limited 50 fs laser pulses to the sample [74]. However, limited by the SPM and other nonlinear parasitic processes, at most 2 to 3 mW power can be used before the pulses get distorted. In this chapter, we study experimentally the broadband generation in the $PbWO_4$ crystal driven by a pair of time-delayed linearly chirped pulses (pulse duration ranges from 100 fs to 2 ps).

A pulse is called linearly chirped when its phase has a quadratic variation, i.e., the instantaneous frequency varies linearly with time delay. The frequency of a negatively chirped pulse decreases as a function of time delay, while the frequency of a positively chirped pulse increases vs. time. A transform limited fs pulse excites all the Raman-active modes accessible by the pulse width, as have been shown in the chapter III. For a pair of linearly chirped pulses, the difference between the instantaneous frequencies depends only on the time delay. When the frequency difference equals to a Raman frequency, this mode can be selectively excited [35]. In the time domain, a periodic pulse train is created, with a period equals to the period of a single Raman vibrational mode, as will be shown later in the theory section. A simplified setup for high-resolution spectroscopy has been built using a pair of time-shifted, linearly chirped pulses [75]. A related method of achieving the spectral selectivity is Fourier domain pulse shaping, when a pulse train is created by applying a periodic spectral phase to a single fs pulse using a pulse shaper [76].

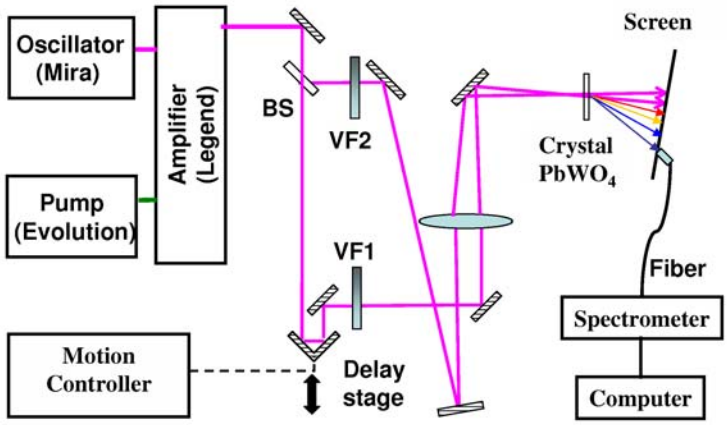

Fig. 37. Schematic of the experimental setup. VF: Variable neutral density filter; BS: 50/50 ultrafast beam splitter. An approximately linearly chirped pulse is obtained by misalignment of the compressor in the amplifier. It is split into two and later recombined at the sample with a relative time delay.

We present and discuss the different sideband generations obtained through the different Raman mode excitations by varying the time delay and the crossing angle between the two pump beams. The sideband generation by the excitation of Raman line at 325 cm $^{-1}$ is compared to that of using two-color near transform limited fs pulses with a central frequency separation close to the Raman frequency.

B. Experimental setup

The experimental setup is shown in Fig. 37. Briefly, the output of the regenerative amplifier (Legend, Coherent) is an infrared beam (λ=802 nm) of 35 to 50 fs pulses with a 1 kHz repetition rate and 1 W average power. It is split into two by an ultrafast beamsplitter. The delay between the two pulses can be varied by moving (with an electronic motion controller) a retro reflector which is mounted on a delay stage. The two beams are recombined and focused in the crystal by a 2 inch focal lens (f=50 cm). Both beams are attenuated by two variable neutral density filters so that the

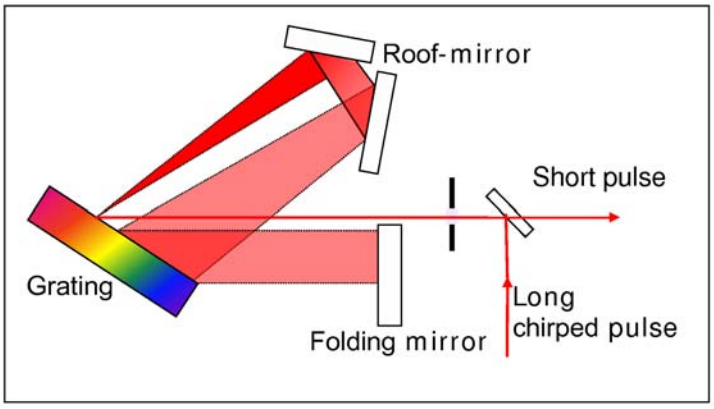

Fig. 38. Schematic of a compact compressor. Adapted from the laser training material, Coherent.

power used is below the threshold of the onset of the parasitic nonlinear processes. The power used ranges from 5 mW to 20 mW, depending on the pulse chirp rate and the focusing condition.

A schematic drawing of a compact compressor with a folded geometry is shown in Fig. 38. Normally two gratings are needed. Here the roof-mirror reflects the beam back to the same grating (different part) so only one grating is used. A long pulse with a time chirp is compressed after the compressor to a short pulse with no chirp. The roof-mirror is mounted on a translation stage that can be adjusted using a controller. Moving of the roof-mirror results in the changing of the effective distance between the gratings, therefore the changing of the chirp of the output pulse, as is shown in the theory part. The zero delay between the two pump pulses can be found by focusing the two beams (unchirped pulses) at a very small (less than 2 degrees) crossing angle in a piece of glass. When the two beams overlap both in space and time, an interference pattern around the two pump beams can be easily seen by the eye when they are projected to a paper screen after the crystal. Several orders of self diffraction (SD) of the beam can be seen when enough power is applied. The SD

signals show up symmetrically beside the two pump beams, similar to the picture as shown in Fig. 39 (c) (figure on page 82). The first order SD signal by the pump beam with a variable delay is what we used to measure the chirp introduced, as shown in Fig. 39 (b) (figure on page 82). We can see that the pulse we used is negatively chirped, with a pulse duration (FWHM) ranging from 80 fs to 2 ps. The chirp is approximately linear. The narrowing of the spectrum on the top (longer wavelength) might be due to the measuring range of the fiber-coupled spectrometer, which cuts off at wavelength 870 nm. The SD signals in crystal are much stronger compared to that in glass.

C. Theory

In this section I show how to estimate the chirp introduced to a pulse by changing the effective distance between the two gratings, and how to use the relationship between the time delay and the pulse chirp to identify which Raman mode is excited. I also show how a periodic pulse train resonantly excites the molecular vibrations, which lead to the sideband generation in the crystal.

1. Chirped pulse characterization

The temporally chirped pulse width introduced by moving the distance l between the gratings is [77]:

$$\delta_\lambda \tau = \frac{l(\lambda/d)\delta\lambda}{cd[1-(\lambda/d-\sin\gamma)^2]}. \tag{5.1}$$

where $\delta_\lambda\tau$ is the variation of group delay, l is the slant distance between the gratings, d is the grating constant, $\delta\lambda$ is the bandwidth of the pulse, c is the speed of light, and γ is the angle of incidence. In our experiment, λ=802 nm, $\delta\lambda$=35 nm, d^{-1}=1500 lines/mm, and γ is about 30°. When plug in these numbers we get: $\delta_\lambda\tau$= 4.2 l ps/cm.

In terms of frequency ω (=$2\pi c/\lambda$), the group delay can be expressed as:

$$\delta_\omega \tau = \frac{-4\pi^2 cl\delta\omega}{\omega^3 d^2[1-(\lambda/d-\sin\gamma)2]}. \tag{5.2}$$

Thus the linear relation between the delay and the frequency can be expressed as [77]:

$$\tau = \tau_0 - \frac{\omega-\omega_0}{\mu} + O(\omega-\omega_0)^2. \tag{5.3}$$

Here $\mu^{-1} = \frac{-4\pi^2 cl}{\omega^3 d^2[1-(\lambda/d-\sin\gamma)^2]}$, which is proportional to l. Therefore $\Delta\tau = t_d = \Delta\omega/\mu$. For a fixed $\Delta\omega$=ω_R, t_d is proportional to l, so the slope of t_d vs. the chirp rate is proportional to the Raman frequency ω_R.

The sideband generation in crystal is strongly influenced by the phase matching and thus the sidebands have a non-equal frequency spacing (decreasing for high-order sidebands). This relationship between the t_d and ω_R can be used to identify which Raman mode is excited. For example, one possible Raman mode which can be confused with the Raman mode at 903 cm^{-1} is one at 762 cm^{-1}. The intensity of this line is around 50 times lower than that of 903 line. However, the pulse intensity at 762 cm^{-1} width is 3 times higher. Raman generation is a highly non-linear effect so it is possible that 762 cm^{-1} can dominate. We measure t_d using different chirp rate pulses with the crossing angle between the two pump beams varying a few degrees. With a small angle crossing, only the 325 cm^{-1} Raman is excited so we can use the slope of the t_d vs. the different chirp rates as a reference slope. We measure a slope of 0.01 for a small angle crossing between the two pump beams and 0.028 for a relatively larger angle (4 degrees). Therefore we get $\omega_{R2}/\omega_{R1} = 2.8$, which is exactly the ratio between the 903 cm^{-1} and 325 cm^{-1}. So we identify that the strong Raman mode 903 cm^{-1} is excited at a large angle, not the one at 762 cm^{-1}.

We change the chirp gradually by a controller. Using the SD-FROG method

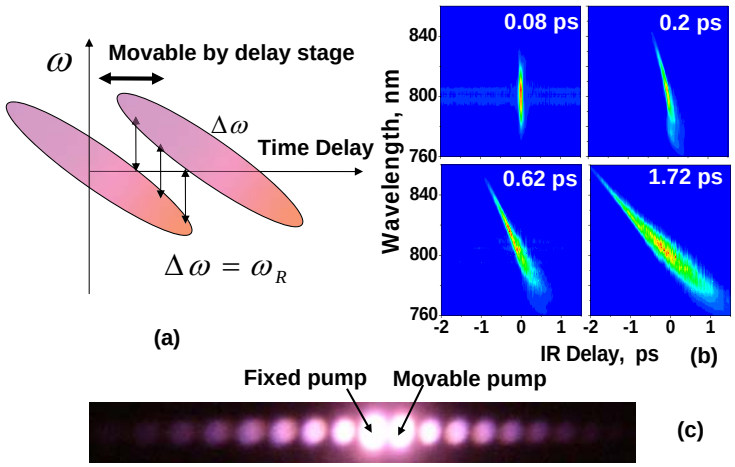

Fig. 39. (a) The schematics of the pulses for the Raman excitation; (b) The chirp of the pulses measured with SD-FROG; (c) Multiple orders of the self diffraction signals in the crystal.

and assuming a linear chirp, we measure a chirp rate of 1281 cm^{-1}/ps, 620 cm^{-1}/ps, and 319 cm^{-1}/ps respectively (Fig. 39 (b)). We then calculate the chirp rate b from b=$\omega_R/(2t_d)$ by measuring the t_d using pulses with different chirp rate when the Raman mode at 325 cm^{-1} is excited. We find these chirp rate agree well with our direct measurements using the SD-FROG method, which justifies our assumption of linear chirp.

2. Coherence preparation

A linearly chirped pulse can be written as:

$$E(t) = \exp(-at^2) * \exp[I * (bt^2 + \omega_l t)]. \tag{5.4}$$

Here $1/\sqrt{a}$ is roughly the pulse duration, b is the chirp rate of the pulse, and ω_l is the laser frequency.

The intensity for two time-delayed linearly chirped pulses is:

$$\begin{aligned} I(t) &= |E(t) + E(t - t_d)|^2 \\ &= \exp(-2at^2) + \exp[-2a(t - t_d)^2] \\ &+ 2\exp[-a(t^2 + (t - t_d)^2]\cos[b(2t - t_d)t_d + \omega_l t_d]. \end{aligned} \tag{5.5}$$

When $\Delta\omega$=ω_R=2bt_d, the last term in I_t is proportional to $\cos(\omega_R t+C)$ ($C = (2\omega_l\omega_R - \omega_R^2)/4b$, is a constant). We see that there is a periodic beat in the pulse intensity in the time domain. The periodicity of this pulse train can be matched to the period of this Raman mode at ω_R, permitting selective mode excitation [75]. One can adjust the excitation frequency simply by adjusting the time delay between the two pulses.

Molecular vibrations resonantly excited by a periodic sequence of short pulses has been described in detail by Gershgoren *et al.* [75] and Zheltikov [35]. The impulsively stimulated Raman scattering can be described by a driven damped harmonic oscillator [35]:

$$\frac{d^2Q}{dt^2} + 2\Gamma\frac{dQ}{dt} + \Omega^2 Q = F(t), \tag{5.6}$$

where Ω is the Raman frequency and Γ is the relevant damping rate, and F(t) is the external force applied. When a pulse train is used, the amplitude of the molecular vibrations is [35]:

$$Q(t) = \frac{C}{\Omega}\frac{\sin\frac{\pi NT}{T_0}}{\sin\frac{\pi T}{T_0}}\sin(\Omega t + \varphi), \varphi = \pi\frac{T}{T_0}(N - 1), \tag{5.7}$$

here $T_0 = 2\pi/\Omega$, N is the total number of pulses in the pulse sequence, C is a constant. We can see that when T is a multiple integer of the period of the molecular vibrations T_0, the amplitude of the molecular vibrations has a maximum. As a result of the coherently excited molecular vibrations, many sidebands can be generated, as

described in chapter II.

D. Experimental results and discussion

We have shown in the earlier chapters that the angle between the two pump beams is very critical for generation in Raman crystals. For example, to effectively excite the 903 cm^{-1} Raman mode, an angle of 3 to 4° is needed. While for the lower frequency Raman mode at 325 cm^{-1} to be excited, a smaller angle 2.5° works the best. We vary the the angle by adding a 20 cm negative lens after the 50 cm lens with a proper distance. Next we discuss the sideband generation at the different crossing angles between the two pump beams. For convenience of description, I call the pump beam which delay can be varied as the movable pump and the other one as the fixed pump beam.

1. Self diffraction and the excitation of the Raman mode at 191 cm^{-1}

When the angle between the two pumps is around 1°, self diffraction of the beam is observed at 0 delay as shown in Fig. 39 (c). Here we use collimated beams which have a beam size of about 1 mm.

When we apply a pair of linearly chirped pulses with a chirp rate of 2100 cm^{-1}/ps to the crystal, we observe up to 40 AS and 5 S sidebands generated as shown in Fig. 40 (a). The angle between the two beams is about 1.2°. We first observe AS generation on the movable pump side at delay t_d (here the movable pump acts as the pump beam and the fixed pump as the Stokes beam, as conventionally $\omega_p > \omega_s$.). When we move the pulse forward from 0 delay to -t_d, we observe generation on the fixed delay side. Now the fixed pump functions as a pump beam. Here only the picture in one side is shown since the generation pictures in both sides are symmetric. Due to the

loose focus of the beam, both the pump and the Stokes power is higher than 5 mW when measured after the crystal. The conversion efficiency from the pump beam to the sidebands is 25 %. The conversion efficiency of Stokes beam is about the same.

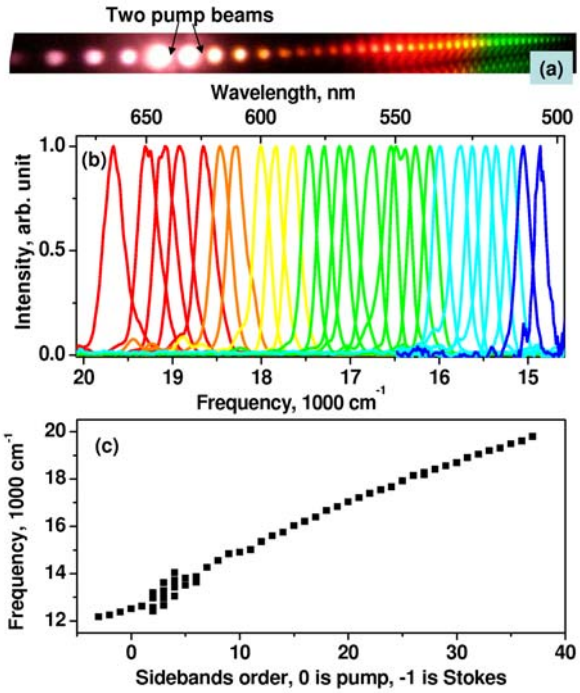

Fig. 40. Broadband generation in a $PbWO_4$ crystal using two time-delayed linearly chirped pulses applied at an angle of 1.2 ° to each other. The chirp rate of the pulse is about 2100 cm^{-1}/ps. (a) Generated beams projected onto a white screen. (b) Normalized spectra of the generated sidebands from AS 11 to AS 37. The wavelength is in reciprocal scale. (c) The peak frequency of the generated sideband plotted as a function of the sideband order. Multiple value corresponds to the multiple peaks in the sideband spectrum. The high-order sidebands have a slope of 200 cm^{-1} per AS order.

The spectra of the high-order sidebands (AS 11 to AS 37) are shown in Fig. 40 (b). There is substantial overlap between the spectra of the generated sidebands. When the angle is smaller and therefore a lower frequency Raman transition is excited, we observe continuum generation instead of the distinctive spots for the high-order

sidebands, due to the small angle separation and the wide spectrum of the sideband, similar to the picture shown in Fig. 41 (a). In Fig. 40 (c) we plot all the sideband peak frequency as a function of the sideband order. Here the multiple values means multiple peaks in spectrum. The average frequency spacing of the sidebands is around 200 cm^{-1}. We believe the generation at this angle is due to the excitation of Raman line at 191 cm^{-1}. The slight bending of the slope indicting a decrease in the frequency spacing.

2. The excitation of the Raman mode at 325 cm^{-1}

When two color excitation is used and the angle between the two pumps is small, we observe generation due to 320 cm^{-1} Raman mode excitation. About 30 AS is observed as shown in Fig. 41 (a). Only 2 to 3 mW power can be used, limited by the onset of the SPM. This mode should be easily accessed by the chirped pulse since the width (FWHM) of the pulse is around 460 cm^{-1}. To observe this, we use one 2 inch lens with focal length of 50 cm. The angle between the pumps is about 2.4 °. As many as 40 AS have been observed at two different delays. The output angle of the highest sideband with respect to the pump is about 50 °. Counterintuitively, like in diamond, we again observe that some of the high-order sideband is stronger than the low-order ones, as shown in Fig. 41 (d). This can be seen more clearly when a large angle between the two pump beams is used. There are two possible explanations. One is that the FWM coexist with the Raman process. When a certain order of the two processes is overlapped, that signal gets enhanced. A proof is that the sideband generation pattern changes when we vary the delay, since FWM signal varies as the delay changes. The other explanation is that the phase matching factor somehow modulates the intensity of the output sidebands, as described the last chapter. Further theoretical investigation is needed to solve this “mystery”.

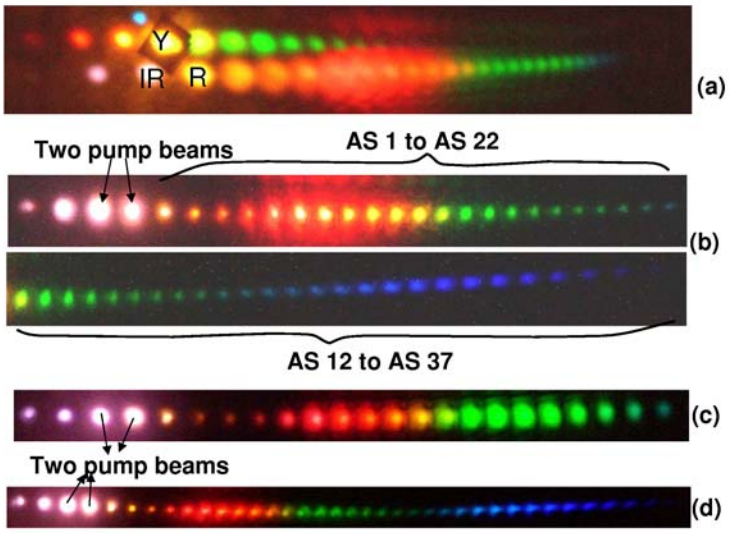

Fig. 41. (a) Broadband generation in $PbWO_4$ crystal pumped by fs pulses (λ_S=804 nm, λ_S=766 nm, and $\triangle\nu$= 617 cm^{-1}). The angle between the pump and Stokes beam is 2.9 °. A third probe pulse (Y) leads to generation of many orders of CARS and CSRS signals. (b) Broadband generation in a $PbWO_4$ crystal using two time-delayed linearly chirped pulses applied at an angle of 2.4 ° to each other. The chirp of the pulse is about 2100 cm^{-1}/ps. (c) The generated beams by using a pair of linearly chirped pulses with a large chirp rate, 440 cm^{-1}/ps. d) The intensity modulation of the generated sidebands.

The generation at a chirp rate of 2100 cm^{-1}/ps is shown in Fig. 41 (b). We observe 40 AS and 3 S sidebands. The spacing between the sidebands is around 320 cm^{-1} in average. It decreases to 240 cm^{-1} for the high-order sidebands. As high as 41 % conversion efficiency has been measured for the pump beam and 21 % for the Stokes beam. When the chirp rate is increased to 1060 cm^{-1}/ps, the sideband generation seems less effective. The AS number decreases to 34. The pump beam has a 33 % conversion efficiency and the Stokes bean 19 %. When we introduce more chirp until a chirp rate of 440 cm^{-1}/ps is reached, the efficiency reduces to about 14 % for the pump beam and 11 % for the Stokes beam. About 22 AS is observed.

However, the absolute input power can be increased to 15 mW without introducing the nonlinear parasitic effects. Another feature of the generation using pulses with a high chirp rate is that the FWM signal gets weaker. Consequently, the generated sidebands have good beam profiles and the spectrum is mostly single peaked, as shown in Fig. 41 (c).

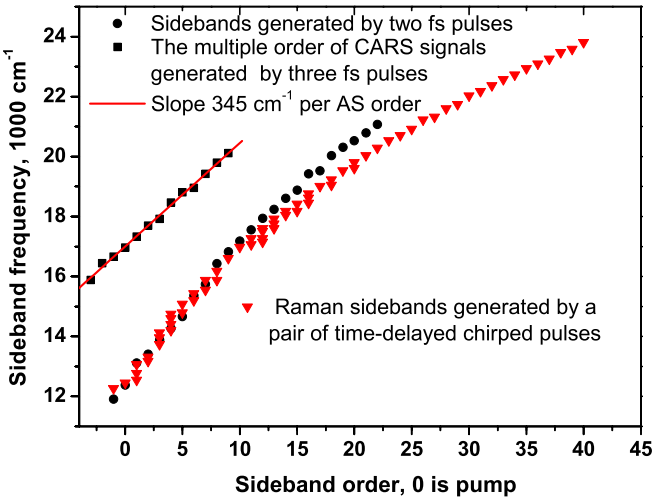

Fig. 42. Comparison of the sideband generation in PbWO4 crystal using two near transform limited fs pulses ($\delta\nu$=615 cm^{-1}) and a pair of time-delayed chirped pulses. Many more sidebands are generated in the latter case.

In Fig. 42 we plot the sideband frequency as a function of the sideband order. The square ones are the CARS/CSRS signals generated by all three beams when fs pulses are used (Fig. 41 (a), top row). The probe beam (Yellow) is labelled as 0 order. The frequency spacing is regular, about 345 cm^{-1} per AS order. Compared to the sidebands generated by two fs pulses (Fig. 42, round dots), there are many more sidebands generated when a pair of time delayed linearly chirped pulses are used (Fig. 42, triangles). The AS sidebands covering a range of 12,000 cm^{-1} span.

3. The excitation of the Raman mode at 903 cm^{-1}

The Raman mode 903 cm^{-1} frequency is the strongest Raman mode in the PbWO4 crystal. The FWHM of the pulse we used is around 400 to 500 cm^{-1}, depending on whether the iris is fully open or not. To find out this chirped pulse excitation can be used for this Raman mode, we change the angle between the two pumps to about 4°. We observe generation up to 15 AS as shown in Fig. 43.

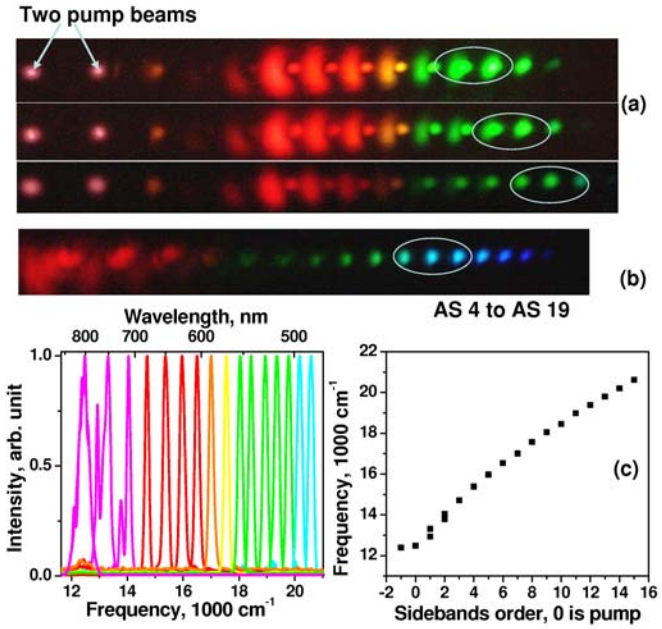

Fig. 43. Sideband generation in a $PbWO_4$ crystal using two time-delayed linearly chirped pulses applied at an angle of 4 ° to each other. The chirp of the pulse is about 620 cm^{-1}/ps. (a) Generated beams projected onto a white screen. Pictures are taken at three consecutive time delays between the two pump beams, with a increase of 33.3 fs. (b) The picture of the high-order sidebands. They are brighter than the low-order sidebands. (c) Normalized spectra of the two pump beam and the generated sidebands (left) and the peak sideband frequency plotted as a function of the sideband order (right). The slope is around 540 cm^{-1} per AS order.

With a large angle, the non-resonant FWM signal is more separated from the Raman generation as shown in Fig. 43 (a). We show the sideband generation picture at three consecutive time delays between the two pump beams, with a separation of 33.33 fs. As we can see, the large spot, which is due to FWM generation process, shifts as the delay varies. When certain order (circled by dots in Fig. 43 (a)) overlaps with the Raman generation (small round spot), the intensity of that order enhanced. When lower power or higher chirp rate pulses are used, the FWM process weakens and only sidebands generated through Raman processes appear. When high power or less chirped pulses are used, this FWM process sometimes leads to the distorted beam profile of the lower orders due to the competition between the two processes as shown in Fig. 43 (b). However, the high-order sidebands have good beam profiles. The spectra of the two pump beams and the generated sidebands are shown in Fig. 43 (c). The frequency spacing between the sidebands is decreasing from low-order to high-order sidebands, similar to the situation of sideband generation using two-color fs excitation. When we plot the peak frequency of the sideband as a function of the sideband order, we see a linear slope with a 540 cm^{-1} per AS order, which is much smaller than 903 cm^{-1}. The reason could be that this mode can only be excited by the edge of the chirped pulses.

E. Conclusion

We shape a fs pulse by introducing a linear chirp so that the pulse duration is close to the coherence life time in solids. The pulse is split into two and recombined on the crystal with a relative time delay. We adjust the time delay between the two pulses so that the difference of the instantaneous frequencies equals to a certain Raman frequency. As expected, this Raman mode is selectively excited and substantial

coherence builds up in the crystal. We measure up to 40 AS and 5 S sidebands generated. The conversion efficiency from the two pump beams to the sidebands is very high, for example, we have measured as high as 41 % conversion efficiency for the pump beam and 21 % of for the Stokes beam. By compare the sideband generation using the pulses with different chirps, we show that the nonlinear parasitic effect can be avoided by using a more chirped pulse. Thus laser pulses with more power can be used for the Raman excitation. However, if the peak intensity of the pulse is too low, the sideband generation is not very efficient either, as can be seen from the decrease in the conversion efficiency of the pump beams.

Compared to the two-color fs pulses excitation, this method has the advantage of more sideband generation (the AS sidebands covers a range of 12,000 cm^{-1} span), high conversion efficiency, high input power allowed (the power can be used without creating the parasitic nonlinear effect such as SPM can be 10 times higher than the transform limited pulse power used), and simpler setup. Although the FWM process still creates some multiple peaks structure in the spectra of the low-order sidebands, the complication due to simultaneous multiple Raman lines excitation when fs pulses are used is eliminated. Different Raman mode can be selectively excited by varying the time delay and the angle between the two pump beams.

This experiment confirm again that the phase matching condition plays an important role in the Raman generation process in crystal. When we vary time delay between the two pulses, no sideband generation related to Raman mode at 903 cm^{-1} is observed when the crossing angle between the two pump beams is small. On the other hand, at large angle, no sideband generation related to the Raman mode at 325 cm^{-1} is observed either.

The generation is more efficient for excitation of low frequency Raman mode at 325 cm^{-1} than that of high frequency mode at 903 cm^{-1}, which can be only excited

by the edge of the chirped pulses. We believe that if a two separately prepared time-delayed linearly chirped pulses which have a frequency difference of 903 cm^{-1} can be used, the sideband generation should be very efficient.

Since the generation is very sensitive to the time delay, this method can be used to measure the chirp when the Raman frequency is known or the other way around. This broadband generation can also be used for a continuum generation or a tunable light source. Most important of all, we have shown previously that the sidebands generated are mutually coherent [74]. Therefore it opens a possibility for this broadband light source to be used to synthesize subfemtosecond light waveforms.

CHAPTER VI

FEMTOSECOND COHERENT ANTI-STOKES RAMAN SCATTERING APPLIED TO THE DETECTION OF BACTERIAL ENDOSPORES*

A. Introduction

Dipicolinic acid (DPA) is a marker molecule for bacterial spores [43] and the ability to detect trace amounts of it is of paramount importance. We work with DPA in a H_2O/NaOH solution (NaDPA). Optical coherence of NaDPA has a relaxation time of the order of 30 fs, and vibrational coherence in liquids typically has a picosecond life time. Femtosecond pulses therefore are essential for the study of a complex organic molecule such as NaDPA. Impulsive pump-Stokes excitation (the pulse duration is shorter than the molecules vibrational beat cycle) of multiple modes of molecular vibrations results in quantum beats in the signal, which facilitates unambiguous detection of a target species and its discrimination against interferents [78]. These observable quantum beats, which allow extraction of species-specific parameters, occur on a subpicosecond time scale and therefore require femtosecond probing. For example, we have utilized fs CARS to study the vibrational dynamics of methanol-water solutions by measuring the beat frequencies between Raman modes and coherence decay rates of C-H stretch modes (at 2835 cm^{-1} and 2943 cm^{-1}) in methanol [63].

*Part of this chapter is reprinted from "Concentration dependence of femtosecond coherent anti-Stokes Raman scattering in the presence of strong absorption," by M. Zhi, D. Pestov, X. Wang, R. K. Murawski, Y. V. Rostovtsev, Z. E. Sariyanni, V. A. Sautenkov, N. G. Kalugin, and A. V. Sokolov, 2007, J. Opt. Soc. Am. B, 24, 1181-1186 (2007), copyright 2007, with kind permission from Optical Society of America.

B. Concentration dependence of femtosecond coherent anti-Stokes Raman scattering in the presence of strong absorption

Theory suggests that the CARS generation efficiency can be increased by using electronically resonant pulses. We have shown that when a UV probe pulse with a frequency near resonant to the first excited electronic state of the molecule is used, the efficiency per particle is 20-fold higher compared with a nonresonant probe pulse [79]. In such a near-resonant configuration, absorption is intrinsically present and limits signal generation at large concentrations. The propagation of ultrashort pulses through resonant media has previously been studied in both linear [80] and nonlinear regimes [81]. However, these previous results do not directly apply to the present work since our pulse spectrum is substantially narrower than the UV absorption band of DPA, which has a peak at 272 nm (see Ref. [82] or Figure on page 151).

In this section we present a detailed study of the concentration dependence of the CARS and CSRS signals. In particular, we have observed slopes having as large as the third power of concentration. We present a model that describes the propagation of the generated signal through the attenuating medium that agrees with our experimental results. We have derived an analytic expression for the signal intensity that includes a concentration-dependent dispersion. This generalized solution properly describes the observed deviations from the quadratic density dependence.

1. Experimental setup

The experimental setup is shown in Fig. 44. Briefly, the output of the regenerative amplifier (Legend, Coherent) is an infrared beam of 40-50 fs pulses with a 1 kHz repetition rate and 1 W average power. A small fraction is used as the Stokes beam (λ_{Stokes} = 806 nm). Approximately 60% of the infrared power is sent into optical

parametric amplifier (OPA) 1 (OPerA-VIS/UV, Coherent), which provides the pump pulses at $\lambda_{pump} = 726$ nm. The rest is used by OPA 2 (OPerA-SFG/UV, Coherent) to generate the probe beam ($\lambda_{probe} = 295$ nm). The pump and Stokes beams have a few milliwatts of average power on the sample. The UV probe power is ~0.5 mW. The sample is a NaDPA solution in a 100 μm quartz cell. After spatial separation, the generated beam is focused on the entrance slit of the monochromator (MicroHR, Jobin Yvon), which has a liquid-nitrogen-cooled CCD camera (Spec-10, Princeton Instruments) attached to the exit.

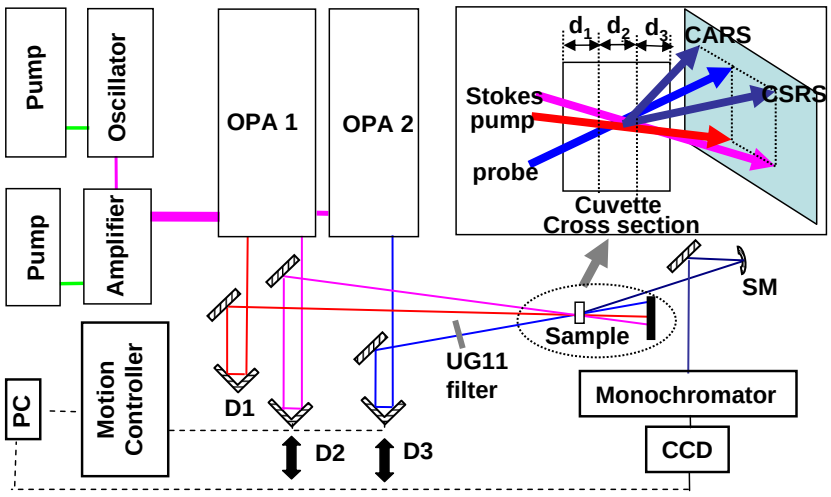

Fig. 44. Schematics of the experimental setup. OPA, optical parametric amplifier; D1, D2, D3, delay stages; SM, spherical mirror; UG11, UV bandpass filter; CCD: charge coupled device. Inset, CARS and CSRS generation in a folded boxCARS geometry.

We first describe experiments that used a similar setup (described in detail in Ref. [79]). In these experiments, instead of the CCD camera, we utilize a thermo-electrically cooled photomultiplier tube for signal acquisition. The sample is a quartz cuvette with a 2 mm path length filled with NaDPA solution. The pump, Stokes, and

probe wavelengths are 640, 585, and 320 nm, respectively. We choose off-resonance preparation for two major reasons: first, strong UV absorption would prevent us from homogeneous excitation of the coherence throughout the interaction volume; second, it allows one to avoid sample degradation due to extended UV exposure.

The folded boxCARS geometry, as shown in the inset of Fig. 44, is used for both of the setups. The angles are chosen such that the FWM phase-matching condition is satisfied for water. The pump and Stokes pulses are focused into a 100 to 300 μm spot size on the sample.

2. Experimental results and discussion

a. Experimental result with a 2 mm cuvette

To see the unambiguous signature of the DPA molecule, we pick up a frequency region where at least two Raman lines are within the spectral convolution of the preparation pulses (ω_{R1} = 1435 cm^{-1}, ω_{R2} = 1383 cm^{-1}) [79]. As a result, both of the Raman transitions can be excited. Due to quantum beating [40], we can see oscillations with expected beating frequency between the two vibrational bands.

DPA saturation in distilled water is reached at ~10 mM concentration at room temperature. By using NaOH as a buffer solution, higher concentrations of DPA solution can be obtained. Pipettes (Ergonomic Integra-lite) with 20 μl increment enable us to gradually change the concentration. The pulse energy around the peak of the first oscillation (which typically occurs between 0.4 and 0.5 ps probe delay) is recorded for CARS. It is normalized on the FWM peak for pure NaOH solution (no DPA, Fig. 45). The CSRS pulse energy has a similar dependence on the concentration of NaDPA. The concentration curves extracted from these measurements are shown in Fig. 46 for CARS (square symbols) and Fig. 47 for CSRS. The pulse energy in

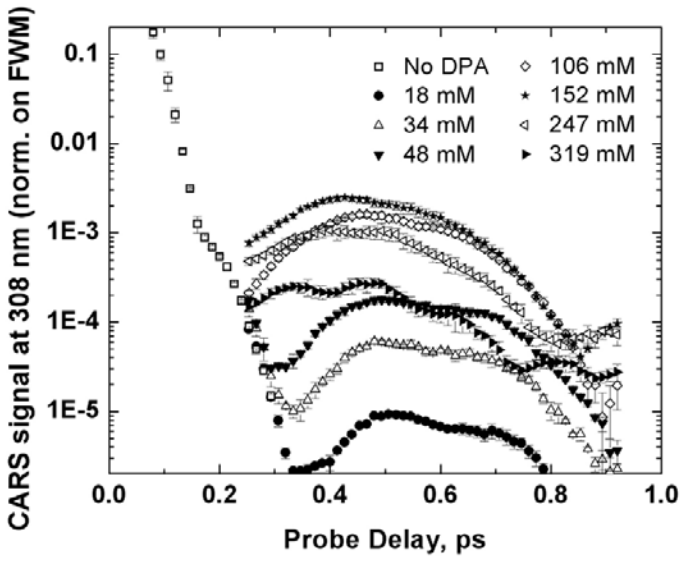

Fig. 45. CARS pulse energy as a function of probe pulse delay at different NaDPA concentrations. Sample, NaDPA solution in a quartz cuvette with 2 mm path. The pH value of the solution is about 14.

Fig. 46 is normalized on the maximal pulse energy recorded for CARS at 152 mM concentration (Fig. 45). Similar normalization is applied to CSRS pulse energy.

The concentration curves show similar features. The CARS pulse energy has a maximum at ∼152 mM and the CSRS peaks at 252 mM. This can be explained by the fact that the CARS signal has a relatively higher absorption cross section since the absorption peak of the NaDPA solution is near 272 nm (Appendix A). The theoretical curves obtained from our model, which will be discussed next, are shown together with the experimental data. The theoretical results are normalized in the same way as the experimental data.

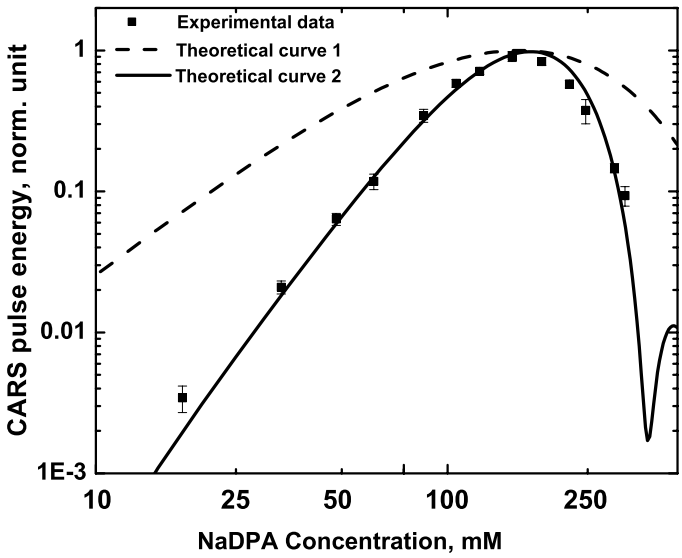

Fig. 46. Log-log plot of CARS pulse energy at the peak of the oscillation as a function of NaDPA concentration. The solid curve is the theoretical curve obtained with the phase-matching factor included; the dashed curve is the theoretical curve obtained with the assumption $\triangle k_s = 0$; at lower concentration, this curve has a slope of 2.

b. Theoretical model

Intuitively, the concentration dependence can be easily understood from the two limits. On one hand, when there is no DPA in the solution, there should be no signal, and adding DPA will result in the growth of the signal. The power law dependence of the signal on concentration in this limit is well known [79]. On the other hand, if there is too much DPA in the solution, both the signal and the probe pulse will get absorbed. As a result, the signal rolls over as the concentration increases after the peak value. A simple model that explicitly includes absorption for the probe and generated fields, but not for the driving fields, is developed to back up this intuitive consideration. Within our model, the field amplitudes are governed by the following

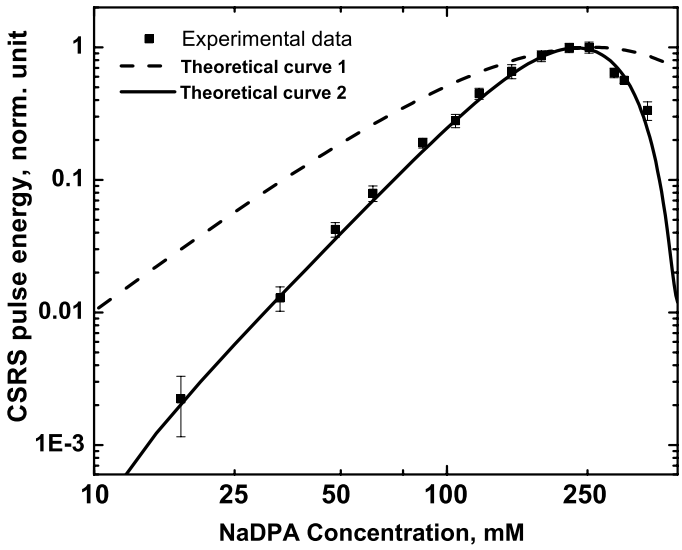

Fig. 47. Log-log plot of CSRS pulse energy at the peak of the oscillation as a function of NaDPA concentration. Solid line is the theoretical curve obtained with the phase matching factor included; dashed line is the theoretical curve obtained with the assumption $\triangle k_s = 0$; at lower concentration, this curve has a slope of 2, as is the case for CARS signal.

equations:

$$E_p(z) = E_p(0) \times e^{-\alpha_p z N/2}; \tag{6.1}$$

$$\frac{d}{dz}E_s(z) = -\frac{1}{2}N[\alpha_s E_s(z) - b\rho_{12}E_p(z)e^{i\triangle k_s z}]. \tag{6.2}$$

Here b is a coupling constant; N is the NaDPA molecule concentration; α_p and α_s are the absorption cross sections of probe and the generated signal pulse respectively; $\Delta k_s = k_s - [k_{probe} \pm (k_{pump} - k_{Stokes})]$ is the phase mismatch for CARS (plus sign) or CSRS (minus sign); k is the wave vector; and ρ_{12} is the coherence created by the two visible pump and Stokes pulses [79]. Note here that the parameter b has a resonant dependence on the frequency of the probe field. This gives us the resonance

enhancement of the signal. We consider three regions of the sample: before interaction (d_1), interaction region (d_2), and after interaction (d_3) (Fig. 44, inset). In our calculations d_1 is set to be equal to d_3 so that fewer parameters are used for fitting the experimental data. $E_p(z)$ is the probe-field amplitude, and $E_s(z)$ is the signal generated.

In our model, we use the following assumptions: (1) no absorption or depletion of the two visible pump and Stokes pulses, such that the coherence excitation is independent of concentration, and (2) linear absorption of the probe and signal pulses.

Substituting Eq. 6.1 into Eq. 6.2 we get

$$\frac{d}{dz}E_s(z) = -\frac{1}{2}N\alpha_s E_s(z) - b\rho_{12}E_p(0)e^{-\alpha_p zN/2}e^{i\triangle k_s z}. \tag{6.3}$$

E_s has the solution of the form

$$E_s(z) = Ce^{-\alpha_p zN/2}, \tag{6.4}$$

here C is a factor whose z dependence remains to be found. Next we integrate through the three regions. Substitute Eq. 6.4 into Eq. 6.3, we get

$$\frac{d}{dz}C = b\rho_{12}NE_p(0)e^{-\alpha_p d_1 N/2}e^{i\triangle k_s z}e^{-\alpha_p zN/2+\alpha_s zN/2}. \tag{6.5}$$

Here z=0 is at the boundary between d_1 and d_2, where the signal starts to generate.

Therefore

$$\begin{aligned} C &= \int_0^z b\rho_{12}NE_p(0)e^{-\alpha_p d_1 N/2}e^{i\triangle k_s z}e^{\alpha_s-\alpha_p zN/2} \\ &= b\rho_{12}NE_p(0)e^{-\alpha_p d_1 N/2}\frac{e^{(\alpha_s-\alpha_p)d_2 N/2}e^{i\triangle k_s d_2}-1}{(\alpha_s-\alpha_p)N/2+i\triangle k}. \end{aligned} \tag{6.6}$$

We obtain an analytic expression for $E_s(z)$ as

$$E_s(z) = b\rho_{12} N E_p(0) e^{-\alpha_p z N/2} \frac{e^{(\alpha_s-\alpha_p)d_2 N/2} e^{i\triangle k_s d_2} - 1}{(\alpha_s - \alpha_p)N/2 + i\triangle k} e^{-\alpha_s d_2 N/2} e^{-\alpha_s d_3 N/2}. \tag{6.7}$$

The relevant experimental quantity, however, is the signal (CARS or CSRS) intensity after the cell, $I_s^{\text{out}} = E_s^* E_s$, which is given explicitly as

$$\begin{aligned} I_s^{\text{out}} \quad &= |b\rho_{12}|^2 \cdot I_p^{\text{in}} \cdot \exp\left[-(\alpha_p d_1 + \alpha_s d_3)N\right] \cdot N^2 \cdot \\ &\frac{\exp(-\alpha_p d_2 N) + \exp(-\alpha_s d_2 N) - 2\exp\left[-(\alpha_p+\alpha_s)d_2 N/2\right]\cos(\Delta k_s d_2)}{N^2(\alpha_s-\alpha_p)^2/4 + \Delta k_s^2}, \end{aligned} \tag{6.8}$$

where I_p^{in} is the incident probe-field intensity. The last two terms reduce to $(d_2 N)^2$ for small N and $\Delta k_s = 0$, which gives the square-law dependence as shown in theoretical curve 1 in Fig. 46 and Fig. 47, where perfect phase matching is assumed. On the other hand, when there is no absorption, i.e. $\alpha_p = \alpha_s = 0$, the solution will have the form of $|b\rho_{12}|^2 \cdot I_p^{\text{in}} \cdot (d_2 N)^2 \cdot \text{sinc}^2(\Delta k_s d_2/2)$, which has typical CARS signal dependence on Δk_s and the interaction length d_2.

We first applied Eq. 6.3 with the assumption of perfect phase matching, i.e. $\triangle k_s = 0$. The calculated curves for the CARS and CSRS dependence on the NaDPA concentration are in a qualitative agreement with our experimental results (theoretical curve 1, Fig. 46 and Fig. 47). The peak values of CARS and CSRS are about the same as in our measurement. They are 160 mM (experiment, 152 mM) and 258 mM (experiment, 252 mM) for CARS and CSRS, respectively. The absorption cross sections used in the calculations are $\alpha_p = 0.042$ mM^{-1}cm^{-1}, $\alpha_{CARS} = 0.083$ mM^{-1} cm^{-1}, and $\alpha_{CSRS} = 0.036$ mM^{-1}cm^{-1}. They are measured experimentally as shown in Appendix A. The fitting parameters are $d_1 = d_3 = 0.725$ and $d_2 = 0.55$ mm. The interaction length d_2 is close to the estimated one from the beam geometry and dispersion. The other two parameters, d_1 and d_3, are taken equal since we have always

tried to center the overlap region in the cuvette.

The theoretical curves exhibit a square-law dependence for small concentration. However, the experimental results show a steeper increase of the signal (the slope is 2.7 on the log-log scale), which can be explained as follows. In our experiment, the geometry of the laser beams is optimized for one particular concentration. The CARS/CSRS signal is measured in the same configuration for different concentrations of NaDPA. However, the calculations show that the absorption of the probe field is substantial because the frequency of the probe beam is close to the resonant electronic transition. Similarly, the resonant dispersion of DPA molecules can contribute and lead to the appearance of phase mismatching for signal generation. The pulse energy has steeper dependence on the NaDPA concentration due to the changing refractive index of the NaDPA solution when the NaDPA concentration increases.

To support this explanation we have measured the index of refraction of the NaDPA solution for two concentrations, 50 and 100 mM. It is measured by using the well-known refractive index of water [83]. Briefly, the beam is refracted through a corner of a quartz cuvette and is projected onto a piece of paper about 3 meters away from the sample. The output angle, and therefore the beam position on the paper, is decided by the refractive index of water or solution to be measured. From the known refractive index of water and the recorded beam positions on the paper for water, 50 mM and 100 mM NaDPA solutions, the refractive index of the NaDPA solutions are calculated and shown in Fig. 48. The error here mainly comes from the uncertainty to which the refractive index of water is calculated [83]. Clearly, this uncertainty translates into an uncertainty in the measured values for the refractive index of the NaDPA solutions. However, the relative error of our measurements is smaller, and is roughly represented by the size of the symbols (squares, triangles, and circles) showing the data points.

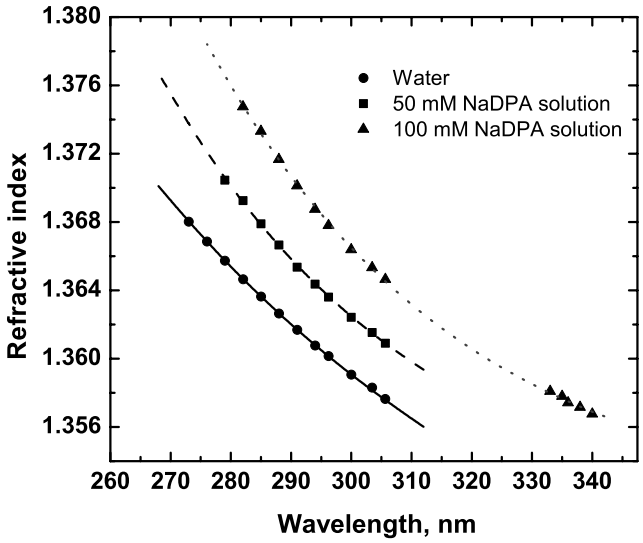

Fig. 48. Refractive index of 50 mM and 100 mM NaDPA solution in the UV range. Dashed line: fitting curve for 50 mM NaDPA solution; dotted line: fitting curve for 100 mM NaDPA solution; solid line: fitting curve from the empirical equation for water.

We fitted the data with an equation similar to the empirical equation for the refractive index of water [83]. The fitting curves are shown in Fig. 48 (dashed line, 50 mM; dotted line, 100 mM) with the experimental data. The fitting equation for the refractive index of 50 mM NaDPA solution is:

$$n(\lambda) = 1.31279 + 59.8991/\lambda - 30562.7/\lambda^2 + 5.11903 \times 10^6/\lambda^3. \tag{6.9}$$

For 100 mM solution, it is:

$$n(\lambda) = 1.31279 + 65.8283/\lambda - 35024.0/\lambda^2 + 6.03199 \times 10^6/\lambda^3. \tag{6.10}$$

Here λ is measured in nanometers.

We see that the refractive index of our solution increases noticeably with increasing concentration of NaDPA. Obviously, phase matching cannot be satisfied at all concentrations. We perform calculations taking into account the resonant dispersion and observe steeper slope for the signal dependence on the NaDPA concentration. We assume a linear dependence of Δk_s on concentration N, i.e. $\Delta k_s = a(N - N_0)$. N_0 is the point where the phase matching is satisfied. We use N_0 and a as fitting parameters, and keep the rest of the parameters fixed as given above. The calculated results are shown as solid curves in Fig. 46 (CARS) and Fig. 47 (CSRS). The parameters used in the calculations are $N_0 = 170$ mM, $a_{CARS} = 0.585$ mM^{-1}cm^{-1}, and $a_{CSRS} = -0.44$ mM^{-1} cm^{-1}. We observe a good agreement between our experimental and theoretical results. One may note that a_{CARS} has a larger magnitude than a_{CSRS} which should be the case since the CARS signal is closer to the absorption peak.

c. Experimental result with a 100 μm cuvette

When the interaction length d_2 is decreased, the phase-matching constraint is relaxed. To further prove our theory, we measure the concentration dependence curve with a

100 μm cuvette (with the energies and diameters of the beams given above). In this case, the interaction length is limited to the cell length, and the phase mismatch complication is eliminated.

We start with 50 mM DPA solution in H_2O/NaOH. The CARS signal, collected with the CCD camera, is shown in Fig. 49. Background subtraction is used to get a high signal-to-noise ratio. Beside the slow beating signal (at ∼130 pixels) between 1435 and 1383 cm^{-1} lines, one can see another fast modulation of the signal at shorter wavelength (smaller pixels), which can be assigned to the quantum beating between 1569 and 1435 cm^{-1} transitions. Here $\lambda_{probe} = 300$ nm, $\lambda_{CARS} = 288$ nm, and a band of 20 pixels is equivalent to ∼1 nm. By fitting the experimental data with an exponential decay function, we find the coherence relaxation time to be about 0.8 ps.

The data shown in Fig. 50 were taken at a probe delay corresponding to the second oscillation peak of the CARS signal (∼1.6 ps away from the FWM zero delay) with 10 s exposure time. For this concentration measurement, $\lambda_{probe} = 295$ nm (Fig. 63) and $\lambda_{CARS} = 283$ nm. Background is acquired with the Stokes beam blocked and is subtracted from the data. The result is shown in Fig. 50. We estimate that 1 arbitrary unit of the signal pulse energy in Fig. 50 roughly corresponds to 0.2 fJ/pulse. To change the sample, the cuvette must be removed and replaced. This could explain the larger error bars than in the previous experiment. The experimental data agrees well with the analytical solution. Also, at lower concentration the slope is 2, as expected. Here $\alpha_p = 0.508$ $mM^{-1}cm^{-1}$ and $\alpha_s = 5.28$ $mM^{-1}cm^{-1}$, which are obtained from our experimental results (Appendix A). We estimate that the beam interaction length is longer than the thickness of the cuvette 100 μm and therefore choose fitting parameters $d_1 = d_3 = 0$ and $d_2 = 100$ μm.

In the present setup, we have demonstrated an unambiguous and distinctive signal from a 10 mM NaDPA solution in a 100 μm cuvette. The interaction volume is

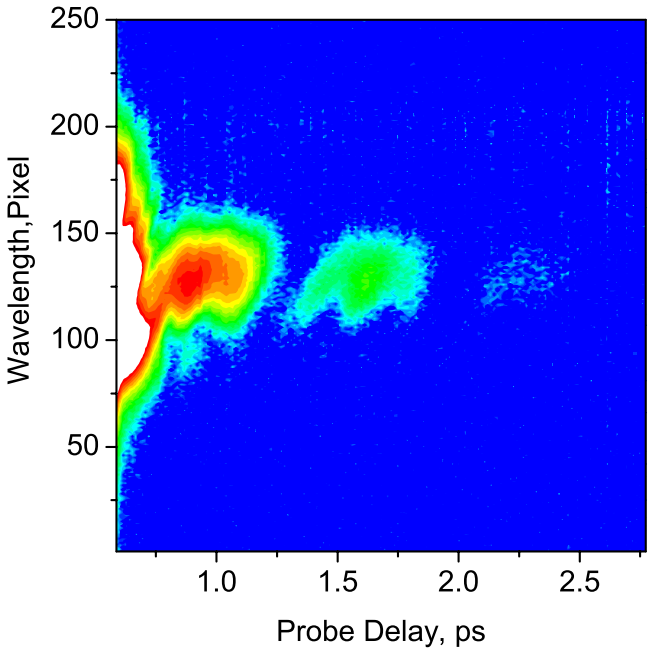

Fig. 49. Logarithmic contour plot of the CARS signal spectrogram as a function of the probe laser delay, acquired with CCD from a 50 mM sample of DPA in H_2O/NaOH in a 100 μm quartz cuvette. Exposure time is 10 s.

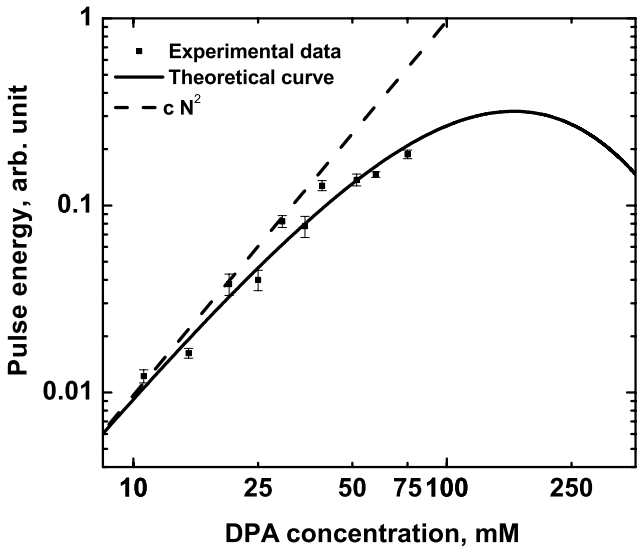

Fig. 50. CARS signal concentration dependence for NaDPA solution in a 100 μm cell. The error is estimated from the three sets of data taken at each concentration; c is a constant.

estimated to be 100 μm $\times$100 μm $\times$100 μm = 10^{-6} cm^3. This corresponds to 6×10^{12} NaDPA molecules contributing to the coherent Raman scattering. The number of DPA molecules (mainly, in the form of CaDPA salt) in one bacterial spore is $\sim 2\times 10^9$. Assuming that the scattering from different spores adds up coherently in the forward direction, our current setup should be able to detect 3×10^3 spores. This is within the limits of a lethal dosage [84]. There are proposed techniques to improve the CARS sensitivity, such as femtosecond adaptive spectroscopic technique (FAST) applied to CARS (FAST CARS) [43] which maximizes the molecular coherence. Additionally, polarization methods may prove useful for removing the nonresonant background and therefore increase the signal-to-noise ratio [85; 86].

C. CSRS in crystalline DPA

Many different form of DPA such as powder, hot solution, DPA salt (NaDPA, CaDPA) have been used for the research of detection of bacteria spores. Here I present the experiment of fs CARS in crystalline DPA. After trial and error we use the following procedure to get a piece of good quality crystal. First heat up 100 ml of distilled water until the temperature is around 60^{o}C. Then add DPA powder until the solution is saturated. After that put the solution in a water bath (about 1 liter) which is inside a box isolated using isolation foam. Let the solution cool down slowly (normally within 12 hours).

We obtain more flake structures with thickness of about 200 μm as shown in Fig. 51 (a) from the solution prepared with the above mentioned procedure. If we filter the solution (100 μm filter paper) before we put it in the isolated box, we obtain more needle structure with diameter of about 300 μm as shown in Fig. 51 (b). If we pick up a good needle crystal as a seed for next crystallization, we obtain long needles. Similarly, if we use a flake structure crystal as a seed, we obtain larger flakes.

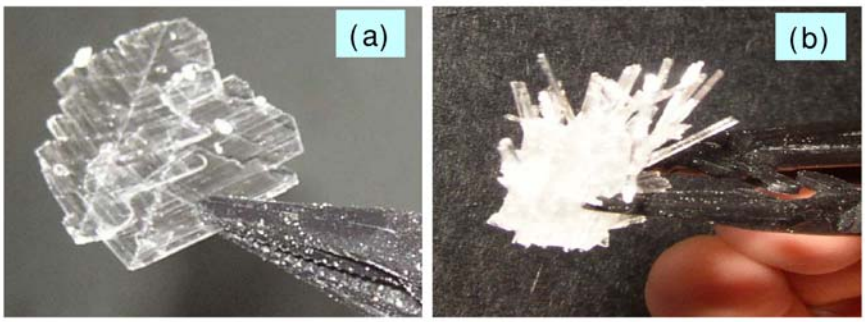

Fig. 51. Two different forms (flake and needle) of crystalline DPA grown under different conditions.

Crystalline DPA has similar Raman spectra as DPA powder. When we apply a pump beam (Yellow) at 579.5 nm, Stokes beam (Red) at 640nm and probe beam (UV)

at 320 nm with the above mentioned BOX CARS geometry (Fig. 44), we observe the degenerate FWM signal from the pump (Y) and Stokes (R) pulses (Fig. 52 (top)). We also observe both the CARS and CSRS signals. We record the CSRS signal as a function of the probe delay. Surprisingly, the CSRS signal from some orientations of the needles has a reflected CSRS signal as shown in Fig. 52 (a), which we find out that it comes from the reflection from the back surface of the crystal. However, other orientations give clear strong CSRS signal as shown in Fig. 52 (b). When we put the needles under a microscope, we find that the needle cross section has hexagonal structures. Therefore, if we focus on the plane, we get weak CSRS beat signal but strong back reflection signal from the crystal (Fig. 52 (a)). If we focus on the corner of the hexagon structure, we get a strong CSRS beat signal (Fig. 52 (b)).

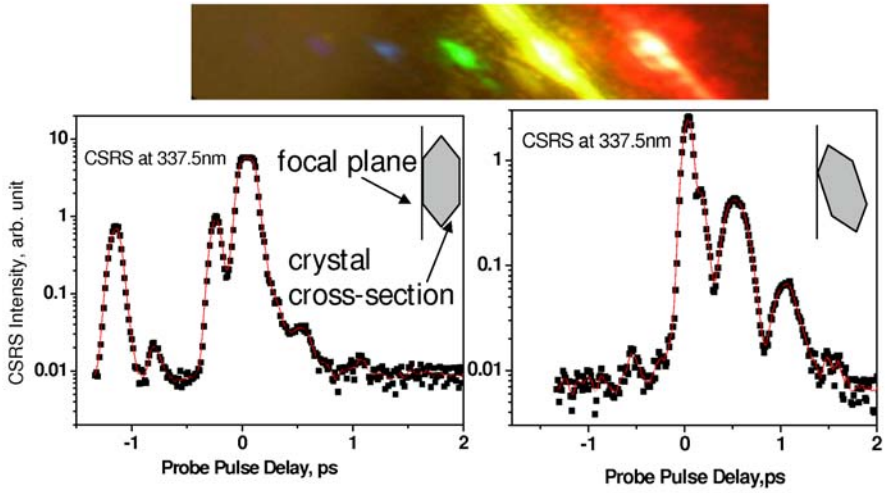

Fig. 52. CSRS signals in DPA crystal depends on whether the focal plane of the laser beam is parallel to one of the long axis of the crystal (left) or not (right). Top: Degenerate FWM in crystalline DPA.

We deduce that when a monocrystal is used, the orientation of its axis with respect to the laser polarization will determine which molecular mode will interact

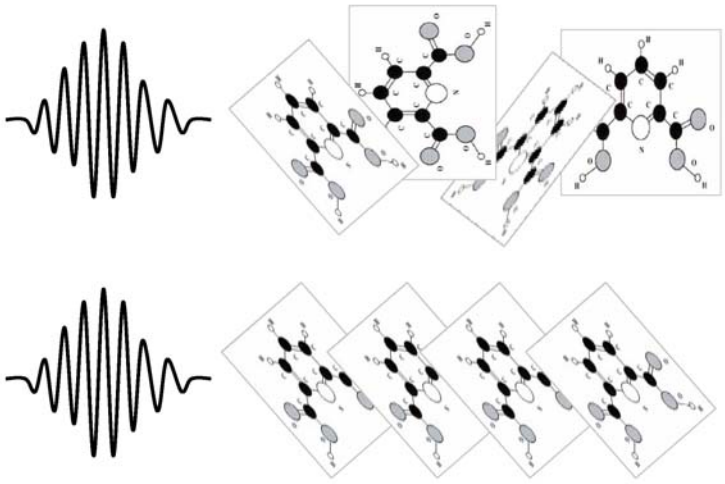

Fig. 53. Schematics of the molecule in a crystal interacting with the light. The orientation of its axis with respect to the laser polarization will determine which molecular mode interacts with light, and how strongly.

with light, and how strongly, as schematically shown in Fig. 53. This is similar to what happens to the bulk crystal that we use for the sidebands generation research.

To prove this, we mount the needle on a rotational mount and observe the CSRS signal at different orientations of the needle. The results are shown in Fig. 54. We can see that the interaction of a molecule with laser light will depend on its orientation with respect to the laser polarization.

D. Conclusion

Femtosecond CARS can be used as an efficient tool for detecting DPA, the marker molecule for bacterial spores. The quantum beating in the signal acquired with a CCD camera gives an unambiguous signature of the molecule. From measuring the concentration dependence of the CARS signal on NaDPA, we observe a power-law dependence at low concentrations, followed by a maximum, and then a signal

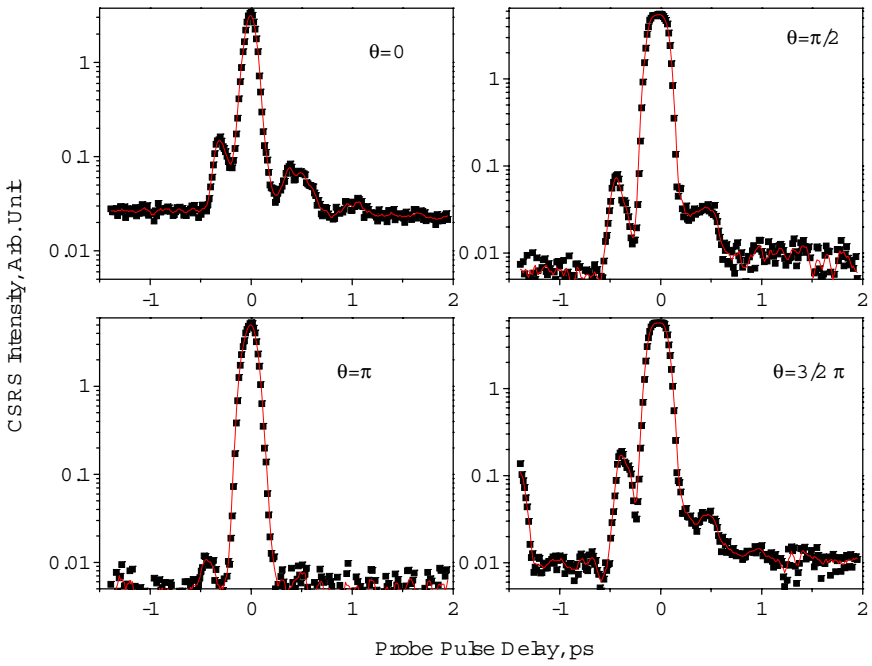

Fig. 54. CSRS signal in DPA crystal (needle form) at different orientations of the needle.

reduction at higher concentrations. But at lower concentration, we have observed slopes having as large as the third power of concentration. A model is used to describe this behavior and an analytical solution is found that agrees with our experimental data. We find that the concentration dependence of the signal has a slope steeper than two (on a log-log scale) and can be explained when dispersion is taken into account. We have established that our technique is a viable alternative for the detection of lethal amounts of anthrax spores. We also study the CSRS signal in the crystalline DPA, which gives us knowledge about how the laser interact with a monocrystal.

Please note that recently, a hybrid CARS technique is invented which deals with the issue of the fluctuating background—a serious problem for detection of backscattering CARS signal from powder. This hybrid technique combines the robustness of frequency-resolved CARS with the advantages of time-resolved CARS spectroscopy

and has made a rapid and highly specific detection of NaDPA powder possible [87].

CHAPTER VII

NUMERICAL STUDY OF NUCLEAR COLLISIONS INDUCED BY SINGLE-CYCLE LASER PULSES: MOLECULAR APPROACH TO FUSION*

A. Introduction

Fusion, which fuels stars, occurs when light nuclei of hydrogen (H), deuterium (D), or tritium (T), join together to produce helium, neutrons, and energy. If harnessed on earth, fusion has the potential to provide a clean and virtually unlimited source of energy. The fusion reaction occurs when two nuclei approach within about 10^{-15} m, where the strong-force attraction between the nuclei overcomes the electrical repulsion. Such close encounters only occur when nuclei collide with sufficient kinetic energy.

The two present techniques for controlled fusion, laser-beam-driven (inertial confinement) and Tokamak (magnetic confinement) fusion, employ different confinement and heating mechanisms for the reactants, but both rely on *hot plasma* (Fig. 55 (a)). Thermal motion of the nuclei in such plasma results in random nuclear collisions, which can be energetic enough to produce fusion when the temperature is very high (10^8 K).

We study a new method, which does not require preparation and confinement of a hot and dense plasma, but works in a molecular gas. This method uses the factthat nuclei in a molecule are pre-aligned in front of each other and can be driven intoeach other by a very strong ultrashort laser pulse (Fig. 55 (b)). The method works for

*Part of this chapter is reprinted from "Nuclear collisions induced by single-cycle laser pulses: molecular approach to fusion," by Sokolov A. V., and Zhi M., 2004, Journal of Modern Optics, 51 (16-18): 2607-2614, copyright 2004, with kind permission from Taylor & Francis.

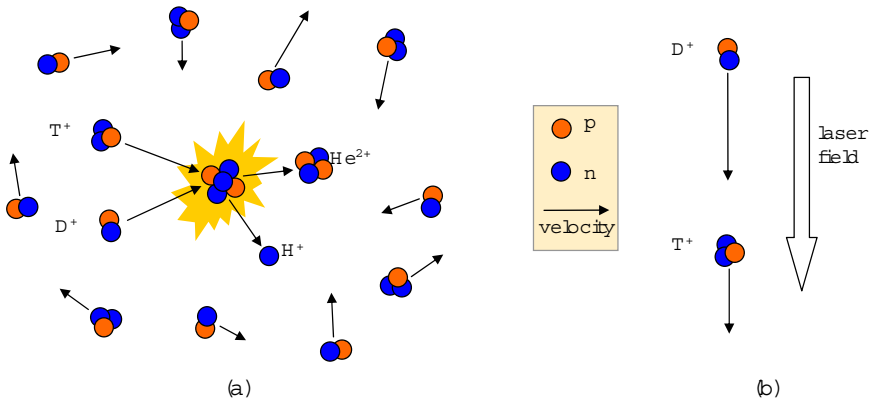

Fig. 55. (a) Nuclear fusion in a hot plasma "soup"; and (b) nuclei pre-aligned for a laser-induced collision.

hetero-nuclear molecules (such as HD, HT, or DT) and relies on the fact that nuclei of different masses will acquire different velocities when driven by the same electric field. When the field is strong enough, it may make the nuclei collide with high kinetic energy needed to overcome the Coulomb barrier. The initial orientation of the molecules with respect to the direction of the laser field can be induced by the leading front of the same strong laser pulse, or can be pre-set by additional laser pulses.

Realization of this technique will require ultrashort (few-femtosecond, single-cycle) laser pulses with field intensities approaching 10^{23} W/cm^2. A short and clean leading pulse front (with no pre-pulse) must assure that after a molecule is fully ionized (at about 10^{15} W/cm^2) the nuclei are still not too far apart when the peak of the pulse arrives. This is because that Coulomb repulsion will make the bare nuclei fly apart on a time scale of 10 fs. Also, the nuclear wavepackets will spread on the same timescale, reducing the probability of a collision. Short near single-cycle pulse duration will also be required for the following reason: If the nuclei experience a

"near-miss" collision on one laser cycle which comes before the pulse peak, they will fly apart and will not have a chance to re-collide. The necessary peak intensity (10^{23} W/cm^2) is set by the requirement that the ponderomotive energy of a nucleus is roughly equal to the Coulomb potential at 10^{-15} m internuclear distance.

Present-day techniques allow production of laser field intensities up to 10^{22} W/cm^2 [88], while generation of ultrashort pulses with peak intensity as high as 10^{23} W/cm^2 should become possible in the near future[5; 89; 90] . Some alternative techniques may also lead to production of ultra-intense single-cycle laser pulses [91; 6].

In earlier work, over a decade ago Corkum has developed a three-step model for high-order harmonic generation [92]. According to that model, an electron is separated from an atom and accelerates under the action of a strong laser field, gains energy and re-collides with the parent ion. Recently Corkum and coworkers have proposed to use the returning electron as a fast probe of atomic and molecular dynamics [93]. In that paper they have also alluded to the possibility that a nucleus can be considered in place of the electron. Very recently Bandrauk and Corkum discussed a possibility to achieve nuclear fusion by applying a strong laser field (10^{22} W/cm^2) to a D_2^+ ion with a muon in place of the electron [94; 95]. The work by Ivanov and Smirnova on laser-driven motion of two nuclei of unequal masses [96] is also closely related to the present idea.

B. Classical simulation

In order to gain a qualitative understanding of the laser-induced nuclear collision process we first perform a classical simulation, where the nuclei are treated as point particles. In our simulation we use hydrogen and tritium with equal nuclear charges $q_1 = q_2 = 1.6 \times 10^{-19}$ C, and masses $m_1 = 1.67 \times 10^{-27}$ kg, $m_2 = 3 \times 1.67 \times 10^{-27}$ kg.

The nuclei move under the action of the Coulomb repulsion and a strong laser field **E** such that the total force on each of the nuclei is:

$$\mathbf{F}_{1,2} = q_{1,2}\mathbf{E} \pm k\frac{q_1 q_2(\mathbf{r}_1 - \mathbf{r}_2)}{|\mathbf{r}_1 - \mathbf{r}_2|^3} = m_{1,2}\ddot{\mathbf{r}}_{1,2}, \tag{7.1}$$

where $\mathbf{r}_{1,2}$ are the position vectors of the nuclei, $\ddot{\mathbf{r}}_{1,2}$ are the accelerations of the nuclei, and k is the Coulomb's constant.

1. Linearly polarized laser field

We first consider a linearly polarized field and assume 10^{21} W/cm^2 laser intensity. The amplitude of the electric field is $E_0 = 8.68 \times 10^{13}$ V/m and $E_x = E_0 \times \cos[\omega(t - t_0)]e^{\frac{-(t-t_0)^2}{\tau^2}}$, where we take $t_0 = 5$ fs, $\omega = 2\pi c/\lambda$, $\lambda = 0.5\mu m$, $\tau = 1.5$ fs.

We assume the nuclei originate from an HT molecule, oriented along the laser polarization, with both electrons removed by the strong laser field at t=0, when the internuclear distance is 1 Å. The peak laser intensity 10^{21} W/cm^2 is more realistic, but not sufficient yet for nuclear fusion. The shortest distance between the two nuclei is about 2×10^{-13} m, and the width of the short pulse generated at the time of the collision is about 0.4 attosecond. The results of the simulation are shown in Fig. 56.

2. Elliptically polarized laser field

A simple extension to consider is to use elliptical laser polarization, instead of linear as assumed in Fig. 56, to explore elliptical nuclear motion instead of linear. In this simulation we assume 10^{23} W/cm^2 laser intensity. The amplitude of the electric field is $E_0 = 2.21 \times 10^{14}$ V/m. The components of the electric field in the x and y direction are

$$E_x = 0.1047387E_0 \times \cos[\omega(t - t_0)]e^{\frac{-(t-t_0)^2}{\tau^2}}, \tag{7.2}$$

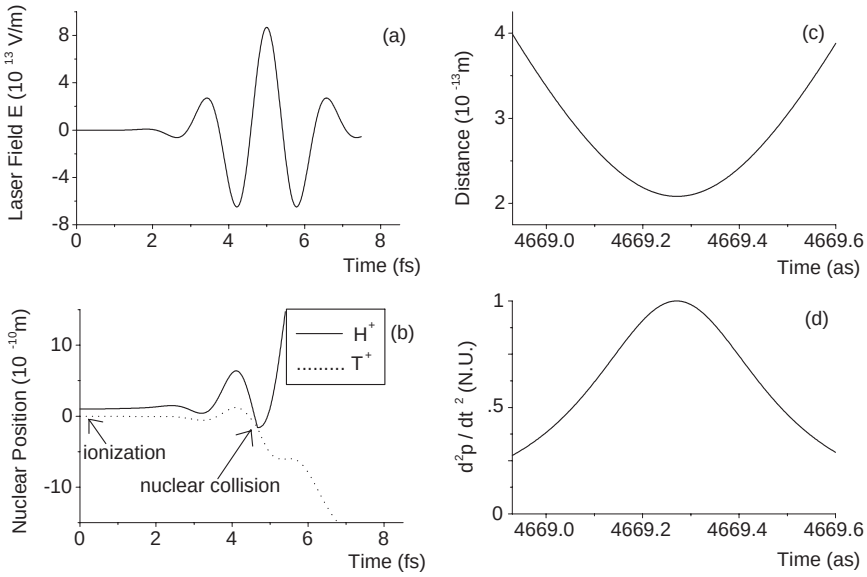

Fig. 56. Classical simulation of a laser-induced nuclear collision between H^+ and T^+. Part (a) shows the single-cycle laser pulse; part (b) shows the calculated nuclear motion; part (c) shows the distance between the nuclei at the time the collision happens; part (d) shows the second derivative of the system's dipole moment p, which results in an X-ray burst of sub-attosecond (10^{-18}s) duration.

and

$$E_y = E_0 \times \cos[\omega(t - t_0) + \frac{\pi}{2}]e^{\frac{-(t-t_0)^2}{\tau^2}}. \quad (7.3)$$

Here $t_0 = 10$ fs, $\tau = 1.2 \times 10^{-15}$s, ω and λ are the same as in the previous simulation.

The two nuclei initially are 1 Å apart and are aligned along the x direction. We adjust the ellipticity of the laser field such that the nuclei collide with each other in y direction at the peak of the short pulse laser field, t_0=10 fs. When we change the initial separation to 1.5 Å and 2 Å, we see similar collision picture once the electric field is adjusted. The results are shown in Fig. 57.

In contrast to the previous example (at 10^{21} W/cm^2 intensity), now (at 10^{23} W/cm^2 intensity) the minimum distance between the two nuclei is close to 10^{-15} m, where a fusion reaction may occur. The collision results in a large and very brief acceleration and produces a zeptosecond burst of light (charge × acceleration = radiation). The short light pulse generated during the collision is now on a zeptosecond (10^{-21} s) time scale and 10^4 times stronger than in the previous case.

C. Statistical ensemble simulation

The most suitable reaction occurs between the nuclei of the two heavy isotopes of hydrogen—deuterium and tritium. Therefore in this part of the simulation, we use deuterium and tritium nuclei instead of the hydrogen and tritium in the previous cases. Quantum mechanically speaking, deuterium and tritium nuclei should be represented by two wavepackets. When they overlap, there is a finite probability that the two nuclei will collide and fly apart (or fuse). We assume that the molecules are aligned along the laser field, such that each of the nuclei is confined in a three-dimensional harmonic potential. We generate ensembles of nuclei with random locations but with overall Gaussian distributions: $\frac{1}{\sqrt{2\pi\sigma}}e^{\frac{-r^2}{2\sigma^2}}$, where $\sigma = \frac{r_{max}}{\sqrt{2}}$, $\mathbf{r}$ is

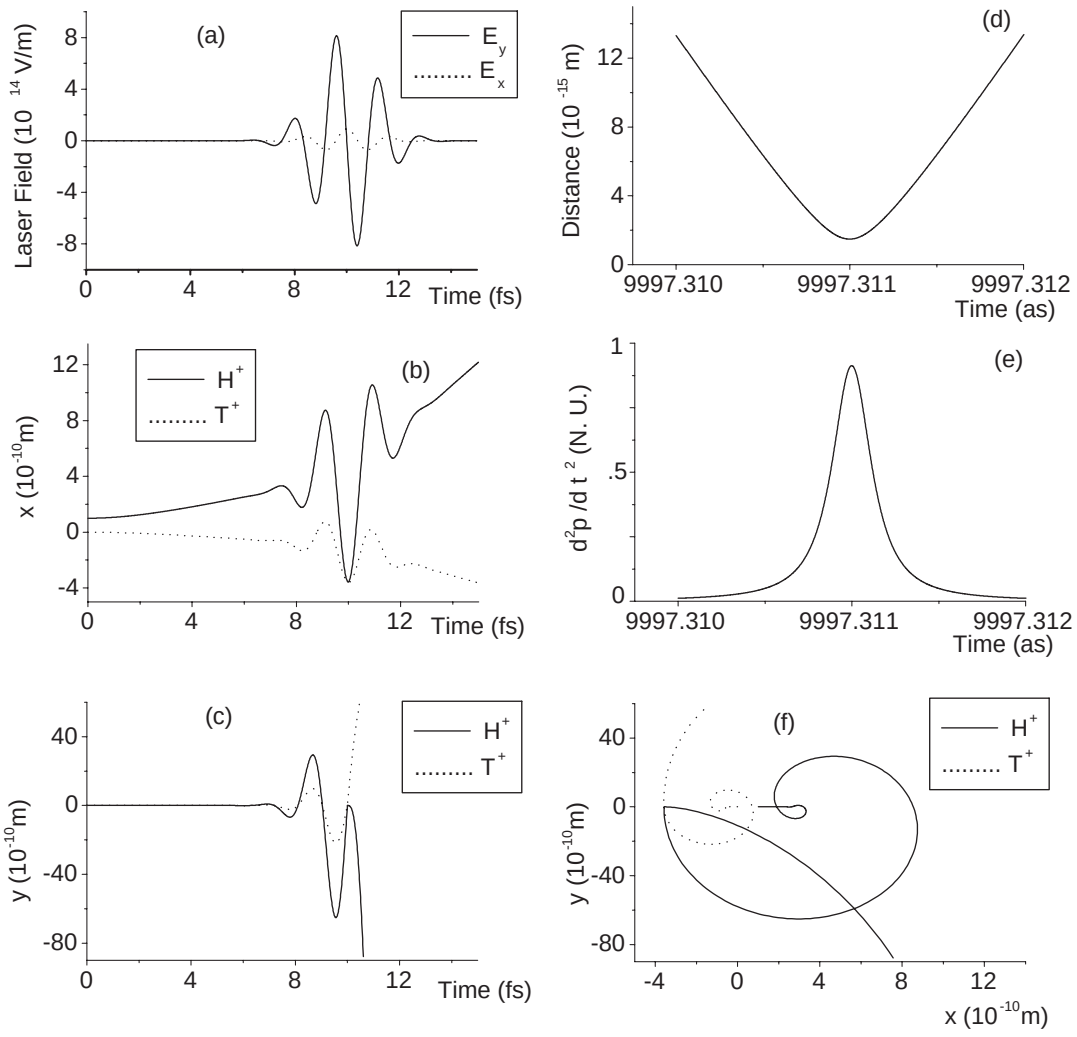

Fig. 57. Classical simulation of a nuclear collision between H^+ and T^+ induced by an elliptically polarized laser pulse. (a) the electrical field of the ultrashort pulse; (b) the motion of the two nuclei in x direction; (c) the motion of the two nuclei in y direction; (d) the distance between the two nuclei when the collision happens; (e) the short pulse generated due to the collision; (f) two-dimensional trajectories of the two nuclei.

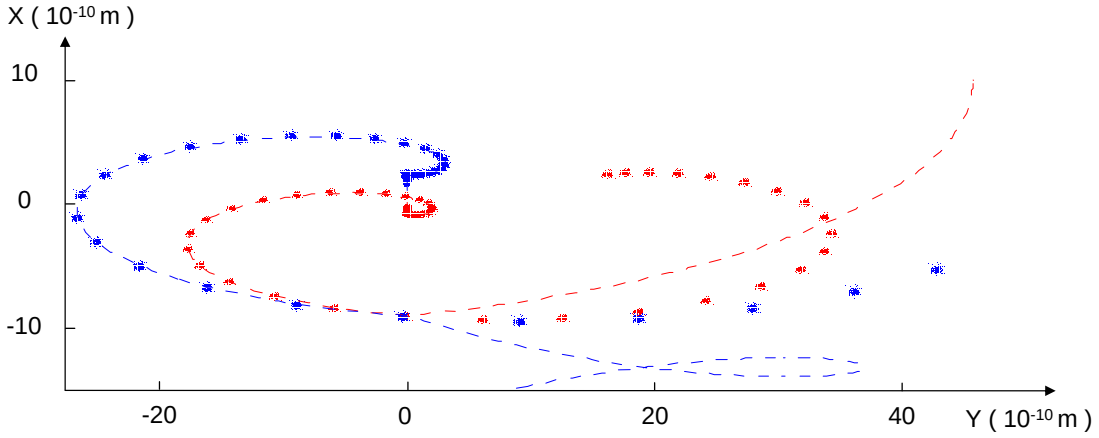

Fig. 58. The motion of the two nuclear ensembles under the action of elliptically polarized laser field. Clouds of red dots show the ensemble of T^+ nuclei at different moments of time projected onto the X-Y plane; blue dots show the D^+ ensemble. Dashed lines are the classically calculated parametric trajectories for a single pair of nuclei (D^+ and T^+) under the same laser field as used in the ensemble calculation, but with initial positions and velocities precisely right for a collision.

the displacement of a nucleus from the center and r_{max} is 10^{-11} m for hydrogen, 8.4×10^{-12} m for deuterium, and 7.6×10^{-12} m for tritium. Once the location of the nucleus is fixed, by using the energy conservation and assuming the ground state energy equal to $\frac{1}{2}\hbar\omega$ (where $\omega = \sqrt{\frac{k}{m}}$ and $k = \frac{\hbar^2}{mr_{max}^2}$), the initial velocity (absolute value) is determined from equations: $\frac{1}{2}kr_{max}^2 = \frac{1}{2}\hbar\omega$ and $\frac{1}{2}kr_{max}^2 + \frac{1}{2}mv_0^2 = \frac{1}{2}\hbar\omega$. We obtain

$$v_0 = \frac{\hbar}{mr_{max}}\sqrt{1 - \frac{r^2}{r_{max}^2}}. \tag{7.4}$$

In this part of the simulation the electric field we used has the form:

$$E_x = E_0 \times \cos[\omega(t - t_0)]e^{\frac{-(t-t_0)^2}{\tau^2}}; \tag{7.5}$$

and

$$E_y = 0.3E_0 \times \cos\left[\omega(t-t_0) + \frac{\pi}{2}\right] e^{\frac{-(t-t_0)^2}{\tau^2}}. \tag{7.6}$$

where $E_0 = 2.29 \times 10^{14}$ V/m, $t_0 = 10$ fs, $\tau = 1.2 \times 10^{-15}$ s, ω and λ are the same as in the previous simulation.

In Fig. 58 we show the motion of the two ensembles of nuclei together with a single pair of nuclei under the same laser field. The trajectory of the single pair of nuclei (dashed curves) is calculated classically. We can see that at about y=0, the nuclei collide and then deflect. However, since the probability of a strong collision is very low, we didn't see it happen in our ensemble calculation.

D. Quantum calculation

We perform a quantum-mechanical calculation for two nuclei (of unequal mass) in a strong laser field. Even though for two nuclei of equal mass an analytical solution exists, when the two masses are unequal a numerical solution is necessary. The classical analysis allows us to obtain the trajectories which we can use as a reference for the quantum calculation. It also allows studying the nuclei individually or collectively, since we can do classical ensemble simulation. The quantum calculation enables us to see the wavepacket behavior at the collision point and can also incorporate easily the effect of magnetic field if we use space dependent vector potential in the future.

The Hamiltonian for the relative motion of the two charges in a laser field with vector potential A is:

$$H = \frac{1}{2m_1}(p_1 - \frac{q_1 A}{c})^2 + \frac{1}{2m_2}(p_2 - \frac{q_1 A}{c})^2 + \frac{q_1 q_2}{R}. \tag{7.7}$$

Let $R = r_1 - r_2$, $R_{cm} = \frac{m_1 R_1 + m_2 R_2}{m_1 + m_2}$, p=$\frac{m_2 p_1 - m_1 p_2}{m_1 + m_2}$, $p_{cm} = p_1 + p_2$, M=$m_1 + m_2$,

$\mu = \frac{m_1 m_2}{m_1+m_2}$, q=$\mu(\frac{q_1}{m_1} - \frac{q_2}{m_2})$, we get

$$H = \frac{p^2}{2\mu} - \frac{q\mathbf{p}\cdot\mathbf{A}}{c\mu} + \frac{q_1 q_2}{R} + \frac{A^2}{2c^2}\left(\frac{q_1^2}{m_1} + \frac{q_2^2}{m_2}\right) + \frac{p_{cm}^2}{2M} - \frac{2p_{cm}qA}{cM}. \tag{7.8}$$

The last two terms are related with center of mass energy. Therefore in the center of mass frame the Hamiltonian can be written as [96]:

$$H_{rel} = \frac{p^2}{2\mu} - \frac{q\mathbf{p}\cdot\mathbf{A}}{c\mu} + \frac{q_1 q_2}{R} + \frac{A^2}{2c^2}\left(\frac{q_1^2}{m_1} + \frac{q_2^2}{m_2}\right). \tag{7.9}$$

The non-dipole Schrödinger equation in two dimensions (assuming the vector potential is polarized in x direction) is therefore:

$$\begin{aligned} i\frac{\partial}{\partial t}\psi(x,y,t) \quad &= [-\tfrac{1}{2}(\tfrac{\partial^2}{\partial x^2} + \tfrac{\partial^2}{\partial y^2}) - \tfrac{i}{c}A(x,t)\tfrac{\partial}{\partial y} + \tfrac{1}{2c^2}\left(\tfrac{q_1^2}{m_1} + \tfrac{q_2^2}{m_2}\right)A(x,t)^2 \\ &\quad + \tfrac{q_1 q_2}{\sqrt{x^2+y^2}}]\psi(x,y,t). \end{aligned} \tag{7.10}$$

Note here the effect of the magnetic field is also included in the calculation.

We choose a hetero-nuclear molecule HT for our simulation. Atomic units (e=m=η=1 a.u. and c=137 a.u.) are used throughout this paper except when specific units are given. Let charge 1 and 2 be hydrogen and tritium nuclei separately then m_1=1836.15, m_2 =5508.45; q_1=1; q_2=1.

We assume the nuclei originate from an HT molecule, oriented along the laser polarization (x direction), with both electrons removed by the strong laser field at t=0, when the internuclear distance is 1.88973 (1 $\mathring{A}$). We also assume an overall Gaussian distribution: $2\pi r_{max}^{-3/2}\exp[-r^2/(2r_{max}^2)]$, where r_{max} is the displacement of a nucleus from the center and is about 10^{-11} m for hydrogen and 7.6×10^{-12} m for tritium. In the center of mass frame, the initial wavefunction has the form: $1/\sqrt{\sqrt{\pi}*\sigma}\exp[-(x-x_0)^2/(2\sigma^2)]$ for one-dimensional (1-d) case. The initial position of the wavepacket is x_0. $\sigma = 0.237336$ is obtained from the above r_{max} for hydrogen

and tritium nuclei.

Now in the Hamiltonian, R is the relative distance between H and T nuclei, reduced mass μ=1377.43, effective charge q=0.5.

If we use dipole approximation, i.e., assume that the vector potential is not space dependent, then the last term of the Hamiltonian only gives a time dependent phase [97]. So in atomic units the Schrödinger equation needs to be solved reduced to

$$i\frac{\partial}{\partial t}\psi(x,t) = (-\frac{1}{2\mu}\frac{\partial^2}{\partial x^2} + \frac{iq}{c\mu}A_x\frac{\partial}{\partial x} + 1/|x|)\psi(x,t). \tag{7.11}$$

for 1-d case.

There are several ways to get numerical solution of the Schrödinger equation. One very popular algorithm is Crank-Nicholson finite-difference method [98]. We use second-order split-operator method [99; 100] while the time dependence was developed by Siu A. Chin *et al.* [101]. The algorithm is more stable compared to Crank-Nicholson method which we also tried to use to solve the equation (please refer to appendix B for the code). The second-order split-operator method can be applied to our calculation as following.

The Schrödinger equation $i\frac{\partial}{\partial t}\psi(t) = H\psi(t)$ has the solution with the general form: $\psi(t) = \exp(-iHt)\psi(0)$. If we let H(t) = T(t) + V, i.e. split the Hamiltonian to a part which has an operator and another part doesn't, then $T(t) = -\frac{1}{2\mu}\nabla^2 + \frac{iq}{c\mu}A(t)\cdot\nabla, V = \frac{q_1q_2}{r_{12}}$. For small dt, we can get:

$$\begin{aligned}
\psi(t+dt) &= \exp(-iHdt)\psi(t) = \exp -idt[T(t)+V] \\
&= \exp(-idt\tilde{V}/2)\exp[-idtT(t)]\exp(-idt\tilde{V}/2)\psi(t) \\
&= \exp(-idtV/2)\exp[-idtT(t+dt/2)]\exp(-idtV/2)\psi(t),
\end{aligned} \tag{7.12}$$

where $\tilde{V} = V + \tilde{D}$, and $\tilde{D}$=iD. $D = \frac{\vec{\partial}}{\partial t}$ is the forward time derivative operator. The effect of $\exp(-idt\tilde{V}/2)$ can be implemented as a simple multiplication in the coordinate space. Using one-dimensional Schrödinger equation as an example, the effect of $\exp[-idtT(t+dt/2)]$ can be implemented as following:

$$T(t) = -\frac{1}{2\mu}\frac{\partial^2}{\partial x^2} + \frac{iq}{c\mu}A_x\frac{\partial}{\partial x}, \tag{7.13}$$

$$\begin{aligned} \exp(\varepsilon t)\exp(ikx) &= \exp[-\frac{1}{2\mu}(ik)^2 + \frac{iq}{c\mu}A(t)*(ik)] \\ &= \exp\{\varepsilon[\frac{1}{2\mu}k^2 - \frac{q}{c\mu}A(t)k]\}. \end{aligned} \tag{7.14}$$

Here ε=-idt. Let $\psi(x,0) = \sum_k \psi(k,0)$ and $\psi(k,\triangle t) = \psi(k,0) * \exp\{\varepsilon[\frac{1}{2\mu}k^2 - \frac{q}{c\mu}A(t)k]\}$, then

$$\begin{aligned} \exp(\varepsilon t)\psi(k,0) &= \sum_k \psi(k,0)\exp\{\varepsilon[\frac{1}{2\mu}k^2 - \frac{q}{c\mu}A(t)k]\}\exp(ikx) \\ &= FFT^{-1}\psi(k,\triangle t). \end{aligned} \tag{7.15}$$

Therefore, for each time iteration, we have :

$$\begin{aligned} &\psi(x,t+dt) \\ &= \exp[\varepsilon/2V(x)]FFT^{-1}\{\exp\{\varepsilon[\tfrac{1}{2\mu}k^2 - \tfrac{q}{c\mu}A(t)k]\} * FFT\{\exp[\varepsilon/2V(x)]\psi(x,t)\}\}. \end{aligned} \tag{7.16}$$

1. 1-d quantum-mechanical calculation results and comparison with classical simulation

In the earlier classical calculation, we showed the classical calculation in the lab frame, starting the calculation with electric filed. In order to compare with the quantum calculation result we start the calculation with vector potential and the

corresponding electric field has slightly different parameters. The classical results will be shown with the quantum calculation result for comparison. First we carry out the classical calculation with field which is linearly polarized in the x direction. The vector potential is

$$A_x(t) = A_0 \times \cos[\omega(t-t_0)] \exp[\frac{-(t-t_0)^2}{\tau^2}], \tag{7.17}$$

here $A_0 = -6.945\times10^5$. It is chosen such that at the collision point of the two charges, the shortest distance between them is 3×10^{-14} m. The cross section of the DT collision with tritium at rest increases as the deuterium energy increases but flatten out at around 100 kev with a value of 15.4 millibarns [102]. This energy corresponds to 60 kev of relative energy in the center of mass frame. At the distance we choose, the cross section of DT fusion is already significant (11.2 millibarns) [103]. What happens is the very strong tunnelling in the DT. We expect the similar tunnelling effect in HT reaction. Also, if we choose DT instead of HT for our simulation, the electric field needed to bring the two nuclei to the chosen distance is about 3 times higher than that is needed for HT collision. ω=0.0911928, which corresponds to 500 nm wavelength; t_0 = 413.394 (10 fs); τ=49.6073 (1.2 fs). The electric field can be obtained by: $E_x(t) = -\frac{1}{c}A_x^{'}(t)$, the peak amplitude is about 462.166 (2.376×10^{14}V/m) and the corresponding intensity required is around 7.5×10^{21} W/cm^2 .

We employ a Cartesian grid of 2^{16} points with spatial separation between two consecutive points $\triangle x = 32/2^{16}$ (2.58×10^{-14} m), which is set by the shortest distance we want to observe. We let the initial 1-d Gaussian wavepacket propagates on this grid with time step of 0.1 sometime before the collision point and 0.0001 around the collision point. The time step has to be small enough to get a stable and reasonable result. We use complete reflection to deal with the infinity potential at the origin, i.e. after each iteration, we set the wavefunction at the first grid x=0.000488 to be zero.

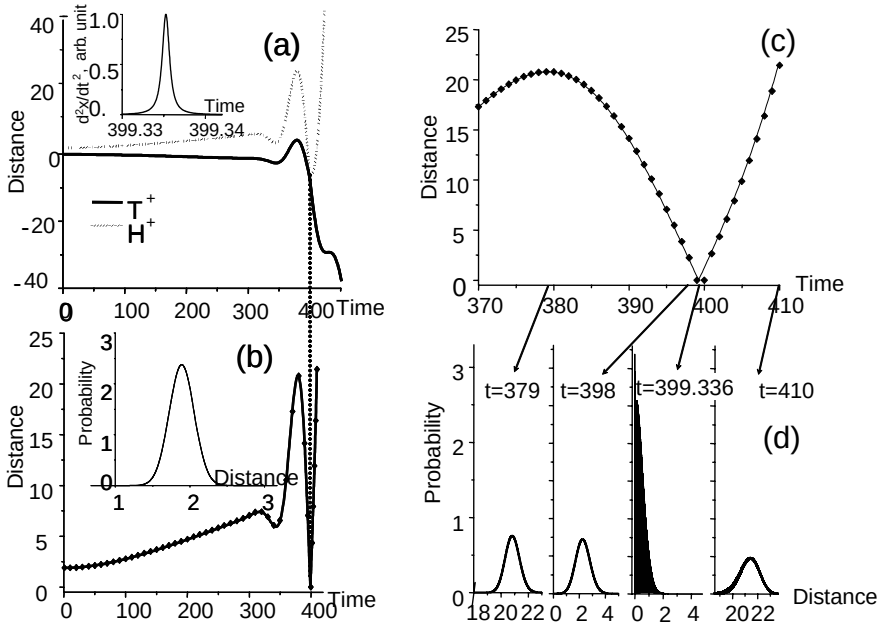

Fig. 59. Simulation of a laser-induced nuclear collision between H^+ and T^+. (a) collision picture in the lab frame (H^+, dotted curve, T^+, solid curve), insert: the sub attosecond (2.4×10^{-20} s) pulse generated at the collision point; (b) calculated nuclear motion in the center of mass frame(classical, solid line, quantum, scattered diamond), insert: initial Gaussian wavepacket used for the numerical solution of the Schrödinger equation. (c) movement of the wavepackets around the collision point; (d) probability density plots of the wavepackets at different time.

In Fig. 59 we show results from both the classical and quantum calculation. Classically, the two nuclei fly apart due to coulomb potential in the beginning and later start to move under the electric filed and collides at time 399.336. Quantum mechanically speaking, the wavepacket moves toward the center and then reflect back from the infinity potential, the wavepacket spreads out as time goes by. We can see the trajectories from classical calculation (solid curve) and from the quantum calculation (dotted line) coincide well (less data points are used for the plot for visual clarity). The shortest distance between two nuclei can be 3×10^{-14} m or less if the fields used are stronger. Fig. 59 (b) shows the probability of the wavepacket at following time: t=379, where the wavepacket is driven by the laser field to far way; t=398, where the wavepacket is driven to the origin; t=399.336, where the collision happens at the classical simulation. If looked closer, the dark area has oscillations which may come from the interference between the incoming and reflecting waves. It may also be due to the extremely smaller grid size $\triangle x$ we are using such that $\exp(-i\triangle t/\triangle x)$ causes the oscillation. At t=410, the wavepacket revives to approximately a Gaussian. The initial wavepacket has a width of 0.5 and spreads out to 1.5 at the end. We have tried to put the absorber at the boundary to avoid the reflection from the boundary. The closest distance, which is what we are interested in, is the same as the one we obtained without using the absorber. There is high probability of the wave function getting to the region where the nuclear fusion is possible since we can see that at the collision point the wavepacket is highly compressed to the origin due to the strong field.

We calculate the closest approach for a less intense electric field than we used. The ponderomotive energy in our case is $U_p = \frac{q^2 E^2}{4\mu\omega^2}$, here q is effective charge and μ is the reduced mass which are given earlier. By equaling with the coulomb potential, we can get the minimum distance r_{min} the field can drive the nuclei to. $E_0 = 2.376 \times 10^{14}$

V/m, which is used for 1-d simulation. The result is shown in table II, where r_{min} has the unit of 10^{-14} m. We see that the distance calculated from different approaches is about the same order of magnitude except for a very low field, when the nuclei just fly apart so the minimum distance is the same as the initial distance we set (10^{-10} m).

Table II. The minimum internuclear distance ($\times 10^{-14}$ m) at the different laser fields calculated from the different approaches.

Electric field	r_{min} (classical)	r_{min} (quantum mechanical)	$r_{min}(\frac{kq_1q_2}{Up})$
E_0	2.99	7.75	4.52
$3E_0/4$	5.97	10.34	8.04
$E_0/2$	27.4	31.0	18.2
$E_0/4$	10^4 (intial distance)	703	72.6

In order to find the relation between the minimum internuclear distance and the peak intensity of the electric field being applied, we calculate the closest distance as a function of the peak electric field as shown in Fig. 60, in which we also shows the closest distance calculated from 1.4 Up of the field at the peak intensity. We see that when the peak field intensity is from around 350 a.u. to 1800 a.u., the two curves coincide well with each other.

For the higher field, we look at the dependence of the time when the internuclear distance is a minimum (collision time) on the peak electric field as shown in Fig. 60 (right Y). From the figure we can see that at the point where the two curves start to disagree at the high field, the collision time shifted from negative electric field to the positive side (E=0 at t=397.69). The minimum internuclear distance increases due to the much closer approach at the first local maxim of the electric field (near miss collision).

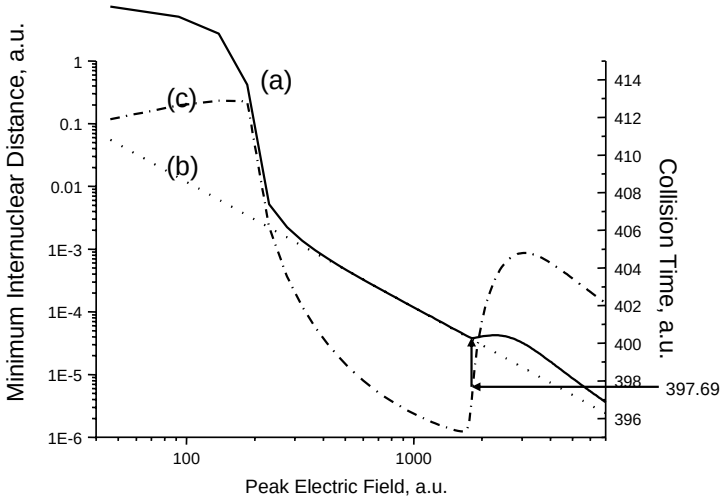

Fig. 60. (a) (Solid line) Minimum internuclear distance as a function of the peak electric field from a 1-d quantum-mechanical calculation; (b) (dotted line) Minimum internuclear distance calculated from 1.4 Up; (c) (dash-dotted line) Closest approach (collision) time vs. the peak electric field.

For the lower field, the difference could be due to the initial condition of nuclear distance 1 Å we set. We calculate the minimum internuclear distance at different peak electric field with different initial internuclear distance. We find that at certain initial condition (2 Å), the distance calculated from the ponderomotive energy coincide well with the minimum distance calculated classically until very low field. By varying the pulse length, we can find another minimum internuclear distance at the same peak electric field in the lower field region when $\tau = 33$ a.u. (0.8 fs). The parameters can be optimized more to achieve closer approach but we are interested in the region around where the distance calculated from 1.4 ponderomotive energy can give a good prediction.

2. 2-d quantum-mechanical calculation results and comparison with classical simulation

During the 1-d calculation, we realized that 1-d is too unrealistic and easily gives artificial results due to the large grid size or the large time step. For example, we see the wavepacket penetrate the infinity potential at intense fields if the grid size $\triangle x$ is larger than $32/2^{16}$ or $\triangle t > 0.001$. For a more realistic model we consider the two-dimensional (2-d) case when the elliptically polarized beam is being used. For this case, the dynamics of the wavepacket at the collision point will be richer than for the 1-d case where the movement of the wavepacket is limited to 1-d. The very large grids ($2^{14} \times 2^{14}$) that have to be employed to get to the resolution of 3×10^{-14} m make the problem very difficult to solve because of large memory requirements. With parallel computers available they are not prohibitively computation demanding but due to the memory limit we can't have as small resolution as in the 1-d calculation.

So in atomic units the Schrödinger equation that needs to be solved in 2-d case is:

$$i\frac{\partial}{\partial t}\psi(x,y,t) = \quad (7.18)$$
$$= [-\frac{1}{2\mu}(\frac{\partial^2}{\partial x^2} + \frac{\partial^2}{\partial y^2}) + \frac{iq}{c\mu}A_x(t)\frac{\partial}{\partial x} + \frac{iq}{c\mu}A_y(t)\frac{\partial}{\partial y} + 1/\sqrt{x^2+y^2}]\psi(x,y,t).$$

If we split the Hamiltonian to T and V as in the 1-d case and let

$$T = -\frac{1}{2\mu}(\frac{\partial^2}{\partial x^2} + \frac{\partial^2}{\partial y^2}) + \frac{iq}{c\mu}(A_x(t)\frac{\partial}{\partial x} + A_y(t)\frac{\partial}{\partial y}); \quad (7.19)$$

and

$$V = \frac{1}{\sqrt{x^2+y^2}}. \quad (7.20)$$

Here $\varepsilon = -idt$. Then

$$\begin{aligned} \psi(x,y,t+dt/2) &= e^{\varepsilon H(t+\triangle t/2)}\psi(x,y,t) = \\ &= e^{\varepsilon(T+V)}\psi(x,y,t) = e^{\frac{\varepsilon V}{2}}e^{\varepsilon T}e^{\frac{\varepsilon V}{2}}\psi(x,y,t). \end{aligned} \tag{7.21}$$

Therefore for each iteration, we have:

$$\begin{gathered} \psi(x,y,t+dt/2) = \\ e^{\varepsilon V/2}FFT^{-1}\{e^{\varepsilon[\frac{k_x^2+k_y^2}{2\mu}-\frac{q}{c\mu}(A_xk_x+A_yk_y)]}FFT\{e^{\varepsilon V/2\psi(x,y,t)}\}\}. \end{gathered} \tag{7.22}$$

The components of the vector field in the x and y direction are

$$A_x(t) = 0.474436A_0 \times \sin(\omega t)\exp[\frac{-(t-t_0)^2}{\tau^2}], \tag{7.23}$$

and

$$A_y(t) = A_0 \times \sin(\omega t + \pi/2)\exp[\frac{-(t-t_0)^2}{\tau^2}]. \tag{7.24}$$

Here τ=62.0121 (1.5 fs), t_0, ω and λ are the same as in the previous simulation. $E_x(t) = -\frac{1}{c}A_x'(t)$, $E_y(t) = -\frac{1}{c}A_y'(t)$, $A_0 = -0.65 \times 10^6$. The peak intensity required is 6.56×10^{21} W/cm^2. For the classical calculation, unlike in the 1-d case, where we only adjust the intensity of the field, here we adjust carefully both the ellipticity and the intensity so that the two nuclei have a head on collision at the peak intensity of the laser pulse. We then use these parameters for our quantum simulation. Similarly as in the 1-d case, strong collision happens and very short pulse is emitted.

In Fig. 61 we show the collision picture both in the lab frame (Fig. 61 (a)) and center of mass frame (Fig. 61 (b)). For the 2-d calculation, due to the high grid size, it is extremely difficult to look closely at the collision point. Our resolution is 0.0027 a.u. (1.43×10^{-13} m). In Fig. 62 we show the contour plot of the logarithm of the modulus squared of the wavefunction at different times. The behavior of the wavepacket is

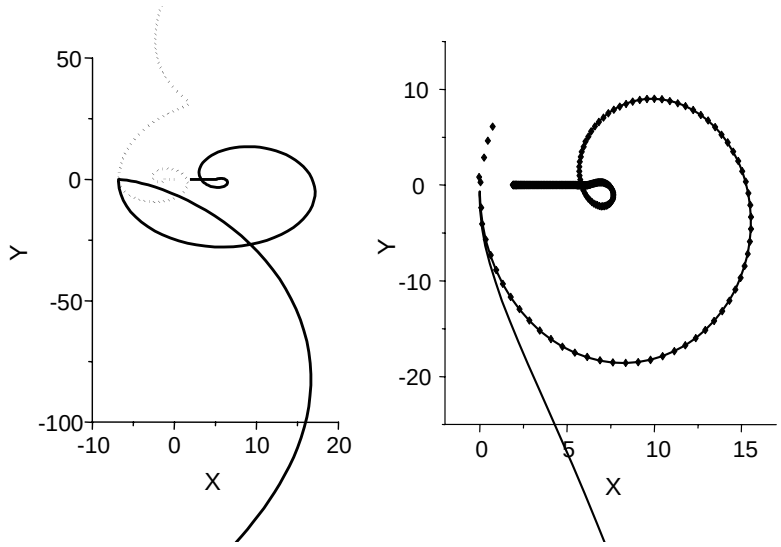

Fig. 61. Classical simulation of a nuclear collision between H^+ and T^+ induced by an elliptically polarized laser pulse. (a) the motion of the two nuclei in the lab frame(H^+, solid curve, H^+, dotted curve); (b) the motion of the two nuclei in the center of mass frame.

similar to the 1-d case before the collision. The wavepacket spreads out much faster in the y direction than in the x direction. This we believe is due to the coulomb repulsion between the two nuclei since when we use a circularly polarized laser field we see similar elongation in the y direction. Our classical ensemble simulation also shows a similar result. At time 413.5 when the collision has happened, we again see some oscillations. The wavepacket is split at the center and is pushed around the origin. After the collision, the wavepacket moves under the electric field instead of being reflected as shown in the classical case. At t=418, the wavepacket is completely split into two parts.

We also make an effort to calculate approximately the collision probability. We define the probability as the ratio between two numbers-the area circled by the closest distance and the area of the wavepacket defined by FWHM. For the elliptically polarized laser field we get probability of 0.8% while for circularly polarized laser field,

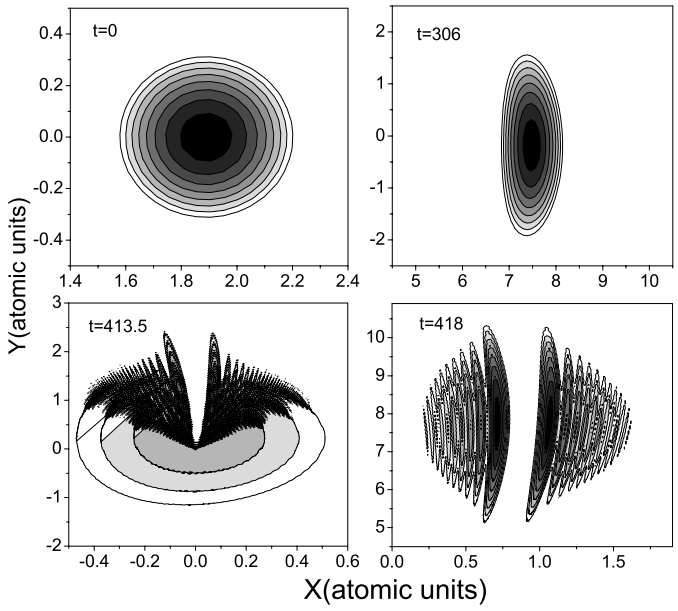

Fig. 62. Contour plots of the probability density of the wavepackets at different times: (a) t=0; (b) t=306; (c) t=413.5; (d) t=418. The contour lines are on logarithmic scale.

we get 0.3%. To induce head-on collision, the peak value of the electric field for the circularly polarized laser is about half of that used for the elliptically polarized laser field.

E. Conclusion

We explore a possible new method for studying nuclear collisions, which may lead to nuclear fusion. Unlike the conventional fusion techniques, hot plasma is not required in this method. The nuclei are well controlled, instead of moving randomly with the thermal energy. For the simulation, we first perform a classical calculation of the system of two nuclei moving under a superintense ultrashort field. Then the time-dependent quantum system of a molecule (HT) in this laser field is numerically solved. From our classical calculation we note that the nuclear collisions occur on a sub-attosecond time scale, and are predicted to result in an emission of zeptosecond bursts of light. The quantum calculation coincides well with the classical result. The relationship between the closest internuclear distance and the peak electric field being applied is studied classically.

If the experimentally obtained pulses do not have a clean and sharp enough leading front (pre-pulse exists), then a technique proposed by Ivanov and Smirnova can be used to hold the nuclei close together for a long enough time [96]. This is a so-called Molecule-without-electrons, where the positively charged nuclei are "bound" by a strong laser field. If the peak intensity of 10^{23} W/cm^2 is never achieved, then the relative velocity of the nuclei will not be sufficient for fusion, but the production of sub-attosecond pulses may still be possible due to the rapid acceleration by the Coulomb force during the nuclear collision, as we showed earlier. Since the probability of a strong collision is very low, we can use two possible ways to increase the

probability: one is that the precise control of nuclear motion may allow efficient use of nuclear resonances, the other is that nuclear wavepacket "focusing" may be possible by coherent control techniques. However, a more careful and detailed theoretical analysis is needed. In our calculation, we treated the nuclei as point particles. We need to find out what will happen when we consider the fact that the particles have finite size, i.e. nuclear physics needs to be included in our calculation. The effect of the magnetic field can be easily incorporated into the Hamiltonian and be numerically solved by the same method in the future.

CHAPTER VIII

SUMMARY

Ultrashort pulse generation is of great importance to many applications. We realize efficient generation of light frequencies spanning the infrared, visible, and ultraviolet spectral regions in Raman crystals, which provides a possible new way to generate record-short (subfemtosecond) pulses.

Our experimental work lends insight to the complicated sideband generation process in crystals. From working with the popular Raman crystal $PbWO_4$, we find that first of all, it is very important to satisfy the phase matching condition, i.e. non-collinear geometry has to be used for efficient generation in the crystal. By varying the detuning, angles, and polarization of the pump and Stokes beams, we find that FWM and Raman effects coexist and the generated sideband frequencies are very sensitive to the angles and the polarization of the pump beams. We design an interference experiment which proves the mutual coherence among the Raman sidebands generated. We also study the coherence decay of the two strong Raman modes in crystals using both fs pulses and shaped fs pulses with narrow spectral width and ps duration. We find that the two modes are excited simultaneously by the fs pump laser fields. When a third probe beam is applied in the same plane with the pump and Stokes pulses, more sidebands are generated and the energy of the high-order sidebands is enhanced. When the three laser fields (pump, Stokes and probe) are applied to the crystal in a Box CARS configuration, we observe that up to 50 colors are generated which form a 2-D color array.

We demonstrate similar generation in another crystal, diamond, which shows that the Raman generation method is universal and can be applied to other popular Raman crystals. Since diamond is an isotropic material with a simpler dispersion

relationship compared to that of the uniaxial crystal $PbWO_4$, the theoretical phase-matching calculation can easily be performed and can help understand the sideband generation process. The experiment done in diamond also sheds some light on how the 2-D color array is generated when three pulses are applied to the diamond crystal.

Compared to the Raman generation using fs fourier transform limited pulses, we obtain more efficient sidebands generation in $PbWO_4$ crystal with more sidebands generated by using a pair of time-delayed linearly chirped pulses. Up to 40 AS and 5 S are observed. As high as 41 % of pump and 21 % of Stokes conversion efficiency is measured. This shows that this is a good way to build maximal coherence in the crystal. The pulses have ps duration, which is on the order of the coherence decay time. This means ps pulses may be more effective for sideband generation than fourier transform limited fs pulses.

We also study fs CARS as an efficient tool for detecting DPA, the marker molecule for bacterial spores. From measuring the concentration dependence of the CARS signal on NaDPA, we observe a power-law dependence at low concentrations, followed by a maximum, and then a signal reduction at higher concentrations. But at lower concentration, we have observed slopes having as large as the third power of concentration. A model is used to describe this behavior and an analytical solution is found that agrees with our experimental data. We find that the concentration dependence of the signal has a slope steeper than two and can be explained when dispersion is taken into account. From the experimental study of the CSRS in crystalline DPA, we find that the orientation of a monocrystal axis with respect to the laser polarization will determine which molecular mode will interact with light, and how strongly,

As a potential application of the ultrashort and superintense laser fields when they become available, we explore theoretically a possible new method for studying nuclear collisions, which may lead to nuclear fusion. We carry out both classical

and quantum mechanical calculation of the system of two nuclei moving under a superintense ultrashort field. From our classical calculation we note that the nuclear collisions occur on a sub-attosecond time scale, and are predicted to result in an emission of zeptosecond bursts of light. The quantum calculation coincides well with the classical result. More quantum mechanical calculations of nuclear collisions are needed, for example, to estimate the probability of head-on collision and to study the zeptosecond burst of light.

In summary, we study a family of closely connected topics related to production and application of ultrashort laser pulses. We use a state-of-art commercial fs laser system to develop and efficient bioagent detector. We use the same lasers to study ways to generate record-short (subfemtosecond) pulses, and finally we analyze the possibilities for using ultrashort and superintense pulses (when they become available) to drive nuclear fusion. We study Raman generation in crystals, and elucidate the key ingredients of efficient sideband generation. It is not only interesting from a fundamental point of view, but it should also find applications in a wide variety of fields. It should be beneficial for other studies involving crystals interacting with ultrashort (fs) pulses.

Many future projects can be extended from this research. Since this is a very new and challenging experiment, there are many "mysteries" remaining to be solved. For example, the splitting in the time domain of the FWM and CARS signal, the exact mechanism of 2-D color array generation when three pulses are used, and the UV absorption when pulses are overlapped. The unequal frequency spacing between the sidebands needs more vigorous theoretical explanations. One could learn more of the sideband generation in crystals if more quantified results are obtained. For example, it will be important to characterize the sidebands, i.e. to measure the absolute sideband pulse energy and the sideband pulse width.

Whether the collinear generation in $PbWO_4$ crystal by the excitation of the small-frequency Raman mode at 325 cm^{-1} can be realized or not deserves to be studied, since collinear generation will result in the convenience of combining the sidebands for sub-fs pulse synthesis. Using two separately prepared linearly chirped pulses for the excitation of the Raman mode at 903 cm^{-1} in $PbWO_4$ crystal is also a promising experiment given the efficient sidebands generation from the excitation of the Raman mode with a lower frequency. An alternative way of excitation would be to use a pulse shaper to obtain a pulse train with a period equals to the period of Raman vibrations. If ps pulses are available, a comparison of sidebands generation using ps pulses, fs pulses, and linearly chirped pulses would be an interesting subject as well.

Optimizing the sideband generation in diamond is possible if a good sample with the right thickness is available. We have observed Stokes generated in the IR region, where diamond has a very small dispersion. Therefore it is a promising candidate material for far IR generation given its wide transmission spectral range. Of course, the most important future project will be to realize the eventual goal of the generation of sub-fs pulses using the broadband light generated in crystals.

REFERENCES

[1] L. E. Hargrove and M. A. Pollack, Applied Physics letters **5**, 4 (1964).

[2] E. P. Ippen and C. V. Shank, Applied Physics Letters **27**(9), 488 (1975).

[3] D. E. Spence, J. M. Evans, W. E. Sleat, and W. Sibbett, Optics Letters **16**, 1762 (1991).

[4] I. D. Jung, F. X. Kärtner, N. Matuschek, D. H. Sutter, F. Morier-Genoud, G. Zhang, U. Keller, V. Scheuer, M. Tilsch, and T. Tschudi, Optics Letters **22**, 1009 (1997).

[5] G. Steinmeyer, D. H. Sutter, L. Gallmann, N. Matuschek, and U. Keller, Science **286**(5444), 1507 (1999).

[6] A. V. Sokolov and S. E. Harris, Journal of Optics B: Quantum and Semiclassical Optics **5**, R1 (2003).

[7] A. V. Sokolov, M. Y. Shverdin, D. R. Walker, D. D. Yavuz, A. M. Burzo, G. Y. Yin, and S. E. Harris, Journal of Modern Optics **52**, 285 (2005).

[8] R. Kienberger, E. Goulielmakis, M. Uiberacker, A. Baltuska, V. Yakovlev, F. Bammer, A. Scrinzi, T. Westerwalbesloh, U. Kleineberg, U. Heinzmann, M. Drescher, and F. Krausz, Nature **427**, 817 (2004).

[9] T. T. Basiev, P. G. Zverev, A. Y. Karasik, V. V. Osiko, A. A. Sobol, and D. S. Chunaev, Journal of Experimental and Theoretical Physics **99**(5), 934 (2004).

[10] H. Kawano, Y. Hirakawa, and T. Imasaka, IEEE Journal of Quantum Electronics **34**(2), 260 (1998).

[11] G. Korn, O. Dühr, and A. Nazarkin, Physical Review Letters **81**(6), 1215 (1998).

[12] A. Nazarkin, G. Korn, M. Wittmann, and T. Elsaesser, Physical Review Letters **83**(13), 2560 (1999).

[13] S. Yoshikawa and T. Imasaka, Optics Communications **96**, 94 (1993).

[14] S. Katzman, American Chemical Society magazine, News in Brief **73**, 351 (2001).

[15] T. Imasaka, S. Kawasaki, and N. Ishibashi, Applied Physics B: Lasers and Optics **49**(4), 389 (1989).

[16] H. Kawano, T. Mori, Y. Hirakawa, and T. Imasaka, Physical Review A **59**(6), 4703 (1999).

[17] H. Kawano, C. H. Lin, and T. Imasaka, Applied Physics B: Lasers and Optics **63**(2), 121 (1996).

[18] H. Kawano, Y. Hirakawa, and I. Totaro, Applied Physics B: Lasers and Optics **65**(1), 1 (1997).

[19] V. Schulz-Von der Gathen, T. Bornemann, V. Kornas, and H. F. Dobele, IEEE Journal of Quantum Electronics **26**(4), 739 (1990).

[20] S. Emiliano, K. Paul, G. H. C. New, K. J. Mendham, H. Thomas, J. W. G. Tisch, and J. P. Marangos, Optics Letters **29**, 495 (2004).

[21] E. Sali, P. Kinsler, G. H. C. New, K. J. Mendham, T. Halfmann, J. W. G. Tisch, and J. P. Marangos, Physical Review A **72**(1), 013813 (2005).

[22] T. T. Basiev and R. C. Powell, Optical Materials **11**(4), 301 (1999).

[23] J. Q. Liang, M. Katsuragawa, F. L. Kien, and K. Hakuta, Physical Review Letters **85**(12), 2474 (2000).

[24] A. Dyson, A. E. Dangor, and A. K. L. Dymoke-Bradshaw, Journal of Physics B: Atomic, Molecular and Optical Physics **22**, L231 (1989).

[25] H. M. Pask, Progress in Quantum Electronics **27**, 3 (2003).

[26] I. T. Sorokina and K. L. Vodopyanov, eds., *Solid-State Mid-Infrared Laser Sources* (Springer-Verlag, New York, 2003).

[27] T. T. Basiev, A. A. Sobol, Y. K. Voronko, and P. G. Zverev, Optical Materials **15**, 205 (2000).

[28] L. L. Losev, J. Song, J. F. Xia, D. Strickland, and V. V. Brukhanov, Optics Letters **27**, 2100 (2002).

[29] A. S. Grabtchikov, R. V. Chulkov, V. A. Orlovich, M. Schmitt, R. Maksimenko, and W. Kiefer, Optics Letters **28**, 926 (2003).

[30] A. A. Kaminskii, C. L. McCray, H. R. Lee, S. W. Lee, D. A. Temple, T. H. Chyba, W. D. Marsh, J. C. Barnes, A. N. Annanenkov, V. D. Legun, H. J. Eichler, G. M. A. Gad, and K. Ueda, Optics Communications **183**, 277 (2000).

[31] T. T. Basiev, A. A. Sobol, P. G. Zverev, V. V. Osiko, and R. C. Powell, Applied Optics **38**(3), 594 (1999).

[32] E. Matsubara, K. Inoue, and E. Hanamura, Journal of the Physical Society of Japan **75**, 024712 (2006).

[33] H. Matsuki, K. Inoue, and E. Hanamura, Physical Review B **75**(2), 024102 (2007).

[34] K. Inoue, J. Kato, E. Hanamura, H. Matsuki, and E. Matsubara, Physical Review B **76**(4), 041101 (2007).

[35] A. M. Zheltikov, Journal of Raman Spectroscopy **33**(2), 112 (2002).

[36] B. Schrader, *Infrared and Raman Spectroscopy* (VCH Publishers Inc., New York, 1995).

[37] M. Chergui, *Femtochemistry* (Springer-Verlag, New York, 1996).

[38] M. M. Martin and J. T. Hynes, *Femtochemistry and Femtobiology* (Elsevier, Amsterdam, 2004).

[39] A. C. Eckbreth, *Laser Diagnostics for Combustion Temperature and Species (Combustion Science and Technology)* (Gordon and Breach, New York, 1996).

[40] R. Leonhardt, W. Holzapfel, W. Zinth, and W. Kaiser, Chemical Physics Letters **133**(5), 373 (1987).

[41] T. Lang and M. Motzkus, Journal of Optical Society of America B **19**, 340 (2002).

[42] R. P. Lucht, S. Roy, T. R. Meyer, and J. R. Gord, Applied Physics Letters **89**, 251112 (2006).

[43] M. O. Scully, G. W. Kattawar, R. P. Lucht, T. Opatrný, H. Pilloff, A. Rebane, A. V. Sokolov, and M. S. Zubairy, Proceedings of the National Academy of Sciences of the United States of America **99**, 10994 (2002).

[44] R. A. Meyers, ed., *Ultrafast Laser Technology and Spectroscopy in Encyclopedia of Analytical Chemistry* (John Wiley & Sons Ltd., New York, 2000).

[45] R. Paschotta, *Encyclopedia of laser physics and technology*, http://www.rp-photonics.com, accessed in September, 2007.

[46] R. W. Boyd, *Nonlinear Optics* (Academic Press, New York, 2002), 2nd ed.

[47] J. C. Diels and W. Rudolph, *Ultrashort Laser Pulse Phenomena* (Academic Press, New York, 2006), 2nd ed.

[48] R. S. Krishnan and R. K. Shankar, Journal of Raman Spectroscopy **10**(1), 1 (1981).

[49] W. Demtröder, *Laser Spectroscopy: Basic Concepts and Instrumentation* (Springer Verlag, Berlin, 2003).

[50] R. Tribeno, *Frequency-Resolved Optical Gating: The Measurement of Ultrashort Laser Pulses* (Kluwer Academic, Boston, 2000).

[51] D. J. Kane and R. Trebino, IEEE Journal of Quantum Electronics **29**(2), 571 (1993).

[52] A. P. Hickman, J. A. Paisner, and W. K. Bischel, Physical Review A **33**(3), 1788 (1986).

[53] F. L. Kien, K. Hakuta, and A. V. Sokolov, Physical Review A **66**(2), 023813 (2002).

[54] S. Baccaro, L. M. Barone, B. Borgia, F. Castelli, F. Cavallari, I. Dafinei, F. de Notaristefani, M. Diemoz, A. Festinesi, and E. Leonardi, Nuclear Instru-

ments and Methods in Physics Research Section A: Accelerators, Spectrometers, Detectors and Associated Equipment **385**, 209 (1997).

[55] P. Lecoq, I. Dafinei, E. Auffray, M. Schneegans, M. V. Korzhik, O. V. Missevitch, V. B. Pavlenko, A. A. Fedorov, A. N. Annenkov, V. L. Kostylev, and V. D. Ligun, Nuclear Instruments and Methods in Physics Research Section A: Accelerators, Spectrometers, Detectors and Associated Equipment **365**, 291 (1995).

[56] B. Tatian, Applied Optics **23**, 4477 (1984).

[57] M. Fujita, M. Itoh, M. Horimoto, and H. Yokota, Physical Review B **65**(19), 195105 (2002).

[58] A. A. Kaminskii, H. J. Eichler, K. Ueda, N. V. Klassen, B. S. Redkin, L. E. Li, J. Findeisen, D. Jaque, J. Garcia-Sole, J. Fernandez, and R. Balda, Applied Optics **38**, 4533 (1999).

[59] F. Manjon, D. Errandonea, N. G. Munoz, J. Pellicer-Porres, J. Lopez-Solano, P. Rodriguez-Hernandez, S. Radescu, and A. Mujica, arXiv.org Condensed matter **cond-mat/0606563**, 1 (2006).

[60] T. C. Damen, S. P. S. Porto, and B. Tell, Physical Review **142**(2), 570 (1966).

[61] G. M. A. Gad, H. J. Eichler, and A. A. Kaminskii, Optics Letters **28**, 426 (2003).

[62] J. I. Takahashi, Y. Kawabe, and E. Hanamura, Optics Express **12**, 1185 (2004).

[63] D. Pestov, M. Zhi, Z.-E. Sariyanni, N. G. Kalugin, A. Kolomenskii, R. Murawski, Y. V. Rostovtsev, V. A. Sautenkov, A. V. Sokolov, and M. O. Scully, Journal of Raman Spectroscopy **37**(1-3), 392 (2006).

[64] T. T. Basiev, A. A. Sobol, P. G. Zverev, V. V. Osiko, and R. C. Powell, Applied Optics **38**, 594 (1999).

[65] H. O. Pierson, *Handbook of Carbon Graphite, Diamond and Fullerenes: Properties, Processing, and Applications* (Noyes Publications, Park Ridge, NJ, 1993).

[66] A. A. Kaminskii, V. G. Ralchenko, and V. I. Konov, Laser Physics Letters **3**, 171 (2006).

[67] G. Eckhardt, D. P. Bortfeld, and M. Geller, Applied Physics Letters **3**(8), 137 (1963).

[68] A. K. McQuilla, W. R. Clements, and B. P. Stoichef, Physical Review A **1**(3), 628 (1970).

[69] A. A. Kaminskii, V. G. Ralchenko, V. I. Konov, and H. J. Eichler, Physica Status Solidi (B) **242**, R4 (2005).

[70] D. Y. Smith, M. Inokuti, and W. Karstens, J. Phys. : Condens. Matter **13**, 3883 (2001).

[71] D. F. Edwards and E. Ochoa, Journal of Optical Society of America **71**, 607 (1981).

[72] Y. Irie and T. Imasaka, Optics Communications **113**(1-3), 105 (1994).

[73] P. Pavone, K. Karch, O. Schütt, D. Strauch, W. Windl, P. Giannozzi, and S. Baroni, Physical Review B **48**(5), 3156 (1993).

[74] M. Zhi and A. V. Sokolov, Optics Letters **32**, 2251 (2007).

[75] E. Gershgoren, R. A. Bartels, J. T. Fourkas, R. Tobey, M. M. Murnane, and H. C. Kapteyn, Optics Letters **28**, 361 (2003).

[76] N. Dudovich, D. Oron, and Y. Silberberg, Nature **418**(6897), 512 (2002).

[77] E. B. Treacy, IEEE Journal of Quantum Electronics **QE 5**(9), 454 (1969).

[78] Y. Huang, A. Dogariu, Y. Avitzour, R. K. Murawski, D. Pestov, M. Zhi, A. V. Sokolov, and M. O. Scully, Journal of Applied Physics **100**, 124912 (2006).

[79] D. Pestov, M. Zhi, Z. E. Sariyanni, N. G. Kalugin, A. A. Kolomenskii, R. Murawski, G. G. Paulus, V. A. Sautenkov, H. Schuessler, A. V. Sokolov, G. R. Welch, Y. V. Rostovtsev, T. Siebert, D. A. Akimov, S. Graefe, W. Kiefer, and M. O. Scully, Proceedings of the National Academy of Sciences of the United States of America **102**, 14976 (2005).

[80] M. D. Crisp, Physical Review A **1**(6), 1604 (1970).

[81] N. Dudovich, D. Oron, and Y. Silberberg, Physical Review Letters **88**(12), 123004 (2002).

[82] R. Nudelman, B. V. Bronk, and S. Efrima, Applied Spectroscopy **54**(3), 445 (2000).

[83] X. Quan and E. S. Fry, Applied Optics **3418**, 3477 (1995).

[84] T. V. Inglesby, T. O'Toole, D. A. Henderson, J. G. Bartlett, M. S. Ascher, E. Eitzen, A. M. Friedlander, J. Gerberding, J. Hauer, J. Hughes, J. McDade, M. T. Osterholm, G. Parker, T. M. Perl, P. K. Russell, K. Tonat, and for the Working Group on Civilian Biodefense, JAMA: The Journal of the American Medical Association **287**(17), 2236 (2002).

[85] S. Lim, A. G. Caster, and S. R. Leone, Physical Review A **72**(4) (2005).

[86] G. Petrov, V. Yakovlev, A. Sokolov, and M. Scully, Optics Express **13**, 9537 (2005).

[87] D. Pestov, R. K. Murawski, G. O. Ariunbold, X. Wang, M. Zhi, A. V. Sokolov, V. A. Sautenkov, Y. V. Rostovtsev, A. Dogariu, Y. Huang, and M. O. Scully, Science **316**(5822), 265 (2007).

[88] S. W. Bahk, P. Rousseau, T. A. Planchon, V. Chvykov, G. Kalintchenko, A. Maksimchuk, G. A. Mourou, and V. Yanovsky, Opt. Lett. **29**, 2837 (2004).

[89] T. Tajima and G. Mourou, Physical Review Special Topics - Accelerators and Beams **5**(3), 031301 (2002).

[90] K. W. D. Ledingham, P. McKenna, and R. P. Singhal, Science **300**(5622), 1107 (2003).

[91] V. M. Malkin, G. Shvets, and N. J. Fisch, Physical Review Letters **82**(22), 4448 (1999).

[92] P. B. Corkum, Physical Review Letters **71**(13), 1994 (1993).

[93] H. Niikura, F. Legare, R. Hasbani, M. Y. Ivanov, D. M. Villeneuve, and P. B. Corkum, Nature **421**(6925), 826 (2003).

[94] S. Chelkowski, A. D. Bandrauk, and P. B. Corkum, Laser Physics **14**(4), 473 (2004).

[95] S. Chelkowski, A. D. Bandrauk, and P. B. Corkum, Physical Review Letters **93**(8), 083602 (2004).

[96] O. Smirnova, M. Spanner, and M. Ivanov, Physical Review Letters **90**(24), 243001 (2003).

[97] J. R. Vázquez de Aldana and L. Roso, Physical Review A **61**(4), 043403 (2000).

[98] N. J. Giordano, *Computational Physics* (Prentice-Hall, Englewood Cliffs, NJ, 1997).

[99] M. D. Feit, J. A. Fleck, and A. Steiger, Journal of Computational Physics **47**(3), 412 (1982).

[100] M. D. Feit and J. A. Fleck, The Journal of Chemical Physics **78**(1), 301 (1983).

[101] S. A. Chin and C. R. Chen, The Journal of Chemical Physics **117**(4), 1409 (2002).

[102] W. R. Arnold, J. A. Phillips, G. A. Sawyer, E. J. Stovall, and J. L. Tuck, Physical Review **93**(3), 483 (1954).

[103] A. V. Sokolov and S. Chelkowski, private communication (2005).

APPENDIX A

ABSORPTION CROSS SECTIONS OF NaDPA SOLUTION

The absorption cross section dependence on the wavelength, as shown in Fig. 63, is derived from the transmission measurements on 25 mM and 50 mM NaDPA solutions within the UV tuning range of OPA 2. In experiments #1 and #2, two photodetectors (DET210, Thorlabs) were used to measure the laser power before and after the sample. To eliminate possible discrepancy between the photodetectors' response, measurement #3 and #4 were done with one photodetector only. It was used to measure both the total power when there was no sample in the beam path, and the transmitted power when the sample, NaDPA solution in a 100 μm cuvette, was moved in the beam path. The solid line in Fig. 63 is an experimental result from a spectrophotometric measurement taken on a sample of NaDPA solution with an unknown concentration. It was scaled in concentration to match the data obtained in the #1-4 experiments. The close agreement between the experiments with femtosecond pulses and spectrophotometric measurements supports our assumption of linear absorption.

The absorption cross section α is determined by the formula: $\alpha = -\frac{\ln T}{d \cdot N}$. Here T is the transmission, d is the interaction length and N is the concentration of DPA in the solution.

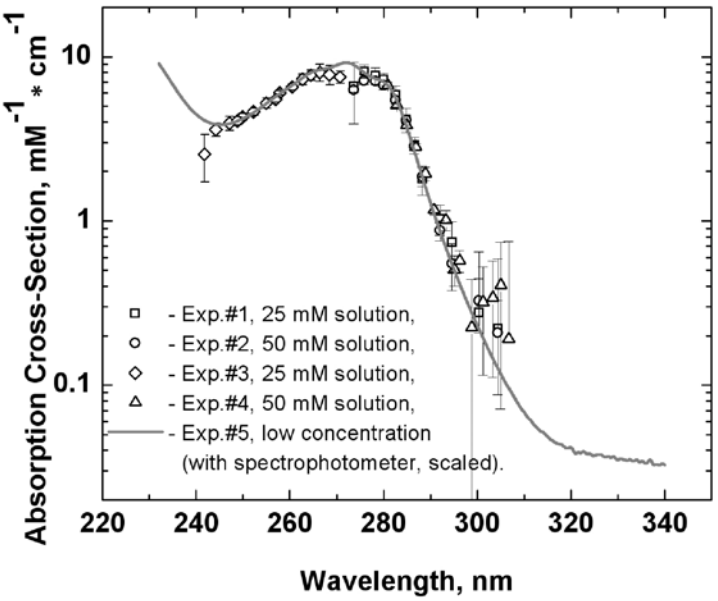

Fig. 63. Absorption cross section of NaDPA solution in UV range.

APPENDIX B

ALTERNATIVE WAY OF SOLVING THE SCHRÖDINGER EQUATION USING CRANK-NICKOLSON METHOD

The Crank-Nickolson operator equation in 1-d case is

$$\psi(x, t + \triangle t) = \frac{1 - i\frac{\triangle t}{2}H}{1 + i\frac{\triangle t}{2}H}\psi(x, t). \tag{B.1}$$

The Hamitonian

$$H = -\frac{1}{2\mu}\frac{\partial^2}{\partial x^2} + \frac{iq}{c\mu}A_x\frac{\partial}{\partial x} + 1/|x|. \tag{B.2}$$

Use m as an index for space and n as an index for time, the wavefunction, A(t) and potential $1/|x|$ can be discretisized as following:

$$\psi(x, t) = \psi(m\triangle x, n\triangle t) = \psi_m^n; \tag{B.3}$$

$$A(t) = A(n\triangle t) = A^n; \tag{B.4}$$

$$|x| = |m\triangle x|. \tag{B.5}$$

The first order and second order of the derivative of the wavefunction can be performed as:

$$\frac{d\psi_m^n}{dx} = \frac{1}{2\triangle x}(\psi_{m+1}^n - \psi_{m-1}^n); \tag{B.6}$$

$$\frac{d^2\psi_m^n}{dx^2} = \frac{1}{(\triangle x)^2}(\psi_{m+1}^n - 2\psi_m^n + \psi_{m-1}^n). \tag{B.7}$$

So in space at each grid m we have:

$$[1+\frac{i\triangle t}{2}(\alpha_1)\frac{d^2}{dx^2}+\frac{1}{m\triangle x}+\alpha_2 A^{n+1}\frac{d}{dx}]\psi_m^{n+1} \tag{B.8}$$
$$=[1-\frac{i\triangle t}{2}(\alpha_1)\frac{d^2}{dx^2}+\frac{1}{m\triangle x}+\alpha_2 A^{n}\frac{d}{dx}]\psi_m^{n}.$$

Here $\alpha_1=-\frac{1}{2\mu}$ and $\alpha_2=i\frac{q}{c\mu}$.

Plug in Eq. B.6 and Eq. B.7 for the derivatives and rearrange the terms we get:

$$\lambda^{n+1}\psi_{m-1}^{n+1}+\lambda_{mL}\psi_m^{n+1}-(\lambda^{n+1})^*\psi_{m+1}^{n+1}= \tag{B.9}$$
$$-\lambda^n\psi_{m-1}^n+\lambda_{mR}\psi_m^n-(\lambda^n)^*\psi_{m+1}^n=r(m)$$

Here $\lambda^n=\frac{i\alpha_1}{2}\frac{\triangle t}{(\triangle x)}^2-\frac{\alpha_2}{2|\triangle x|}A^n$, $\lambda_{mL}=1-i\alpha_1\frac{\triangle t}{(\triangle x)}^2+\frac{1}{m|\triangle x|}$ and $\lambda_{mR}=1+i\alpha_1\frac{\triangle t}{(\triangle x)}^2-\frac{1}{m|\triangle x|}$. The wavefunction at the next step can be obtained by solving a tridiagonal matrix:

$$\begin{bmatrix} \lambda_{1L} & -(\lambda_1^{n+1})^* & \dots & \dots & & \\ \lambda_1^{n+1} & \lambda_{2L} & -(\lambda_1^{n+1})^* & \dots & & \\ & & \vdots & \vdots & & \\ & & \vdots & \vdots & & \\ & & \lambda_1^{n+1} & \lambda_{m-1L} & -(\lambda_1^{n+1})^* & \\ & & & \lambda_1^{n+1} & \lambda_{mL} & \end{bmatrix} \begin{bmatrix} \psi_1^{n+1} \\ \psi_2^{n+1} \\ \vdots \\ \vdots \\ \psi_{m-1}^{n+1} \\ \psi_m^{n+1} \end{bmatrix} = \begin{bmatrix} r_1 \\ r_2 \\ \vdots \\ \vdots \\ r_{m-1} \\ r_m \end{bmatrix} \tag{B.10}$$

Tridiagonal matrix solver is a standard routine which can be used directly.

The 2-d problem can be reduced to 1-d problem by solving three tridiagonal matrices at each time iteration. The details are as follows.

$$H=-\frac{1}{2\mu}(\frac{\partial^2}{\partial x^2}+\frac{\partial^2}{\partial y^2})+\frac{iq}{c\mu}A_x(t)\frac{\partial}{\partial x}+\frac{iq}{c\mu}A_y(t)\frac{\partial}{\partial y}+\frac{1}{\sqrt{x^2+y^2}}. \tag{B.11}$$

Let

$$H_x = -\frac{1}{2\mu}\frac{\partial^2}{\partial x^2} + \frac{iq}{c\mu}A_x(t)\frac{\partial}{\partial x} + \frac{1}{2}\frac{1}{\sqrt{x^2+y^2}}; \tag{B.12}$$

and

$$H_y = -\frac{1}{2\mu}\frac{\partial^2}{\partial x^2} + \frac{iq}{c\mu}A_x(t)\frac{\partial}{\partial x} + \frac{1}{2}\frac{1}{\sqrt{x^2+y^2}}. \tag{B.13}$$

then

$$\exp[-i\triangle t H(t+\triangle t/2)] \approx \frac{1-\frac{i\triangle t}{2}H(t+\triangle t/2)}{1+\frac{i\triangle t}{2}H(t+\triangle t/2)}. \tag{B.14}$$

Next

$$\begin{aligned}\exp[-i\triangle t H(t+\triangle t/2)] \quad &\text{(B.15)}\\ \approx (\frac{1-\frac{i\triangle t}{4}H_x(t+\triangle t/2)}{1+\frac{i\triangle t}{2}H_x(t+\triangle t/2)})&(\frac{1-\frac{i\triangle t}{2}H_y(t+\triangle t/2)}{1+\frac{i\triangle t}{4}H_y(t+\triangle t/2)})(\frac{1-\frac{i\triangle t}{4}H_x(t+\triangle t/2)}{1+\frac{i\triangle t}{4}H_x(t+\triangle t/2)})\\ &+O(\triangle t^3).\end{aligned}$$

Finally, we have

$$\begin{aligned}\psi(t+\triangle t) \quad &\text{(B.16)}\\ = (\frac{1-\frac{i\triangle t}{4}H_x(t+\triangle t/2)}{1+\frac{i\triangle t}{2}H_x(t+\triangle t/2)})&(\frac{1-\frac{i\triangle t}{2}H_y(t+\triangle t/2)}{1+\frac{i\triangle t}{4}H_y(t+\triangle t/2)})(\frac{1-\frac{i\triangle t}{4}H_x(t+\triangle t/2)}{1+\frac{i\triangle t}{4}H_x(t+\triangle t/2)})\psi(t)\\ = (\frac{1-\frac{i\triangle t}{4}H_x(t+\triangle t/2)}{1+\frac{i\triangle t}{2}H_x(t+\triangle t/2)})&(\frac{1-\frac{i\triangle t}{2}H_y(t+\triangle t/2)}{1+\frac{i\triangle t}{4}H_y(t+\triangle t/2)})\Theta(t)\\ = (\frac{1-\frac{i\triangle t}{4}H_x(t+\triangle t/2)}{1+\frac{i\triangle t}{2}H_x(t+\triangle t/2)})&\Phi(t).\end{aligned}$$

Here

$$\Theta(t) = \frac{1-\frac{i\triangle t}{4}H_x(t+\triangle t/2)}{1+\frac{i\triangle t}{2}H_x(t+\triangle t/2)})\psi(t); \tag{B.17}$$

and

$$\Phi(t) = \frac{1 - \frac{i\triangle t}{4} H_x(t + \triangle t/2)}{1 + \frac{i\triangle t}{2} H_x(t + \triangle t/2)})\Theta(t). \tag{B.18}$$

VITA

Miaochan Zhi was born in Luoyang, Henan Province, P. R. China. She received her B.E. in optical technology and photoelectric instrument and M.S. degree in optical physics in Zhejiang University. She joined the graduate school at Texas A&M University, where she received a Ph.D. degree in ultrafast optics, in December 2007. She can be reached at the Department of Physics, Texas A&M University, College Station, TX 77843-4242.